Reconfigurable Intelligent Surface-Assisted Millimeter-Wave Wireless Communications

Zhiyu Liu

School of Electrical and Electronic Engineering

The University of Sheffield

A thesis submitted in partial fulfilment of the requirements for the degree of

Doctor of Philosophy

October 25, 2024

Abstract

The development of 6th Generation (6G) wireless communication technologies mark a new era in global connectivity, characterized by ultra-fast data transmission, near-zero latency, and the ability to support massive device density. Central to the 6G vision is the development of an intelligent communication environment, where machine learning, artificial intelligence, and edge computing enable real-time adaptive control and decision-making. Through technologies like reconfigurable intelligent surfaces (RIS), the environment can be tailored in real time to adapt to changes in network conditions, user mobility, and spatial configurations.

A reflecting RIS is an advanced technology used to enhance wireless communication by actively controlling the way electromagnetic waves propagate. Composed of numerous small, programmable elements, a reflecting RIS can reflect or absorb incoming signals to optimize their path toward a receiver. However, existing research has not adequately addressed the optimization of the quantity and deployment locations of RISs for effectively serving a mobile robot. To address this research gap, I explore the application of RIS-assisted millimeter-wave (mmWave) communications for a mobile robot operating within an indoor industrial environment containing fixed obstacles. I minimize the transmission energy consumption of the access point (AP) by jointly optimizing the number, positions, and phase shifts of the RISs, and the beamforming vectors of the AP. Simulation results indicate that the proposed algorithm converges efficiently and successfully identifies the optimal configuration of RISs, significantly

reducing the transmission energy consumption of the AP.

Unlike reflecting RIS, which merely reflect signals, an intelligent omni-surface (IOS) can simultaneously reflect and refract signals while modifying their properties, such as phase shifts and amplitude. However, existing research has not sufficiently investigated the optimization of the number and deployment locations of IOSs for serving multiple indoor users. To tackle this research gap, I investigate IOS-assisted outdoor-to-indoor mmWave communications. With a fixed total number of refracting elements, I maximize the downlink energy efficiency of the outdoor base station (BS) by jointly optimizing the number, locations, and phase shifts of the IOSs, along with the beamforming vectors of the BS. Simulation results show that the proposed algorithms efficiently determine the optimal number and placement of IOSs, significantly improving the energy efficiency of the outdoor BS.

In conclusion, the utilization of RIS/IOS significantly enhances the performance of wireless communications, and further improvements can be achieved through the optimization of deployment strategies and on/off state management. In the future, I shall extend RIS deployment to 3D space to enable more complex strategies, incorporate real-time optimization with adaptive algorithms, and explore advanced configurations, such as integrating RIS with urban landscapes, aerial platforms, and coordinating multiple RISs for managing complex electromagnetic environments.

Acknowledgment

I am deeply grateful to everyone who supported me throughout my journey at this esteemed university. Their kindness and genuine assistance have been invaluable in helping me complete my studies, and I truly could not have done it without them.

I owe my deepest thanks to my supervisor, Prof. Xiaoli Chu, whose guidance, wisdom, and patience were essential throughout my PhD journey. Her encouragement and mentorship not only shaped my academic research but also gave me strength in my everyday life. I am truly fortunate to have worked under her supervision.

I am also sincerely thankful to my colleagues, Dr. Yang Liu, Dr. Na Tang, and Dr. David López-Pérez, for their generous assistance and technical support. Their camaraderie and collaboration have been a source of inspiration and learning for me.

Finally, I want to express my heartfelt gratitude to my parents, whose unwavering love and support have given me the strength and determination to pursue my goals. Their belief in me has been my greatest motivation.

Table of Contents

List of Figures

List of Tables

List of Abbreviations

Chapter I

Introduction

I.1 Research Background

I.1.1 Intelligent Communication Environment

As the deployment of 5th generation (5G) wireless communication systems advances globally, focus is shifting to the development of 6th generation (6G) wireless networks, which promise transformative applications like augmented reality (AR), virtual reality (VR), mixed reality (MR), brain-computer interfaces, connected robotics, and autonomous systems [1]. Furthermore, 6G envisions evolving from the "internet of things" to the "internet of intelligence," integrating advanced capabilities such as blockchain, distributed ledger technologies and pervasive intelligence [2]. Achieving these ambitious objectives requires significantly exceeding the key performance indicators (KPIs) of 5G, including ultra-reliable low-latency communication, enhanced data rates, energy and spectrum efficiency, and unprecedented connection densities [3].

The shift toward millimeter-wave (mmWave) and tera-hertz (THz) frequencies, driven by the need for high bandwidths, introduces severe limitations due to high path loss, limited communication range, and sensitivity to blockages [4–6]. These chal-

lenges create bottlenecks for achieving reliable, high-speed communication in complex environments. Traditional solutions, such as enhancing hardware or optimizing network strategies [7], fail to adequately address the limitations imposed by the wireless propagation medium itself [8].

In this context, reconfigurable intelligent surface (RIS) and intelligent omni-surface (IOS) emerge as key enablers by actively manipulating the wireless propagation medium, making it controllable for signal propagation [9], [10]. This involves managing how electromagnetic waves interact with scatterers, including indoor furniture, outdoor buildings, and other infrastructure [11], [12]. By incorporating such an intelligent environment into 6G networks, it is possible to significantly enhance signal propagation, thereby meeting the demanding KPIs of future wireless systems and realizing the full potential of 6G technology.

I.1.2 Reconfigurable Intelligent Surface & Intelligent Omni-Surface

RIS, also referred to as intelligent reflecting surface (IRS) [13], [14], or large intelligent surface (LIS) [15], [16], is one of the key elements in intelligent communication environment. A RIS is a planar structure composed of numerous quasi-passive, low-cost elements [17]. Each element is capable of independently modulating the phase shift or amplitude of incoming electromagnetic signals, allowing for a fully tailored manipulation of the signal's propagation [18], [19].

Owing to their low cost, RISs can be installed on a wide range of structures, such as building exteriors, interior walls, aerial platforms, roadside billboards, highway poles, vehicle windows, and even the clothing of pedestrians [20]. These surfaces possess the distinct capability to modify the wireless propagation environment by compensating

for signal attenuation over extended distances [21]. Through the passive reflection of incoming radio waves, RISs can establish line-of-sight (LoS) connections between base stations (BSs) and mobile users, which can significantly improve the coverage of mmWave/THz wireless communications by compensating the severe path loss and high susceptibility to blockages caused by environmental obstacles [22].

From a hardware perspective, RIS offers a sustainable and energy-efficient alternative to traditional relays and amplifiers, such as amplify-and-forward (AF) and decode-and-forward (DF) systems [23]. Unlike these systems, RIS does not amplify signals but instead modulates their phase and amplitude using passive reflection [24]. This passive operation reduces power consumption, lowers hardware complexity, and enables full-duplex, full-band operation [25]. Additionally, RIS can be seamlessly integrated into existing 5G infrastructure, enabling backward compatibility while paving the way for 6G advancements [26].

As shown in Fig. I.1, the authors introduced a common architecture of RIS [27]. In each element, The uppler layer is composed of numerous reflective patches printed on a dielectric substrate, which directly interact with incident signals. Some PIN diodes are embedded between a reflective patch and the ground. The diode's biasing voltage is controlled via a direct-current feeding line, enabling it to switch between "On" and "Off" states. A copper backplane is designed to prevent signal leakage.

Different from the RIS, an IOS is a planner surface that can both reflect and refract incident signals simultaneously. As depicted in Fig. I.2, each element consists of two symmetrical layers, each comprising a reflective/refractive patch, PIN diodes, a ground plane, a via hole, and a feedline. The ground and feedline are doployed at the top and bottom of each layer, respectively, enabling the application of a varying bias voltage to control the states of the PIN diodes. The via hole facilitates the transfer of incident energy between the two layers. In the absence of a metallic backplane, the EM wave can

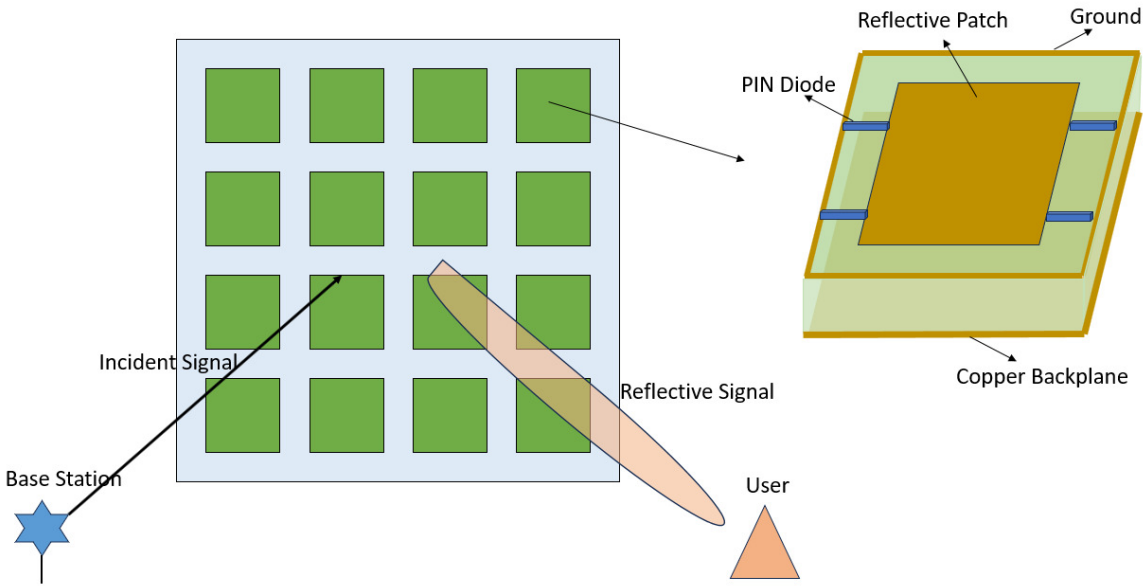

Figure I.1: The architecture of the RIS.

propagate in both directions, allowing for simultaneous reflection and refraction [27].

The RIS/IOS is usually connected to a smart controller, modulating the reflection amplitude and phase shift of each element. In practical applications, a field-programmable gate array (FPGA) can be utilized as the controller [10], acting as a communication gateway with other network components, including BSs, access points (APs), and user terminals, via dedicated wireless links for the exchange of low-rate information.

I.2 Channel model

As shown in Fig. I.3, without considering the direct link between the BS and the user, a BS with M antennas transmits signals reflected by a RIS with N elements to a single antenna users. The channel from the BS to the RIS is modeled as a Rician channel, and is denoted by $\boldsymbol{G} \in \mathbb{C}^{N \times M}$. The (n, m)-th element in $\boldsymbol{G}$ denotes the channel between

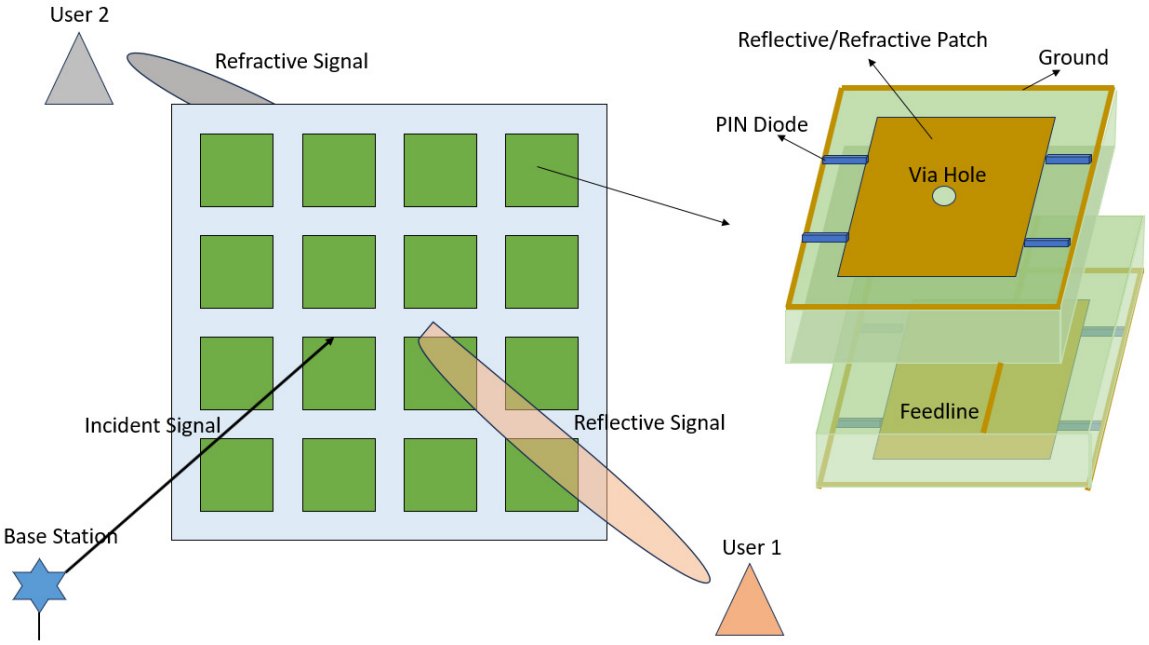

Figure I.2: The architecture of the IOS.

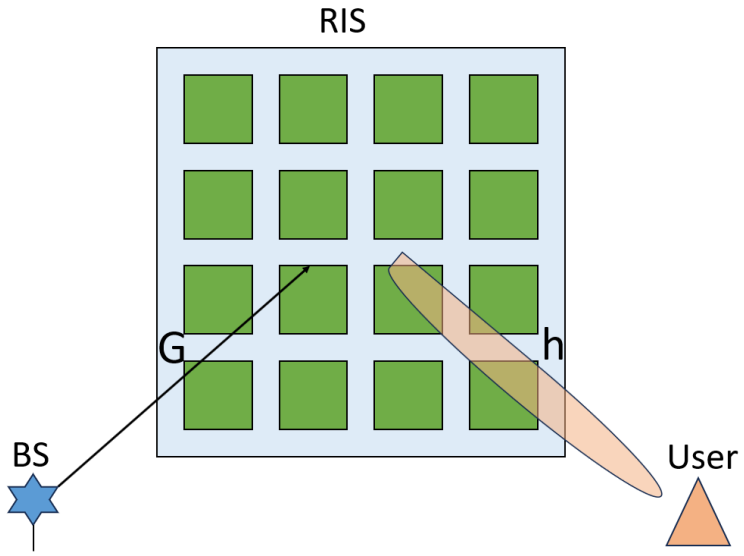

Figure I.3: Channel model

the m-th antenna at the BS and the n-th element on the RIS, and is given by [53]

$$G_{mn} = \sqrt{\frac{\epsilon}{1+\epsilon}} G_{mn}^{LoS} + \sqrt{\frac{1}{1+\epsilon}} G_{mn}^{NLoS} \tag{I.1}$$

where ϵ is the Rician factor, G_{mn}^{LoS} and G_{mn}^{NLoS} are the LoS and NLoS components, respectively, and G_{mn}^{LoS} is given by

$$G_{mn}^{LoS} = \frac{\sqrt{J_m^{BS} J_n^{RIS} K_{mn}^{A} K_{mn}^{D}} e^{\left(\frac{-j2\pi d_{mn}}{\lambda}\right)}}{(4\pi)^{\frac{3}{4}} (d_{mn})^{\alpha}} \tag{I.2}$$

where J_m^{BS} and J_n^{RIS} are the maximum antenna gain of the m-th antenna element at the BS and the maximum antenna gain of the n-th element on the RIS, respectively, $d_{mn} = \sqrt{(x_m - x_n)^2 + (y_m - y_n)^2 + (z_m - z_n)^2}$ is the distance between the m-th antenna at the BS and the n-th element on the RIS, λ is the signal wavelength, α is the path loss exponent, K_{mn}^{D} and K_{mn}^{A} are the normalized radiation pattern of the m-th antenna element at the BS in the direction of the n-th element on the RIS and the normalized radiation pattern of the n-th element on the RIS in the direction of the m-th antenna at the BS, and are given by

$$K_{mn}^{D} = \left|\cos^3 \phi_{mn}^{D}\right|, \tag{I.3}$$

$$K_{mn}^{A} = \left|\cos^3 \phi_{mn}^{A}\right|, \tag{I.4}$$

where ϕ_{mn}^{D} and ϕ_{mn}^{A} are the angle of departure (AoD) from the m-th antenna at the BS to the n-th element on the RIS and the angle of arrival (AoA) at the n-th element on the RIS from the m-th antenna at the BS, respectively.

The NLoS component in (V.1) is given by

$$G_{mn}^{NLoS} = \tilde{h}_{mn}, \tag{I.5}$$

where $\tilde{h}_{mn} \sim \mathcal{CN}(0,1)$ follows independent complex Gaussian distribution with zero mean and unit variance.

The channel from the RIS to the user is given by

$$\boldsymbol{h} = [h_1, \cdots, h_N], \tag{I.6}$$

where h_n is the channel coefficient between the n-th element on the RIS and the user, and is given by

$$h_n = \sqrt{\frac{\epsilon}{1+\epsilon}} h_n^{LoS} + \sqrt{\frac{1}{1+\epsilon}} h_n^{NLoS}, \tag{I.7}$$

where h_n^{LoS} is the LoS component and is given by

$$h_n^{LoS} = \frac{\lambda \sqrt{J_n^{IOS} J_k K_n^D K_n^A \delta_x \delta_z \gamma_n} e^{\left(\frac{-j2\pi d_n}{\lambda}\right)}}{(4\pi)^{\frac{3}{4}} (d_n)^{\alpha}}, \tag{I.8}$$

where J_k is the maximum antenna gain of the user, δ_x and δ_z are the sizes of each element on the respective IOSs, γ_n is the power ratio between the signal re-emitted by the n-th element of the RIS and the incident signal, the distance between the n-th element on the RIS and the user is given by

$$d_n = \sqrt{(x_n - x_{\text{user}})^2 + (y_n - y_{\text{user}})^2 + (z_n - z_{\text{user}})^2}. \tag{I.9}$$

K_n^D and K_n^A are the normalized radiation pattern of the n-th element on the RIS in the direction of the user and the normalized radiation pattern of the user's antenna, and are given by

$$K_n^D = \left|\cos^3 \phi_n^D\right|, \tag{I.10}$$

$$K_n^A = \left|\cos^3 \phi_n^A\right|, \tag{I.11}$$

where ϕ_n^D and ϕ_n^A are the AoD from the n-th element on the RIS to the user and the

AoA at the user from the n-th element on the RIS, respectively.

The NLoS component in (V.7) is given by

$$h_n^{NLoS} = \tilde{h}_n, \tag{I.12}$$

where $\tilde{h}_n \sim \mathcal{CN}(0, 1)$.

I.3 RIS & IOS Applications

mmWave communication is a promising technology for intelligent warehouses and factories, offering ultra-high data rates and low latency [28]. mmWave signals exhibit limited penetration capability and are easily blocked by obstacles, including dense storage racks, machinery, and structural components commonly found in warehouses and factories. These blockages lead to significant signal degradation, dead zones, and multi-path fading, which can disrupt communication reliability [28]. RIS/IOS can tackle these challenges by dynamically reconfiguring the wireless environment, ensuring reliable and efficient signal propagation.

Furthermore, the importance of RIS/IOS becomes evident in addressing the challenges of high device density and the stringent demands for low-latency communication. Modern intelligent factories and warehouses involve a multitude of internet of things (IoT) devices, automated guided vehicles and robots, and real-time monitoring systems, all of which demand seamless connectivity and minimal latency. High device density results in increased interference and spectrum utilization challenges, while latency-sensitive operations require rapid and reliable communication links. RIS/IOS addresses these issues by enabling dynamic control of signal propagation and interference, ensuring efficient spectrum utilization and maintaining low-latency, high-reliability communication even in dense and dynamic environments.

Energy efficiency and cost constraints are critical considerations in deploying communication infrastructure for intelligent warehouses and factories. Traditional approaches, such as deploying multiple APs or additional BSs, can improve coverage and reliability but at the expense of higher infrastructure and operational costs. These solutions also require significant power consumption, making them less sustainable for large-scale deployments. In contrast, RIS/IOS is designed to be low-cost due to their passive nature, primarily consisting of components like printed circuit boards, radio frequency (RF) switches, PIN diodes, and resistors [29]. The absence of active transmission modules reduces both production complexity and costs. Additionally, RIS/IOS is lightweight, easy to deploy, and does not require extensive cabling or power infrastructure, which is highly energy-efficient and cost-effective.

I.4 Research Challenges and Objectives

Employing mmWave communications in complex environments poses significant challenges due to the pronounced penetration losses and signal attenuation that mmWave signals experience when traversing walls, windows, and other obstacles. Traditional RIS are often inadequate for managing scenarios that require either refraction or the simultaneous reflection and refraction of signals. Furthermore, existing research on RIS deployment strategies remains rudimentary and lacks sophistication.

To address the severe pathloss, penetration losses and signal attenuation suffered by mmWave signals, the first objective of this research is to leverage various types of RIS e.g., reflecting RIS, refracting RIS, and IOS to mitigate these challenges in mmWave signal propagation. This approach aims to enhance the overall performance of wireless communication systems. In parallel, a second objective is to develop an advanced RIS deployment strategy that significantly improve the performance of RIS

assisted wireless communications. Finally, the third objective is to propose innovative solution algorithms capable of addressing the non-convex, variable-coupling, and varying-dimensional optimization problems that arise in these complex scenarios. Collectively, these objectives are designed to overcome the limitations of current mmWave communication systems and advance the field of RIS in intricate and dynamic environments.

I.5 Thesis Organisation

The thesis is structured into seven chapters. The organization of the content is as follows:

Chapter I presents an introduction of this thesis which includes research background, research challenges and objectives.

Chapter II presents an overview of studies concerning various types of RIS and their deployment strategies. Additionally, it introduces algorithms that address the transformation of problems from non-convex to convex forms and discusses strategies for RIS deployment.

Chapter III provides a summary of the contributions made by the three journal papers included in this thesis.

In Chapter IV and Chapter V two journal papers are presented.

Chapter VI concludes the thesis and proposes some new research directions for future work.

Chapter II

Literature Review and Optimization Algorithms used in the Thesis

II.1 Literature Review and Optimization Algorithms

II.1.1 Reflecting Reconfigurable Intelligent Surfaces

Reflecting RIS have emerged as a promising solution for enhancing wireless communication systems by manipulating the propagation environment. This subsection explores the key contributions and advancements in the optimization of reflecting RIS, focusing on their role in improving energy efficiency, beamforming, and sum-rate performance. The studies highlighted here also demonstrate the practical implications and limitations of traditional RIS-aided communication systems, providing a foundation for more complex scenarios. In [30], the authors jointly optimized the power allocation matrix at the BS and the phase shift of the RIS to maximize the energy efficiency (EE) of the

RIS-assisted wireless communication system. They solved the problem by iteratively utilizing conjugate gradient search and sequential fractional programming. Simulation results demonstrated that the proposed algorithms achieve higher EE performance compared to traditional relay-assisted communication systems. The authors identified diminishing EE returns with an increasing number of RIS elements due to the associated power consumption. It could be extended by analyzing optimal deployment strategies for varying user densities or coverage areas. In [31], the authors proposed a free-space path loss model that consider physical factors like the size of the RIS and near-field/far-field effects, validated through extensive simulations and experimental measurements using fabricated RISs in a microwave anechoic chamber. In [32], the authors utilized stochastic successive convex approximation (SCA) and fractional programming to optimize the beamforming of the BS and the phase shifts of the RIS for weighted sum-rate (WSR) maximization. They drew the conclusion that the proposed methods achieve significant performance gains in terms of WSR, especially when channel uncertainties are small, thereby demonstrating the practical viability of RIS for enhancing wireless communication performance. In [33], the authors maximized the sum rate of the multiuser multiple input and single output (MISO) system by jointly optimizing the joint design of transmit beamforming at the base station and the phase shifts at the RIS. They proposed a deep reinforcement learning based algorithm that leverages the policy-based deep deterministic policy gradient method to simultaneously determine the optimal beamforming matrix and phase shift matrix through continuous interactions with the environment. However, the aforementioned studies have primarily focused on traditional RIS-aided wireless communication scenarios, which are inadequate for addressing more complex situations, such as outdoor-to-indoor communications.

II.1.2 Refracting Reconfigurable Intelligent Surfaces

Refracting RIS extend the capabilities of traditional reflecting RIS by enabling signal transmission through obstacles while enhancing performance metrics such as data rates, power efficiency, and secrecy rates. This subsection delves into the innovative designs and optimization strategies for refracting RIS, highlighting their potential in next-generation wireless networks and pointing out areas requiring further research. In [34], the authors introduced a 2-bit transmissive Reconfigurable Intelligent Surface (RIS) element incorporating a penetration structure that merges a 1-bit current reversible dipole with a 90° digital phase shifter. They developed and evaluated a transmissive RIS prototype comprising 16 × 16 elements, achieving a peak broadside gain of 22.0 dBi at 27 gigahertz (GHz) and confirming its two-dimensional beamforming capabilities. Experimental outcomes demonstrated that RIS significantly enhances data rates, reduces transmit power, improves signal transmission through obstacles, and dynamically adapts to signal propagation directions, highlighting its potential for improving B5G network performance. The authors claimed that comparing to 1-bit phase resolution, a 2-bit phase resolution improved the performance of the RIS. The trade-offs between the performance and complexity for higher phase resolution can be further studied. In [35], the authors minimized transmit power by jointly optimizing the beamforming vectors and phase shifts of the RIS through an alternating optimization approach. They employed singular value decomposition and water-filling techniques to derive the optimized beamforming vectors, and utilized Taylor expansion and penalty methods to optimize the phase shifts. In [36], a transparent amplifying intelligent surface architecture was proposed, which refracted and amplified incoming signals. Simulation results validated that the proposed structure could significantly enhance the uplink spectral efficiency in indoor-to-outdoor mmWave communication systems. In [37], the authors maximized the weighted sum secrecy rate in a multiuser MISO

IoT network, where a refracting RIS-based transmitter delivered confidential signals to legitimate users, and a reflective RIS enhanced secrecy performance in the presence of multiple eavesdroppers. By optimizing beamforming vectors, phase shifts, and power allocation matrices using the Lagrange dual method and penalty dual decomposition, the study concluded that the proposed RIS structure achieved near-optimal secrecy rates with lower hardware complexity and power consumption compared to traditional RF transmitters. However, the aforementioned studies focused solely on the refracting function of RIS, neglecting scenarios that require the use of both reflecting and refracting functionalities.

II.1.3 Intelligent Omni-surfaces

IOS represent a revolutionary evolution in the field of RIS technology, offering combined reflection and refraction capabilities. By supporting multi-path signal manipulation, IOS significantly enhances network performance, extending coverage and improving quality of service. This subsection reviews key contributions to IOS technology, emphasizing its operational protocols, optimization strategies, and potential to outperform conventional RIS. In [38], the authors minimized the total transmit power by iteratively applying second-order cone programming and Riemannian manifold optimization techniques. They also maximized the downlink data rate using weighted minimum mean square error and block coordinate descent methods. The simulation results indicated that IOS significantly extends communication coverage, augments signal strength, and enhances the quality of service compared to conventional RIS. Nevertheless, simulation results lacked detailed benchmarking against state-of-the-art solutions, and deployment strategy of IOSs was not considered. In [39], the authors minimized the transmit power under a IOS-aided vehicular communication system. They utilized an alternating algorithm that iteratively optimized the beamforming of the BS and the phase shifts of the

IOS and also proposed a stochastic successive convex approximation-based algorithm to guarantee the convergence to a stationary point. Simulation results demonstrated that the IOS outperformed conventional RIS in terms of double fading mitigation and power savings, showing robustness against channel state information uncertainties induced by vehicular mobility. In [40], the authors developed a detailed circuit-based reflection-refraction model for IOS, which incorporated the physical structure and the angle of incidence of electromagnetic waves. The experimental results confirmed the model's accuracy and highlight the IOS's superior performance over traditional RIS, especially in mitigating signal loss and enhancing communication reliability in various deployment scenarios. In [41], the authors enhanced the network's sum rate by introducing three operational protocols for the IOS, namely, the time switching protocol, power splitting protocol, and mode switching protocol, and devised distinct algorithms for each. Simulation results demonstrated that it is prudent to position the IOS in proximity to the AP and meticulously determine the optimal number of IOS elements to maximize the overall network's sum rate. However, the researches mentioned above ignored the deployment strategy of the IOSs, which is also essential for improving the performance of the IOS.

II.1.4 RIS Deployment Strategy

The deployment strategy of RIS is a critical factor in maximizing its effectiveness in various wireless communication scenarios. This subsection synthesizes research efforts aimed at optimizing the placement and orientation of RIS, focusing on their impact on signal power, coverage probability, and system performance in different environmental settings. In [42], the authors optimized the placement and orientation of RIS to maximize received signal power in an indoor wireless communication system. Through simulation results, the authors concluded that the optimal orientation of the RIS sig-

nificantly enhances received signal power, with the RIS typically pointing towards the opposite corner of the room. However, the authors studied the power density at different observation point instead of modeling specific mobile users, and it could be extended by taking users locations/trajectories into consideration. The authors in [43] employed analytical modeling to derive closed-form expressions for coverage probability in a RIS-aided high-speed train single input and single output (SISO) downlink communication system, and used alternating optimization methods to jointly optimize the discrete phase shifts and horizontal placement of the RIS. Simulation results demonstrated that RIS significantly improves coverage performance, with optimal placement near the center of the BS coverage area. Nonetheless, specific number or locations of RIS was not considered in this work. In [44], the authors developed a theoretical framework to analyze and optimize the RIS orientation and location to maximize coverage probability. They concluded from the analysis and simulations that the RIS should be deployed vertical to the direction from the BS to the RIS with a moderate distance from the BS. The authors in [45] proposed an analytical model to assess the relationship between the RIS placement and the area illuminated by the beam when it strikes the RIS. They conclude through the simulations that when the transmission footprint is much larger than the RIS, the optimal placement is closer to the transmitter or the receiver, while if the footprint is smaller or equal to the RIS, the RIS should be placed near the receiver.

The literature reviewed above highlights a significant gap in the study of mmWave wireless communications for mobile robots within intelligent factories and warehouses. Additionally, existing works on RIS deployment strategies lack depth, as they fail to address the optimization of both the number and precise locations of RIS. Moreover, algorithms for solving complex joint optimization problems, involving the beamforming vectors of the base station, RIS/IOS phase shifts, and deployment strategies, remain

neglected.

II.2 Optimization Algorithms used in Thesis

To optimize an objective function, such as the transmit power or energy efficiency of the BS in a RIS-aided mmWave wireless communication system, the task is often challenging due to the coupling of variables, non-convexity, and varying variable dimensionality. Consequently, the problem is typically decomposed into subproblems. Different algorithms are then employed to transform the objective function and constraints from non-convex to convex, facilitating a more tractable solution approach.

II.2.1 Successive Convex Approximation

SCA is an iterative optimization method designed to address non-convex problems by transforming them into a sequence of convex subproblems [46]. Specifically, the core principle of SCA involves linearizing the non-convex components of the objective function and constraints around the current iterate, thereby generating a convex approximation (e.g., the first-order Taylor expansion of the non-convex components at current iterate) that can be solved efficiently [47]. By iteratively updating the linearization point and resolving the convex problem, SCA converges to a local optimum of the original non-convex problem.

$$\begin{aligned} \min_{x} \quad & \sin x + \frac{1}{2}x^2, \\ & s.t.\ x \in \mathbb{R} \end{aligned} \tag{II.1}$$

For instance, II.1 is a non-convex problem due to the non-convexity of $\sin x$. By expanding the objective function $\sin x$ to its first-order Taylor expansion at x_k, $\sin x =$

$\sin x_k - \cos x_k(x - x_k)$, where x_k is the value of variable x at the k-th iteration. Then, II.1 converts to

$$\begin{aligned} \min_x \ \ & \cos x_k x + \frac{1}{2}x^2, \\ & s.t.\ x \in \mathbb{R} \end{aligned} \tag{II.2}$$

Taking the derivative and setting it to zero, I obtain $x = -\cos x_k$. After that, I set $x_{k+1} = -\cos x_k$ and repeat the process above until convergence.

II.2.2 Penalty Method

The penalty method is an optimization technique employed to address constrained optimization problems by converting them into unconstrained ones [48], [49]. This transformation is accomplished by incorporating a penalty term into the objective function, which assigns a cost for violating the constraints. As the solution deviates further from the feasible region, the penalty term typically increases, thereby guiding the optimization process towards feasible solutions. This approach ensures that constraint violations are systematically reduced, promoting convergence to an optimal solution that satisfies all constraints.

$$\begin{aligned} \min_x \ \ & f(x). \\ & s.t.\ y_i(x) \leqslant 0, i = 1, \cdots, K \end{aligned} \tag{II.3}$$

II.3 can be transformed into an unconstrained problem by introducing a penalty term for the constraint violations:

$$\min_x \ \ f(x) + A \sum_{i=1}^{K} \max\left\{0, y_i(x)\right\}^2, \tag{II.4}$$

where A is the penalty parameter that controls the weight of the penalty term.

II.2.3 Dinkelbach's Method

Dinkelbach's Method is an iterative optimization algorithm specifically designed to address fractional programming problems [50]. Fractional programming entails optimizing a ratio of two functions, commonly where both the numerator and denominator are convex. This method reformulates the fractional problem into a sequence of simpler parametric subproblems, which can be efficiently solved using conventional optimization techniques. Through iterative refinement of these subproblems, Dinkelbach's Method converges to the optimal solution of the original fractional problem. For a fractional programming problem:

$$\max_{x} \ \frac{f(x)}{y(x)}, \tag{II.5}$$

$$s.t.\ y(x) > 0 \tag{II.6}$$

where $f(x)$ and $y(x)$ are real and continuous functions. By applying Dinkelbach's method, I convert II.5 to

$$\max_{x} \ f(x) - \lambda y(x), \tag{II.7}$$

$$s.t.\ y(x) > 0 \tag{II.8}$$

where λ is an parameter that can be updated in each iteration by solving II.7, i.e., $\lambda_{k+1} = \frac{f(x_k)}{y(x_k)}$, where x_k is the value of variable x in the k-th iteration. The algorithm converges until $f(x_k) - \lambda_k y(x_k) < \epsilon$, where ϵ is a threshold.

II.2.4 Genetic Algorithm

A genetic algorithm (GA) is an optimization and search heuristic based on the principles of natural selection and genetics [51]. It is particularly effective for addressing complex problems such as RIS deployment strategy where traditional optimization methods may not succeed. GAs function through a process of initialization, selection, crossover, and mutation, which collectively evolve a population of candidate solutions toward an optimal solution. Specifically, it begins with the initialization of a random population of candidate solutions, encoded as chromosomes. The fitness of each candidate is evaluated using a problem-specific fitness function. Selection processes, such as roulette wheel or tournament selection, are then applied to choose the fittest individuals for reproduction. Crossover combines pairs of parents to produce offspring, followed by mutation, which introduces random variations to maintain genetic diversity. This new population replaces some or all of the current population. These steps i.e., evaluation, selection, crossover, mutation, and replacement, are iteratively repeated over multiple generations until convergence criteria, such as reaching a satisfactory fitness level or a predefined number of generations, are met. This iterative process evolves the population of candidate solutions toward an optimal solution.

II.2.5 Continuous Population-Based Incremental Learning Algorithm

continuous population-based incremental learning (PBILc) is an advanced evolutionary algorithm that integrates aspects of genetic algorithms with competitive learning [52]. It maintains a probabilistic model representing the population's distribution, which is incrementally updated based on the performance of the individuals. The process begins with the initialization of a probability vector that represents the distribution of the

population. A population of candidate solutions is then generated based on this probability vector and evaluated for fitness. The probability vector is updated towards the best-performing individuals, thereby increasing the likelihood of sampling near-optimal solutions in subsequent generations. Mutation is applied to the probability vector to introduce random variations, maintaining genetic diversity and preventing premature convergence. This iterative process of population generation, evaluation, probability vector update, and mutation continues until a stopping criterion is met. This method adaptively refines the probability distribution, enhancing the search process for optimal solutions over successive generations.

Chapter III

Contributions of the Thesis

III.1 Papers Included in the Thesis

This thesis solves the problem of minimizing the transmission energy consumption of the AP under the scenario of RIS-assisted mmWave downlink transmission from an AP on the ceiling to a robot moving around obstacles at fixed locations inside an industrial plant and the problem of maximizing the energy efficiency of the outdoor BS under the scenario of multiple IOSs in outdoor-to-indoor mmWave communications for multiple indoor users in the presence of indoor blockages by jointly optimizing the beamforming vectors of the BS, the phase shifts of the RIS and the locations and number of the RISs/IOSs.

The above contents are included in the two journal papers in Chapter IV and Chapter V and their main contributions are summarized in the following subsections.

III.1.1 Paper I

"Reconfigurable Intelligent Surface-assisted Indoor Millimeter-wave Communications for Mobile Robots" was published in IEEE Internet of Things Journal, vol. 11, no.

1, pp. 1548-1557, on 26 June 2023. In this paper, I present a system model for RIS-assisted mmWave downlink transmission from a ceiling-mounted AP to a robot navigating around fixed obstacles within an industrial plant. In this model, one or multiple RISs are strategically positioned on a selected wall. At each point along the robot's trajectory, the model explicitly accounts for whether the robot has a LoS or non-line-of-sight (NLoS) connection with an RIS or the AP, considering the indoor industrial environment. I aim at minimizing the transmission energy consumption of the AP while ensuring that the robot's received signal to noise ratio (SNR) remains above a specified threshold throughout its movement. This is achieved by jointly optimizing the number, positions, and phase shifts of the RISs, as well as the beamforming vectors of the AP. The primary challenges of this optimization problem arise from the variable number of coupled variables involved, which are intricately linked in both the objective function and the SNR constraint.

Given the non-convex nature and complexity of the formulated joint optimization problem, direct solutions are impractical. Therefore, I decompose the problem into two subproblems and address them alternately. Specifically, for a fixed number and positions of RISs, I develop a total energy consumption optimization (TECO) Algorithm. This algorithm iteratively optimizes the phase shifts of each RIS and the beamforming vector of the AP to minimize the AP's transmission energy consumption. Conversely, for predetermined phase shifts of the RISs and beamforming vectors of the AP, I employ a genetic algorithm to determine the optimal number and deployment locations of RISs that further reduce the AP's transmission energy consumption. Subsequently, I propose a RIS locations and number (RISLN) Algorithm, which iteratively invokes the TECO Algorithm and the GA until the reduction in the AP's transmission energy consumption falls below a specified threshold. Our simulation results indicate that the proposed algorithms converge rapidly and can identify the optimal number and deploy-

ment locations of RISs, thereby minimizing the AP's transmission energy consumption while ensuring reliable communication between the AP and the robot. Additionally, the simulation results reveal that the AP's transmission energy consumption decreases as the fixed total number of reflecting elements is distributed across more RISs. However, this reduction plateaus when the number of RISs becomes excessively large.

III.1.2 Paper II

" Deployment Strategy of Intelligent Omni-surface-assisted Outdoor-to-Indoor Millimeter-wave Communications" was published in IEEE Transactions on Wireless Communications, doi: 10.1109/TWC.2024.3479919. In the second paper, our objective is to enhance the transmission energy efficiency of the outdoor BS while ensuring that the downlink data rate for each user exceeds a specified threshold. This optimization problem necessitates the simultaneous optimization of the number, positions, and phase shifts of the IOSs, alongside the beamforming vectors of the BS. The primary challenges in addressing this problem stem from the intricate interdependence of variables, the non-convex nature, and the varying dimensionality inherent to the problem.

I address the challenges posed by the varying dimensionality of the joint optimization problem by decomposing it into two subproblems. The first subproblem focuses on optimizing the phase shifts of the IOSs and the beamforming vectors of the BS for a specified number and placement of IOSs. To tackle this non-convex subproblem, I develop an energy efficiency maximization (EEM) algorithm that iteratively refines the phase shifts of each IOS and the beamforming vector of the BS. The second subproblem aims at optimizing the quantity and positions of IOSs for a predetermined set of phase shifts and beamforming vectors, employing the PBILc algorithm. By alternately addressing these two subproblems, I introduce the IOS locations and number (IOSLN) Algorithm, which iteratively ascertains the optimal number, placement,

and phase shifts of the IOSs, in conjunction with the beamforming vectors for the BS. This iterative methodology, alternating between the PBILc and EEM algorithms, ensures that modifications to the number and locations of IOSs directly influence their phase shifts and the BS's beamforming strategy, resulting in a synergistic optimization of all variables and enhancing the transmission energy efficiency of the outdoor BS. Our simulation results reveal that the proposed algorithms can determine the appropriate number and deployment locations of IOSs, thereby maximizing the energy efficiency of the outdoor BS while maintaining reliable downlink communications for all indoor users. Furthermore, the results indicate that, for a fixed total number of reconfigurable elements, the optimized number and locations of IOSs yield superior energy efficiency for the BS compared to either centralized or evenly distributed IOS deployment. The optimal number of IOSs increases with the number of indoor users, and the optimized IOS locations tend to cluster in a vertically central area of the wall.

III.2 Paper not Included in the Thesis

" Large Language Models-based On-off Control Optimization for Refracting Reconfigurable Intelligent Surface-assisted Outdoor-to-Indoor Millimeter-wave SWIPT in Mobile Robots", co-authored with Zitian Zhang and Xiaoli Chu has been submitted to IEEE IoTJ, and is currently under review.

Bibliography

[1] W. Saad, M. Bennis and M. Chen, "A vision of 6G wireless systems: Applications, trends, technologies, and open research problems," in IEEE Network, vol. 34, no. 3, pp. 134-142, May/June 2020.

[2] K. B. Letaief, Y. Shi, J. Lu and J. Lu, "Edge artificial intelligence for 6G: Vision, enabling technologies, and applications," in IEEE Journal on Selected Areas in Communications, vol. 40, no. 1, pp. 5-36, Jan. 2022.

[3] I. F. Akyildiz, A. Kak and S. Nie, "6G and beyond: The future of wireless communications systems," in IEEE Access, vol. 8, pp. 133995-134030, 2020.

[4] C. -X. Wang et al., "On the Road to 6G: Visions, Requirements, Key Technologies, and Testbeds," in IEEE Communications Surveys and Tutorials, vol. 25, no. 2, pp. 905-974, Secondquarter 2023.

[5] I. F. Akyildiz, C. Han, Z. Hu, S. Nie and J. M. Jornet, "Terahertz band communication: An old problem revisited and research directions for the next decade," in IEEE Transactions on Communications, vol. 70, no. 6, pp. 4250-4285, June 2022.

[6] C. Chaccour, M. N. Soorki, W. Saad, M. Bennis, P. Popovski and M. Debbah, "Seven defining features of terahertz (THz) wireless systems: A fellowship of com-

munication and sensing," in IEEE Communications Surveys and Tutorials, vol. 24, no. 2, pp. 967-993, Secondquarter 2022.

[7] J. A. Hodge, K. V. Mishra and A. I. Zaghloul, "Intelligent time-varying metasurface transceiver for index modulation in 6G wireless networks," in IEEE Antennas and Wireless Propagation Letters, vol. 19, no. 11, pp. 1891-1895, Nov. 2020.

[8] A. Dogra, R. K. Jha and S. Jain, "A survey on beyond 5G network with the advent of 6G: Architecture and emerging technologies," in IEEE Access, vol. 9, pp. 67512-67547, 2021.

[9] Q. Wu and R. Zhang, "Towards smart and reconfigurable environment: Intelligent reflecting surface aided wireless network," in IEEE Communications Magazine, vol. 58, no. 1, pp. 106-112, January 2020.

[10] Cui TJ, Qi MQ, Wan X, Zhao J, Cheng Q. Coding metamaterials, digital metamaterials and programmable metamaterials. Light: science and applications, vol. 3, no. 10, pp.e218-e218, Oct. 2014.

[11] A. Rasouli and J. K. Tsotsos, "Autonomous vehicles that interact with pedestrians: A survey of theory and practice," in IEEE Transactions on Intelligent Transportation Systems, vol. 21, no. 3, pp. 900-918, March 2020.

[12] J. Zhang and K. B. Letaief, "Mobile edge intelligence and computing for the internet of vehicles," in Proceedings of the IEEE, vol. 108, no. 2, pp. 246-261, Feb. 2020.

[13] Q. Wu and R. Zhang, "Intelligent reflecting surface enhanced wireless network via joint active and passive beamforming," in IEEE Transactions on Wireless Communications, vol. 18, no. 11, pp. 5394-5409, Nov. 2019.

[14] Q. Wu, S. Zhang, B. Zheng, C. You and R. Zhang, "Intelligent reflecting surface-aided wireless communications: A tutorial," in IEEE Transactions on Communications, vol. 69, no. 5, pp. 3313-3351, May 2021.

[15] S. Hu, F. Rusek and O. Edfors, "Beyond massive MIMO: The potential of positioning with large intelligent surfaces," in IEEE Transactions on Signal Processing, vol. 66, no. 7, pp. 1761-1774, 1 April1, 2018.

[16] D. Dardari, "Communicating with large intelligent surfaces: Fundamental limits and models," in IEEE Journal on Selected Areas in Communications, vol. 38, no. 11, pp. 2526-2537, Nov. 2020.

[17] C. Pan et al., "An overview of signal processing techniques for RIS/IRS-aided wireless systems," in IEEE Journal of Selected Topics in Signal Processing, vol. 16, no. 5, pp. 883-917, Aug. 2022.

[18] M. Jian et al., "Reconfigurable intelligent surfaces for wireless communications: Overview of hardware designs, channel models, and estimation techniques," in Intelligent and Converged Networks, vol. 3, no. 1, pp. 1-32, March 2022.

[19] M. Di Renzo et al., "Smart radio environments empowered by reconfigurable intelligent surfaces: How it works, state of research, and the road ahead," IEEE J. Sel. Areas Commun., vol. 38, no. 11, pp. 2450–2525, Nov. 2020.

[20] Y. Liu et al., "Reconfigurable intelligent surfaces: Principles and opportunities," in IEEE Communications Surveys and Tutorials, vol. 23, no. 3, pp. 1546-1577, thirdquarter 2021.

[21] Z. Zhang et al., "Active RIS vs. passive RIS: Which will prevail in 6G?," in IEEE Transactions on Communications, vol. 71, no. 3, pp. 1707-1725, March 2023.

[22] E. Björnson and L. Sanguinetti, "Rayleigh fading modeling and channel hardening for reconfigurable intelligent surfaces," in IEEE Wireless Communications Letters, vol. 10, no. 4, pp. 830-834, April 2021.

[23] Z. Yang, Z. Ding, Y. Wu and P. Fan, "Novel relay selection strategies for cooperative NOMA," in IEEE Transactions on Vehicular Technology, vol. 66, no. 11, pp. 10114-10123, Nov. 2017.

[24] B. Zheng, C. You, W. Mei and R. Zhang, "A survey on channel estimation and practical passive beamforming design for intelligent reflecting surface aided wireless communications," in IEEE Communications Surveys and Tutorials, vol. 24, no. 2, pp. 1035-1071, Secondquarter 2022.

[25] X. Pei et al., "RIS-aided wireless communications: Prototyping, adaptive beamforming, and indoor/outdoor field trials," in IEEE Transactions on Communications, vol. 69, no. 12, pp. 8627-8640, Dec. 2021.

[26] A. Araghi et al., "Reconfigurable intelligent surface (RIS) in the sub-6 GHz band: Design, implementation, and real-world demonstration," in IEEE Access, vol. 10, pp. 2646-2655, 2022.

[27] H. Zhang and B. Di, "Intelligent omni-surfaces: Simultaneous refraction and reflection for full-dimensional wireless communications," in IEEE Communications Surveys & Tutorials, vol. 24, no. 4, pp. 1997-2028, Fourthquarter 2022.

[28] Gulia, Rahul, Abhishek Vashist, Amlan Ganguly, Clark Hochgraf, and Michael E. Kuhl. "Evaluation of 60 GHz wireless connectivity for an automated warehouse suitable for industry 4.0." Information 14, no. 9 (2023): 506.

[29] R. Wang, Y. Yang, B. Makki and A. Shamim, "A wideband reconfigurable intelligent surface for 5G millimeter-wave applications," in IEEE Transactions on Antennas and Propagation, vol. 72, no. 3, pp. 2399-2410, March 2024.

[30] C. Huang, A. Zappone, G. C. Alexandropoulos, M. Debbah and C. Yuen, "Reconfigurable intelligent surfaces for energy efficiency in wireless communication," in IEEE Transactions on Wireless Communications, vol. 18, no. 8, pp. 4157-4170, Aug. 2019.

[31] W. Tang et al., "Wireless communications with reconfigurable intelligent surface: Path loss modeling and experimental measurement," in IEEE Transactions on Wireless Communications, vol. 20, no. 1, pp. 421-439, Jan. 2021.

[32] H. Guo, Y. -C. Liang, J. Chen and E. G. Larsson, "Weighted sum-rate maximization for reconfigurable intelligent surface aided wireless networks," in IEEE Transactions on Wireless Communications, vol. 19, no. 5, pp. 3064-3076, May 2020.

[33] C. Huang, R. Mo and C. Yuen, "Reconfigurable intelligent surface assisted multiuser MISO systems exploiting deep reinforcement learning," in IEEE Journal on Selected Areas in Communications, vol. 38, no. 8, pp. 1839-1850, Aug. 2020.

[34] J. Tang, M. Cui, S. Xu, L. Dai, F. Yang and M. Li, "Transmissive RIS for B5G communications: Design, prototyping, and experimental demonstrations," in IEEE Transactions on Communications, vol. 71, no. 11, pp. 6605-6615, Nov. 2023.

[35] Z. Lin et al., "Refracting RIS-aided hybrid satellite-terrestrial relay networks: Joint beamforming design and optimization," in IEEE Transactions on Aerospace and Electronic Systems, vol. 58, no. 4, pp. 3717-3724, Aug. 2022.

[36] B. Liu, Q. Wang and S. Pollin, "TAIS: Transparent amplifying intelligent surface for indoor-to-outdoor mmWave communications," in IEEE Transactions on Communications, vol. 72, no. 2, pp. 1223-1238, Feb. 2024.

[37] H. Niu et al., "Joint Beamforming Design for Secure RIS-Assisted IoT Networks," in IEEE Internet of Things Journal, vol. 10, no. 2, pp. 1628-1641, 15 Jan.15, 2023

[38] W. Cai, M. Li, Y. Liu, Q. Wu and Q. Liu, "Joint beamforming design for intelligent omni surface assisted wireless communication systems," in IEEE Transactions on Wireless Communications, vol. 22, no. 2, pp. 1281-1297, Feb. 2023.

[39] Y. Chen, Y. Wang, Z. Wang and P. Zhang, "Robust beamforming for active reconfigurable intelligent omni-surface in vehicular communications," in IEEE Journal on Selected Areas in Communications, vol. 40, no. 10, pp. 3086-3103, Oct. 2022.

[40] S. Zeng et al., "Intelligent omni-surfaces: Reflection-refraction circuit model, full-dimensional beamforming, and system implementation," in IEEE Transactions on Communications, vol. 70, no. 11, pp. 7711-7727, Nov. 2022.

[41] L. Lv et al., "Self-Sustainable Intelligent Omni-Surface Aided Wireless Networks: Protocol Design and Resource Allocation," in IEEE Transactions on Wireless Communications, vol. 23, no. 7, pp. 7503-7519, July 2024.

[42] G. Stratidakis, S. Droulias and A. Alexiou, "Optimal position and orientation study of reconfigurable intelligent surfaces in a mobile user environment," in IEEE Transactions on Antennas and Propagation, vol. 70, no. 10, pp. 8863-8871, Oct. 2022.

[43] C. Liu et al., "Reconfigurable intelligent surface assisted high-speed train communications: Coverage performance analysis and placement optimization," in IEEE Transactions on Vehicular Technology, vol. 73, no. 3, pp. 3750-3766, March 2024.

[44] S. Zeng, H. Zhang, B. Di, Z. Han and L. Song, "Reconfigurable intelligent surface (RIS) assisted wireless coverage extension: RIS orientation and location optimization," in IEEE Communications Letters, vol. 25, no. 1, pp. 269-273, Jan. 2021.

[45] K. Ntontin, A. -A. A. Boulogeorgos, D. G. Selimis, F. I. Lazarakis, A. Alexiou and S. Chatzinotas, "Reconfigurable intelligent surface optimal placement in millimeter-wave networks," in IEEE Open Journal of the Communications Society, vol. 2, pp. 704-718, 2021.

[46] Razaviyayn, Meisam. "Successive convex approximation: Analysis and applications." PhD diss., University of Minnesota, 2014.

[47] Mehanna, Omar, Kejun Huang, Balasubramanian Gopalakrishnan, Aritra Konar, and Nicholas D. Sidiropoulos. "Feasible point pursuit and successive approximation of non-convex QCQPs." IEEE Signal Processing Letters 22, no. 7 (2014): 804-808.

[48] Bertsekas, Dimitri P. "Necessary and sufficient conditions for a penalty method to be exact." Mathematical programming 9.1 (1975): 87-99.

[49] Schlüter, Martin, and Matthias Gerdts. "The oracle penalty method." Journal of Global Optimization 47 (2010): 293-325.

[50] W. Dinkelbach, "On nonlinear fractional programming," Management Science, vol. 13, no. 7, pp. 492–498, 1967.

[51] Katoch S, Chauhan SS, Kumar V. A review on genetic algorithm: past, present, and future. Multimedia tools and applications. 2021 Feb;80:8091-126.

[52] M. Sebag and A. Ducoulombier, "Extending population-based incremental learning to continuous search spaces", International Conference on Parallel Problem Solving from Nature, pp. 418-427, 1998.

[53] S. Zhang et al., "Intelligent omni-surfaces: Ubiquitous wireless transmission by reflective-refractive metasurfaces," in IEEE Transactions on Wireless Communications, vol. 21, no. 1, pp. 219-233, Jan. 2022.

Chapter IV

Paper I: Reconfigurable Intelligent Surface-assisted Indoor Millimeter-wave Communications for Mobile Robots

Introduction & Comments

In this paper, I studies RIS-assisted indoor mmWave communications for a mobile robot navigating through an indoor industrial environment with obstacles along a fixed trajectory. To solve the AP's transmission energy minimization problem, I propose TECO and RISLN algorithms to jointly optimize the number, locations, phase shifts of the RIS and the beamforming vector of the AP. Simulation results show the proposed methods significantly reduce AP's energy consumption compared to benchmarks, highlighting that distributing RIS elements across multiple locations improves energy efficiency up to an optimal point, after which further splitting reduces performance due to weaker beamforming gains.

Here are some further detailed explanations to avoid confusion. The LoS link indicator for all the elements on a RIS is considered the same, since I assume the location of the central element of an RIS's array as the location of the RIS for simplicity.

Note that, since the trajectory of the robot is fixed, $\boldsymbol{w}^{(t)}$ and $\boldsymbol{\Theta}_k^{(t)}$ are independent for different t, the objective function of $(P1)$ is minimized when each $\left\|\boldsymbol{w}^{(t)}\right\|^2$ in the summation from $t = 0$ to $t = T$ is minimized.

Theoretically, if the optimization problem is correctly formulated as a maximization problem, and the iterative algorithm is designed to monotonically improve the objective function (e.g., via alternating optimization or gradient-based updates), the value of the objective function should not decrease after each iteration. However, in practice, it is possible for the objective function to temporarily decrease due to several factors, including poor initialization or algorithmic effects. For example, an initial beamforming direction that aligns poorly with the channel or random initialization of RIS phase shifts may result in suboptimal intermediate solutions that temporarily reduce the objective value. Therefore, an effective initialization technique should be employed, such as

aligning the beamforming vector with the strongest channel component.

It is important to note that Fig. IV.2 is not an averaged value, as it is specifically intended to illustrate the impact of the 'crossover' and 'mutation' processes on the algorithm's convergence. In contrast, all other figures in the 'Simulation Results' section are averaged over more than 100 simulations.

The reasons for why choose 60 GHz as the carrier frequency but not lower mmWave frequency such as 27 GHz: From the perspective of bandwidth availability, 60 GHz offers significantly larger available bandwidth, which supports ultra-high data rates necessary for modern applications, such as industrial automation and high-definition video streaming. In contrast, 27 GHz provides less bandwidth, typically limited to narrower channels, making it less optimal for applications requiring large throughput. In terms of the considered scenario: although both 60 GHz and 27 GHz experience significant path loss compared to lower frequency bands, 60 GHz is particularly suitable for indoor environments where the propagation distance is shorter, and the reflections from surfaces can be exploited using RISs.

The proposed TECO and RISLN algorithms are compared with several benchmarks including the schemes used in existing works [24] and other RIS deployment strategies. The system model employs standard path loss models for both LoS and NLoS links, incorporating widely accepted parameters like path loss exponents and channel gains [25]. Noise power and other simulation parameters are also derived from existing studies and typical values used in the literature [21], ensuring consistency with standard practices. Findings like distributing RIS deployment strategy outperforms the centralized deployment were studied and demonstrated in existing works [9], [21], and I further validate and extend the findings to 'Distributing the fixed total number of reflecting elements to more RISs leads to a lower transmission energy consumption of the AP, since more distributed RISs provide more LoS links to the robot while it moves along its trajec-

tory. The reduction in AP transmission energy consumption stops when the number of RISs becomes too large.'

Reconfigurable Intelligent Surface-assisted Indoor Millimeter-wave Communications for Mobile Robots

Zhiyu Liu*, Yang Liu, Xiaoli Chu

Abstract

Reconfigurable intelligent surfaces (RISs) and millimeter-wave (mmWave) communications have been considered for providing wireless connectivity to mobile robots used in industrial plants and other indoor environments. However, the existing works have not sufficiently studied how the number and deployment locations of RISs should be optimized for serving a mobile robot. In this paper, we study RIS-assisted mmWave communications for a robot moving around fixed obstacles in an indoor industrial environment. For a fixed total number of reflecting elements, we formulate an optimization problem to minimize the transmission energy consumption of the access point (AP) while ensuring the robot's received signal-to-noise ratio (SNR) above a threshold throughout its journey by jointly optimizing the number, positions and phase shifts of RISs and the beamforming vectors of the AP. To solve the formulated non-convex optimization problem, we devise an iterative algorithm that decomposes it into two subproblems (i.e., optimizing the phase shifts of RISs and the beamforming vector of the AP, and optimizing the number and locations of RISs) and solves them

*Zhiyu Liu, Yang Liu, and Xiaoli Chu are with the Electronic and Electrical Engineering Department, The University of Sheffield, Sheffield S1 4ET, UK.

alternately. Simulation results show that the proposed algorithm converges fast and can obtain the best number and locations of RISs that lead to a transmission energy consumption of the AP much lower than the benchmark schemes.

IV.1 Introduction

As the industrial Internet of things (IIoT) continues to expand, wirelessly connected mobile robots are expected to be in increasingly widespread use, carrying out various tasks [1]. Due to the presence of machines, furniture and other things in an industrial environment, the line-of-sight (LoS) link between an access point (AP) and a mobile robot is likely to be blocked while the robot is moving around them. This makes it difficult to employ millimeter-wave (mmWave) communications for mobile robots because non-line-of-sight (NLoS) mmWave links suffer from severe penetration losses [2], [3].

To increase the possibility of a receiver seeing a LoS link and to enable continuous connectivity, reconfigurable intelligent surfaces (RISs) have been employed to reflect signals from a transmitter to a receiver [4]. An RIS is a planar surface composed of reconfigurable passive reflecting elements, each being capable of controlling the amplitude and phase shift of their reflected signal [5], and has attracted a lot of interest from researchers. In [6], the authors minimized the transmit power of the AP by jointly optimizing the phase shifts of elements on a single RIS and the beamforming vectors at the AP while meeting the downlink signal-to-interference-plus-noise ratio (SINR) requirement. Their results demonstrated that the transmit power at the AP can be scaled down by $1/N^2$, where N denotes the number of elements on the RIS. In [7], the authors maximized the downlink received signal-to-noise ratio (SNR) in a single RIS-aided multiple-input single-output (MISO) mmWave communication system by

optimizing the phase shifts of the RIS and found that the RIS achieved a lower outage probability than amplify-and-forward (AF) relaying. In [8], the authors maximized the downlink received signal power in a RIS-aided MISO system by jointly optimizing the active beamforming at the AP and passive beamforming at the RIS. We note that only a single RIS was considered in [6]–[8] and their results cannot be readily extended to cases of multiple RISs.

Deploying multiple RISs opens the door to more design variables, such as the number and deployment positions of RISs. In [9], the simulation results showed that a distributed deployment of multiple RISs across the service area of a base station (BS) can improve the mean rate of all the users as compared with the full-duplex (FD) relaying; and when centralizing the fixed total number of elements on fewer RISs, the mean user rate will increase but the fairness among spatially distributed users in terms of their achievable rates will degrade. In [10], the authors found that for a fixed total number of elements, deploying one RIS achieves a larger capacity region for two single-antenna users of different data rate requirements than deploying two RISs. In [11], the results showed that deploying two RISs can increase the downlink received signal power by a factor of $\mathcal{O}(N^4)$, while that of deploying a single RIS is $\mathcal{O}(N^2)$, where N is the total number of reflecting elements. In [12], the authors showed that with a fixed total number of elements, the distributed deployment of multiple RISs (at the same height on a vertical 2D plane) can achieve a higher downlink ergodic capacity than deploying a single RIS under outdated channel state information in a single-input single-output (SISO) system. In [13], the authors maximized the downlink sum rate of all users in a multi-RIS-aided MISO system by jointly optimizing the beamforming vector at the BS, the phase shifts at the RISs and the block-length for ultra-reliable low-latency communication (URLLC) subject to a maximum allowed packet error probability. In [14], the authors jointly optimized the locations of UAVs each carrying an RIS, the phase

shifts of the RISs and the BS transmit power to minimize the number of RISs required for meeting a downlink received SNR requirement. However, the above studies on the deployment of multiple RISs all assumed that the user devices were stationary. Their results cannot be readily extended to the cases of moving users, because the LoS/NLoS status of the links from the RISs and BSs to the users may change as the users move around obstacles. Moreover, in [10]-[12], only two RISs were considered, while the locations of them were not optimized.

Recently, RIS-assisted communications for moving objects have been studied. In [15], the authors maximized the uplink average data rate of a robot moving from an initial position to a target position within a limited time by jointly optimizing the phase shifts of an RIS deployed nearby, the trajectory and the beamforming vector of the robot. In [16], the trajectory and speed of a UAV (carrying a RIS) and the phase shifts of the RIS were jointly optimized to maximize the average downlink rate of a vehicle that moves along a road in an urban area. In [17], the authors analyzed the coverage probability of a single-antenna vehicle served by a UAV carried BS and a single RIS deployed on the exterior wall of a building while the vehicle drives along a straight motorway for different positions of the UAV. In [18], for a vehicular network assisted by a UAV carried RIS, the authors maximized the minimum downlink throughput among all the vehicles served by a BS by jointly optimizing the phase shifts of the RIS, transmission scheduling, transmission power of the BS and the UAV trajectory. In [15]-[18], only a single RIS was considered. In [19], the vehicles moving along a straight motorway were served by a BS carried by a UAV and multiple RISs deployed on a vertical 2D plane that is parallel to motorway, where each RIS served a different vehicle. The authors minimized the sum outage probability of all the vehicles by optimizing the transmit power of the BS, but the locations or number of RISs were not optimized. We note that in the above works, the LoS/NLoS status of each link

was statistically characterized by an independent LoS probability, but the impact of blockage(s) on the wireless links seen by a moving user was not explicitly modeled.

In this paper, we study RIS-assisted mmWave communications for a mobile robot in an indoor industrial environment with large obstacles. Aiming to minimize the transmission energy consumption of the AP, we investigate whether a fixed number of passive elements should be distributed to a large number of small RISs or centralized to a small number of large RISs, while maintaining reliable downlink communications for a robot moving around the obstacles along a known trajectory within a given time limit. The contributions of this paper are summarized as follows:

- We present a system model for the RIS-assisted mmWave downlink transmission from an AP on the ceiling to a robot moving around obstacles at fixed locations inside an industrial plant, where one or multiple RISs are deployed on a selected wall. At each position along its trajectory, whether the robot sees a LoS or NLoS link from an RIS or the AP is explicitly modelled for the considered indoor industrial environment. This is different from the existing works [15]-[19] where the effects of blockages on the links from the RISs or APs to the moving users (e.g., vehicles or robots) were not explicitly modeled.

- We formulate an optimization problem to minimize the transmission energy consumption of the AP while guaranteeing that the received SNR at the robot is kept above a threshold throughout its journey by jointly optimizing the number, positions and phase shifts of RISs and the beamforming vectors of the AP. The difficulties of this optimization problem mainly lie in the unfixed number of variables that are coupled in both the objective function and the constraint on the received SNR in complicated ways. This is different from the existing works where only a single RIS was considered [6]-[8], [15]-[18], the locations or

numbers of RISs were not optimized [10]-[12], [19], or users were assumed to be stationary [6]-[14].

- Since the formulated joint optimization problem is non-convex and difficult to solve directly, we decompose it into two subproblems and solve them alternately. More specifically, for given number and locations of RISs, we devise a Total Energy Consumption Optimization (TECO) Algorithm to minimize the AP's transmission energy consumption by iteratively optimizing the phase shifts of each RIS and the beamforming vector of the AP. For given phase shifts of the RISs and beamforming vectors of the AP, we devise a genetic algorithm to find the optimal number and deployment locations of RISs that minimize the AP's transmission energy consumption. Then, we propose a RIS Locations and Number (RISLN) Algorithm that iteratively calls the TECO Algorithm and the genetic algorithm until the decrease of the AP transmission energy consumption is below a threshold.

- Our simulation results demonstrate that the proposed algorithms converge fast and can find the suitable number and best deployment locations of RISs that minimize the AP's transmission energy consumption while maintaining reliable communications between the AP and the robot. The simulation results also show that the transmission energy consumption of the AP decreases when the fixed total number of reflecting elements are shared by more distributed RISs, but the reduction in AP transmission energy consumption stops when the number of RISs becomes too large.

The rest of the paper is organized as follow. In Section II, we introduce the system model, LoS/NLoS status indicator vector and channel model. In Section III, we formulate the AP's transmission energy consumption minimization problem and pro-

pose algorithms to solve it. In Section IV, we provide simulation results. Finally, we conclude the paper in Section V.

IV.2 System Model

IV.2.1 System Model

As shown in Fig. IV.1, we consider an industrial indoor environment containing several parallel rows of interior obstacles (e.g., large machines or shelves deployed in parallel across the industrial plant) in a Cartesian coordinate system, where one of the ground corners of the plant is set as the origin of the horizontal plane. The plant has a rectangular floor area of $l_f \times l_p$, where l_f is the length of the wall perpendicular to the rows of obstacles, and l_p is the length of the wall parallel to the rows of obstacles. We model the parallel obstacles as evenly spaced identical convex cubes each of length L, width W, and height H, where the distance between any two adjacent obstacle is l_a, and the number of obstacles is given by $I \leqslant l_f/(l_a + W)$. A robot moves on the horizontal ground plane around the parallel rows of obstacles from a starting point q_s to a destination point q_d along a fixed trajectory (as indicated by the dashed line on the ground plane in Fig. IV.1). The trajectory keeps a distance of l ($< l_a/2$) meters from the closet obstacle and forms a U shaped route between any two adjacent obstacles. The obstacles locate along the robot's trajectory from q_s to q_d are denoted by $O_1, O_2, \cdots, O_I$, respectively. The corners of the obstacles closest to the start point are denoted by $q_{O_1}, q_{O_2}, \cdots, q_{O_I}$ and are used to represent the locations of the corresponding obstacles.

We consider the downlink from an access point (AP) mounted on the ceiling to the single-antenna robot. The AP is equipped with a uniform linear array (ULA) of M (>1) antennas. The location of the AP is denoted by q_A. There are K RISs

deployed on a wall perpendicular to the obstacles to reflect signals from the AP to the robot. Each RIS is equipped with $\frac{N}{K}$ passive reflecting elements, where N is the total number of passive reflecting elements of all the RISs. We assume that the reflecting elements on the RISs are all passive [5]-[7]. The deployment of RISs ensures the LoS links between the AP and themselves, and their locations are higher than the receive antenna on the robot. The locations of RISs are given by $\boldsymbol{q}_R = [q_{R_1}, q_{R_2}, \cdots, q_{R_K}]$, where $q_{R_k} = [x_{R_k}, y_{R_k}, z_{R_k}]$. The passive reflecting elements of each RIS form an uniform rectangular array (URA). For simplicity, the location of the central element of the AP's or an RIS's array is considered as the location of the AP or the RIS, which is used to calculate the distance between the AP or the RIS and another communication node [6]. Each RIS is connected to a smart controller that adjusts its phase shifts and reflection amplitudes via a separate wired link.

The time required for the robot to move from the start point to the destination along the fixed trajectory is divided into $T+1$ timeslots, $t = 0, \cdots, T$. Timeslot t has a duration Δ_t, which is sufficiently short so that the channel conditions can be assumed to be fixed within the timeslot. In timeslot t, the robot moves over a distance of $D_t = v_t \Delta_t$, where v_t is the speed of the robot in timeslot t. We use the location of the robot antenna to represent the location of the robot at any time. The trajectory of the robot can be represented by $\boldsymbol{q} = [q_0, q_1, \cdots, q_T]$, where $q_t = [x_t, y_t, z_r]$ denotes the position of the robot in the t-th timeslot, z_r is the height of the robot antenna above ground, $q_0 = q_s$, and $q_T = q_d$.

IV.2.2 LoS Indicator Matrix

The AP-robot and RIS$_k$-robot links ($k = 1, \cdots, K$) may become NLoS when they are blocked by obstacles as the robot moves along the trajectory. We define an $I \times (K+1)$

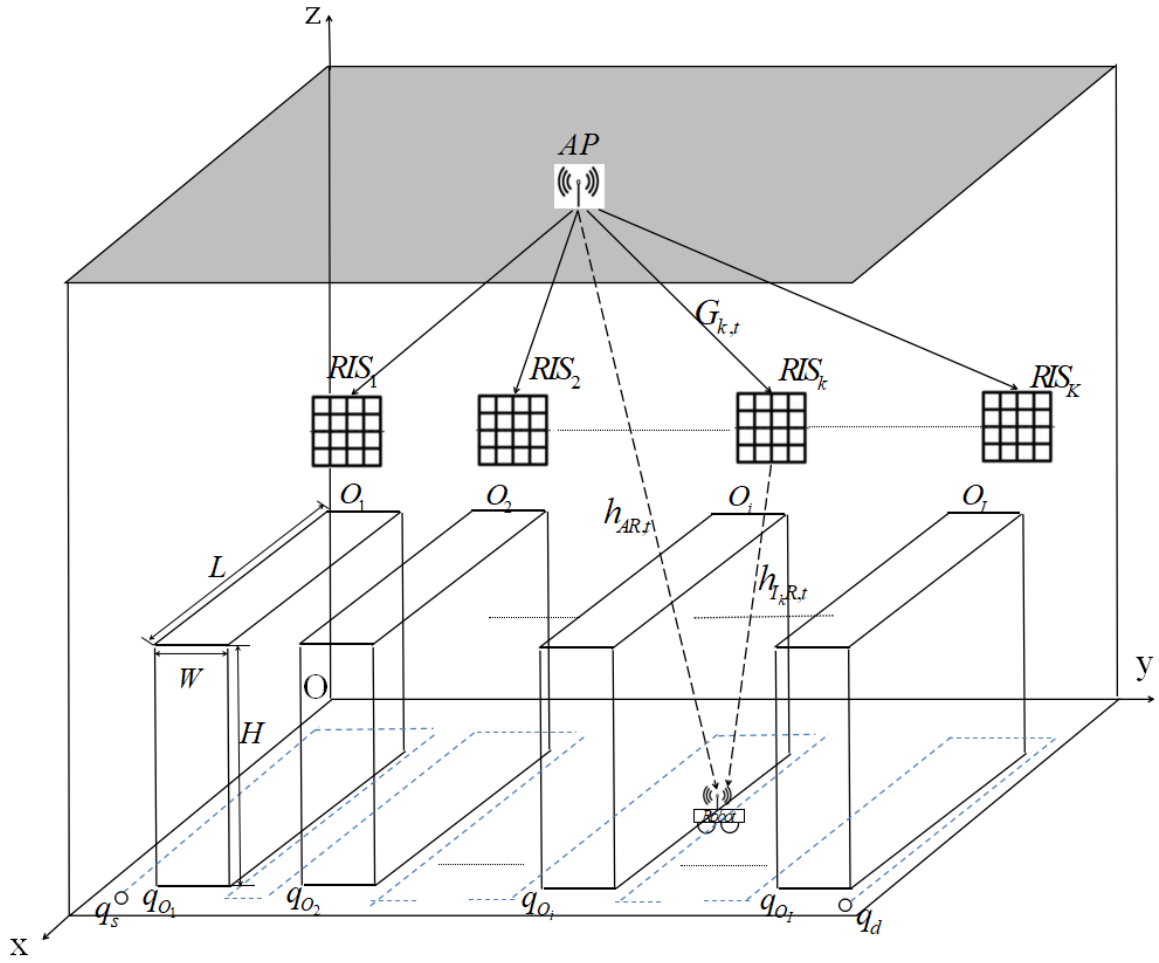

Figure IV.1: System Model.

LoS indicator matrix at timeslot t:

$$\boldsymbol{\mu}^{(t)} = \begin{bmatrix} \mu_{10}^{(t)}, \mu_{11}^{(t)}, \cdots, \mu_{1K}^{(t)} \\ \mu_{20}^{(t)}, \mu_{21}^{(t)}, \cdots, \mu_{2K}^{(t)} \\ \vdots \quad \vdots \quad \vdots \\ \mu_{I0}^{(t)}, \mu_{I1}^{(t)}, \cdots, \mu_{IK}^{(t)} \end{bmatrix} \tag{IV.1}$$

where $\mu_{i0}^{(t)} = 1$ if the LoS link between the AP and the robot is not blocked by the i-th obstacle at timeslot t, otherwise $\mu_{i0}^{(t)} = 0$; $\mu_{ik}^{(t)} = 1$ $(k = 1, \cdots, K)$ if the LoS link between RIS_k and the robot is not blocked by the i-th obstacle at timeslot t, otherwise $\mu_{ik}^{(t)} = 0$. We use a ray-slope method, as shown in Algorithm 1, to identify intersections between the $K + 1$ links and the I obstacles at timeslot t [20], and obtain the LoS indicator matrix.

Algorithm 1 LoS Indicator Vector

Input: q_A, $\boldsymbol{q}_R$, $\boldsymbol{q}_O$, q_t
Output: $\mu_{ik}^{(t)}(i = 1, \cdots, I; k = 0, 1, \cdots, K)$

```
Initialize μ_ik^(t) = 0, (i = 1, ..., I; k = 0, ..., K)
for k = 0 to K do
    for i = 1 to I do
        Obtain the slope of the link between the AP and the robot/ the link between
        the k-th RIS and the robot with the input q_a, q_{R_k}, and q_t.
        Obtain the slope of the link between AP/RIS and the corner of the i-th
        obstacle with the input q_A, q_{R_k}, and q_{O_i}
        Obtain μ_ik^(t) by comparing the obtained slopes.
    end for
end for
```

We note that the system model in Section II-A can be generalized by allowing each obstacle to have its distinct length, width and height, and by allowing different distances between different pairs of adjacent obstacles. In this way, the modeled obstacles can be of various sizes and do not necessarily locate along a straight line. The proposed

Algorithm 1 can still obtain the LoS indicator matrix under such a more general setting of obstacles as long as the trajectory of the robot and the locations and sizes of the obstacles are pre-determined.

IV.2.3 Channel Model

The channels from the AP to RIS_k, from the AP to the robot, and from RIS_k to the robot at timeslot t are denoted by $\boldsymbol{G}_k \in \mathbb{C}^{\frac{N}{K}\times M}$, $\boldsymbol{h}_{AR}^{(t)} \in \mathbb{C}^{1\times M}$, and $\boldsymbol{h}_{kR}^{(t)} \in \mathbb{C}^{\frac{N}{K}\times 1}$, respectively. Accordingly, $\boldsymbol{G}_k$ is given by [21]

$$\boldsymbol{G}_k = \sqrt{\rho d_{Ak}^{-2}} e^{-j2\pi\tau_{Ak}} \boldsymbol{c}_r(\mathcal{V}_{Ak}^{AoA}) \boldsymbol{c}_t^H(\mathcal{V}_{Ak}^{AoD}), \tag{IV.2}$$

where ρ (<1) denotes the LoS path loss at the reference distance of 1 m, d_{Ak} denotes the distance between the AP and RIS_k, τ_{Ak} is the time of arrival (ToA) from the AP to RIS_k, $\boldsymbol{c}_r(\mathcal{V}_{Ak}^{AoA})$ and $\boldsymbol{c}_t(\mathcal{V}_{Ak}^{AoD})$ are respectively given by

$$\boldsymbol{c}_r(\mathcal{V}_{Ak}^{AoA}) = \left[1, \exp\left(\frac{j\pi d_A \sin\mathcal{V}_{Ak}^{AoA}}{\lambda_{AI}}\right), \cdots, \exp\left(\frac{j\pi d_A (\frac{N}{K}-1)\sin\mathcal{V}_{Ak}^{AoA}}{\lambda_{AI}}\right)\right]^T, \tag{IV.3}$$

$$\boldsymbol{c}_t(\mathcal{V}_{Ak}^{AoD}) = \left[1, \exp\left(\frac{j\pi d_A \sin\mathcal{V}_{Ak}^{AoD}}{\lambda_{AI}}\right), \cdots, \exp\left(\frac{j\pi d_A (M-1)\sin\mathcal{V}_{Ak}^{AoD}}{\lambda_{AI}}\right)\right]^T, \tag{IV.4}$$

where $\mathcal{V}_{Ak}^{AoA}$ and $\mathcal{V}_{Ak}^{AoD}$ are the angle of arrival (AoA) at RIS_k from the AP and the angle of departure (AoD) at the AP towards RIS_k, respectively, d_A is the spacing between any two adjacent antennas at the AP, and λ_{AI} is the wavelength of the signal transmitted from the AP to RIS_k.

Similarly, $\boldsymbol{h}_{AR}^{(t)}$ is given by

$$h_{AR}^{(t)} = \begin{cases} \sqrt{\rho (d_{AR}^{(t)})^{-2}} e^{-j2\pi\tau_{AR}^{(t)}} \boldsymbol{c}_t^H(\mathcal{V}_{AR}^{AoD(t)}), & \mu_{i0}^{(t)} = 1, i = 1, \cdots, I \\ \sqrt{\rho (d_{AR}^{(t)})^{-\beta_{AR}}} e^{-j2\pi\tau_{AR}^{(t)}} \tilde{h}, & otherwise \end{cases}, \tag{IV.5}$$

where $d_{AR}^{(t)}$ denotes the distance between the AP and the robot at timeslot t, β_{AR} is the path loss exponent of the NLoS channel between the AP and the robot, $\tau_{AR}^{(t)}$ is the ToA from the AP to the robot at timeslot t, and $\tilde{\boldsymbol{h}} \sim \mathcal{CN}(0,1)$ is a $1 \times M$ vector whose elements follow independent complex Gaussian distribution with zero mean and unit variance, and $\boldsymbol{c}_t(\mathcal{V}_{AR}^{AoD(t)})$ is given by

$$\boldsymbol{c}_t(\mathcal{V}_{AR}^{AoD(t)}) = \left[1, \exp\left(\frac{j\pi d_A \sin \mathcal{V}_{AR}^{AoD(t)}}{\lambda_{AR}^{(t)}}\right), \cdots, \exp\left(\frac{j\pi d_A (M-1) \sin \mathcal{V}_{AR}^{AoD(t)}}{\lambda_{AR}^{(t)}}\right)\right]^T, \tag{IV.6}$$

where $\mathcal{V}_{AR}^{AoD(t)}$ is the AoD at the AP towards RIS_k at timeslot t, and $\lambda_{AR}^{(t)}$ can be expressed as:

$$\lambda_{AR}^{(t)} = \frac{c}{f_c + \frac{f_c v_t \cos(\phi_{AR}^{(t)})}{c}}, \tag{IV.7}$$

where f_c is the carrier frequency of the AP transmission, v_t is the velocity of the robot at timeslot t, $\phi_{AR}^{(t)}$ is the angle between the AP signal's AoA at the robot and the direction of the robot's motion, and c is the speed of light.

Similarly, $\boldsymbol{h}_{kR}^{(t)}$ is given by

$$h_{kR}^{(t)} = \begin{cases} \sqrt{\rho (d_{kR}^{(t)})^{-2}} e^{-j2\pi\tau_{kR}^{(t)}} \boldsymbol{c}_t(\mathcal{V}_{kR}^{AoD}), \ \mu_{ik}^{(t)} = 1, i = 1, \cdots, I \\ \sqrt{\rho (d_{kR}^{(t)})^{-\beta_{kR}}} e^{-j2\pi\tau_{kR}^{(t)}} \tilde{h}, \qquad otherwise \end{cases}, \tag{IV.8}$$

where $d_{kR}^{(t)}$ denotes the distance between RIS_k and the robot at timeslot t, β_{kR} is the path loss exponent of the NLoS channel between RIS_k and the robot, $\tau_{kR}^{(t)}$ is the ToA from RIS_k to the robot, and $\boldsymbol{c}_t(\mathcal{V}_{kR}^{AoD(t)})$ is given by

$$\boldsymbol{c}_t(\mathcal{V}_{kR}^{AoD(t)}) = \left[1, \exp\left(\frac{j\pi d_I \sin \mathcal{V}_{kR}^{AoD(t)}}{\lambda_{kR}^{(t)}}\right), \cdots, \exp\left(\frac{j\pi d_I (\frac{N}{K}-1) \sin \mathcal{V}_{kR}^{AoD(t)}}{\lambda_{kR}^{(t)}}\right)\right]^T, \tag{IV.9}$$

where $\mathcal{V}_{kR}^{AoD(t)}$ is the AoD at the AP at timeslot t, d_I is the spacing between any two adjacent antennas at an RIS. $\lambda_{kR}^{(t)}$ is the wavelength of the siganl reflected by RIS_k

to the robot at timeslot t and can be expressed as

$$\lambda_{kR}^{(t)} = \frac{c}{f_c + \frac{f_c v_t \cos(\phi_{kR}^{(t)})}{c}}, \tag{IV.10}$$

where $\phi_{kR}^{(t)}$ is the angle between the AoA of the signal reflected by RIS_k to the robot and the direction of the robot's motion.

The channel from the AP to the robot at timeslot t is given by

$$\boldsymbol{h}^{(t)} = \sum_{k=1}^{K} (\boldsymbol{h}_{kR}^{(t)})^H \boldsymbol{\Theta}_k^{(t)} \boldsymbol{G}_k^{(t)} + \boldsymbol{h}_{AR}^{(t)}, \quad t = 0, \cdots, T, \tag{IV.11}$$

where the diagonal matrix $\boldsymbol{\Theta}_k^{(t)} = diag(\eta_{k,1}^{(t)} e^{j\theta_{k,1}^{(t)}}, \cdots, \eta_{k,\frac{N}{K}}^{(t)} e^{j\theta_{k,\frac{N}{K}}^{(t)}})$ (j denotes the imaginary unit) is the reflection-coefficients matrix of RIS_k at timeslot t, $\theta_{k,n}^{(t)} \in [0, 2\pi)$ and $\eta_{k,n}^{(t)} \in [0, 1]$ denote the phase shift and the reflection coefficient amplitude of the n-th element of the k-th RIS, respectively. For simplicity, we assume $\eta_{k,n}^{(t)} = 1, \forall n, k, t$, since the reflection coefficient amplitudes are typically set at their maximum value [6], and accordingly $\boldsymbol{\Theta}_k^{(t)} = diag(e^{j\theta_{k,1}^{(t)}}, \cdots, e^{j\theta_{k,\frac{N}{K}}^{(t)}})$.

We consider linear transmit precoding at the AP. At timeslot t ($t = 0, \cdots, T$), the signal transmitted by the AP can be expressed as $\boldsymbol{u}^{(t)} = \boldsymbol{w}^{(t)} s^{(t)}$, where $s^{(t)}$ is the information symbol with a zero mean and unit variance (i.e., normalized power), $\boldsymbol{w}^{(t)} = \sqrt{P^{(t)}} \hat{\boldsymbol{w}}^{(t)}$ is the AP's beamforming vector at timeslot t, $\hat{\boldsymbol{w}}^{(t)} \in \mathbb{C}^{M \times 1}$ denotes the transmit beamforming direction vector, and $P^{(t)}$ is the transmit power of the AP at timeslot t. For given phase shifts $\boldsymbol{\Theta}_k^{(t)}$ of the k-th RIS at timeslot t, $k = 1, \cdots, K$, $\hat{\boldsymbol{w}}^{(t)}$ is given by [22]

$$\hat{\boldsymbol{w}}^{(t)} = \frac{\left(\boldsymbol{h}^{(t)}\right)^H}{\|\boldsymbol{h}^{(t)}\|}. \tag{IV.12}$$

The signal received by the robot at timeslot t is expressed as

$$y^{(t)} = \boldsymbol{h}^{(t)}\boldsymbol{w}^{(t)}s^{(t)} + n^{(t)}, \quad t = 0, \cdots, T, \tag{IV.13}$$

where $n^{(t)} \sim \mathcal{CN}(0, \sigma^2)$ denotes the additive white Gaussian noise (AWGN) at the robot at timeslot t. Accordingly, the SNR received at the robot at timeslot t is given by

$$SNR^{(t)} = \frac{\left|\boldsymbol{h}^{(t)}\boldsymbol{w}^{(t)}\right|^2}{\left|n^{(t)}\right|^2}, \quad t = 0, \cdots, T. \tag{IV.14}$$

IV.3 Problem Formulation and Solution Algorithms

We formulate an optimization problem to minimize the total transmission energy consumption at the AP by jointly optimizing the number and locations of RISs, reflection-coefficients at RISs, and the beamforming vector at the AP, subject to a minimum received SNR constraint at the robot throughout its trajectory, i.e.,

$$(P1): \min_{K, q_{R_1}, \cdots, q_{R_K}, \boldsymbol{\Theta}_1^{(t)}, \cdots, \boldsymbol{\Theta}_K^{(t)}, \boldsymbol{w}^{(t)}} \sum_{t=0}^{T} \left\|\boldsymbol{w}^{(t)}\right\|^2 \tag{IV.15}$$

$$s.t.\ C1: 0 \leqslant \theta_{k,n}^{(t)} < 2\pi,\ \forall k,\ \forall n,\ \forall t, \tag{IV.15a}$$

$$C2: SNR^{(t)} \geqslant \gamma,\ \forall t, \tag{IV.15b}$$

$$C3: K \geqslant 1, \tag{IV.15c}$$

$$C4: 0 \leqslant P^{(t)} \leqslant P_{max},\ \forall t, \tag{IV.15d}$$

$$C5: x_{R_k} = 0, y_{R_k} \in [0, l_f], z_{R_k} \in [z_r, h_{ce}],\ \forall k, \tag{IV.15e}$$

where $\gamma > 0$ is the minimum SNR requirement of the robot, K is the number of RISs, $q_{Rk} = [x_{R_k}, y_{R_k}, z_{R_k}]$ is the position of the k-th RIS, $k = 1, \cdots, K$, P_{max} is the maximum transmit power at the AP, and h_{ce} is the height of the ceiling. The objective function $\sum_{t=0}^{T} \left\|\boldsymbol{w}^{(t)}\right\|^2$ is the total transmission energy consumption of the AP during the robot's journey. Constraint $C1$ imposes the value range of the phase shift for each element on the RISs, $C2$ ensures that the received SNR of the robot at each time slot is above the minimum SNR required, $C3$ ensures that at least one RIS will be deployed, $C4$ specifies the upper and lower bounds of the transmit power at the AP, and $C5$ is the constraint on the location of each RIS.

IV.3.1 TECO Algorithm

We note that it is hard to solve $(P1)$ directly due to the varying number of variables involved. We first study the case with the number K and the locations of RISs fixed, for which $(P1)$ reduces to

$$(P2): \min_{\boldsymbol{\Theta}_1^{(t)}, \cdots, \boldsymbol{\Theta}_K^{(t)}, \boldsymbol{w}^{(t)}} \sum_{t=0}^{T} \left\|\boldsymbol{w}^{(t)}\right\|^2 \tag{IV.16}$$
$$s.t.\ C1, C2, C4.$$

Since $\boldsymbol{w}^{(t)}$ and $\boldsymbol{\Theta}_k^{(t)}$ are independent for different t, the objective function of $(P2)$ is minimized when each $\left\|\boldsymbol{w}^{(t)}\right\|^2$ in the summation from $t = 0$ to $t = T$ is minimized. According to the above and substituting $\boldsymbol{w}^{(t)} = \sqrt{P^{(t)}}\hat{\boldsymbol{w}}^{(t)}$ into (IV.16), $(P2)$ can be equivalently rewritten as

$$(P3): \min_{\boldsymbol{\Theta}_1^{(t)}, \cdots, \boldsymbol{\Theta}_K^{(t)}, P^{(t)}, \hat{\boldsymbol{w}}^{(t)}} P^{(t)} \left\|\hat{\boldsymbol{w}}^{(t)}\right\|^2,\ \forall t \in \{0, \cdots, T\} \tag{IV.17}$$
$$s.t.\ C1, C2, C4.$$

Although $(P3)$ is still a non-convex problem and is difficult to solve directly, since $\left\|\hat{\boldsymbol{w}}^{(t)}\right\|^2 = 1$, we can obtain the optimal transmit power of the AP by substituting (IV.14) into (IV.15b) and solving the resulting inequality for $P^{(t)}$. Thus, the optimal transmit power of the AP is given by

$$P_{\text{opt}}^{(t)} = \frac{\gamma|n(t)|^2}{\left\|(\sum_{k=1}^{K} \boldsymbol{h}_{kR}^{(t)\,H} \boldsymbol{\Theta}_k^{(t)} \boldsymbol{G}_k^{(t)} + \boldsymbol{h}_{AR}^{(t)\,H})\hat{\boldsymbol{w}}^{(t)}\right\|^2}. \tag{IV.18}$$

By substituting (IV.18) into $(P3)$ and assuming that the AP's maximum transmit power P_{max} is sufficiently large (and hence $C4$ can be ignored for analytical tractability), we have

$$(P4): \min_{\boldsymbol{\Theta}_1^{(t)},\cdots,\boldsymbol{\Theta}_K^{(t)},\hat{\boldsymbol{w}}^{(t)}} \frac{\gamma|n(t)|^2}{\left\|(\sum_{k=1}^{K} \boldsymbol{h}_{kR}^{(t)\,H} \boldsymbol{\Theta}_k^{(t)} \boldsymbol{G}_k^{(t)} + \boldsymbol{h}_{AR}^{(t)\,H})\hat{\boldsymbol{w}}^{(t)}\right\|^2} \tag{IV.19}$$

$$,\forall t \in \{0,\cdots,T\}$$

$$s.t.\ C1, C2.$$

Please note that $C4$ will be considered in our proposed Algorithm 2 (which will be presented later in this section) to ensure that the optimized transmit power of the AP does not go beyond its maximum allowed transmit power.

In order to solve $(P4)$, we divide it into two sub-problems $\hat{\boldsymbol{w}}^{(t)}$ and by fixing $\boldsymbol{\Theta}_k^{(t)}$ $(k = 1,\cdots,K, t = 0,\cdots,T)$ in $(P4)$, respectively, as detailed below.

For a given $\hat{\boldsymbol{w}}^{(t)}$, $(P4)$ is equivalent to

$$(P5): \max_{\boldsymbol{\Theta}_1^{(t)},\cdots,\boldsymbol{\Theta}_K^{(t)}} \left\| (\sum_{k=1}^{K} \boldsymbol{h}_{kR}^{(t)\,H} \boldsymbol{\Theta}_k^{(t)} \boldsymbol{G}_k^{(t)} + \boldsymbol{h}_{AR}^{(t)\,H}) \hat{\boldsymbol{w}}^{(t)} \right\|^2 , \ \forall t \in \{0, \cdots, T\} \tag{IV.20}$$

$$s.t.\ C1, C2$$

According to the triangle inequality, we have

$$\begin{aligned} &\left\| (\sum_{k=1}^{K} \boldsymbol{h}_{kR}^{(t)\,H} \boldsymbol{\Theta}_k^{(t)} \boldsymbol{G}_k^{(t)} + \boldsymbol{h}_{AR}^{(t)\,H}) \hat{\boldsymbol{w}}^{(t)} \right\| \\ \leqslant &\left\| \boldsymbol{h}_{1R}^{(t)\,H} \boldsymbol{\Theta}_1^{(t)} \boldsymbol{G}_1^{(t)} \hat{\boldsymbol{w}}^{(t)} \right\| + \left\| \boldsymbol{h}_{2R}^{(t)\,H} \boldsymbol{\Theta}_2^{(t)} \boldsymbol{G}_2^{(t)} \hat{\boldsymbol{w}}^{(t)} + , \cdots , \right. \\ &\left. + \boldsymbol{h}_{KR}^{(t)\,H} \boldsymbol{\Theta}_K^{(t)} \boldsymbol{G}_K^{(t)} \hat{\boldsymbol{w}}^{(t)} + \boldsymbol{h}_{AR}^{(t)\,H} \hat{\boldsymbol{w}}^{(t)} \right\|. \end{aligned} \tag{IV.21}$$

The equality in (IV.21) holds if and only if

$$\begin{aligned} &\arg(\boldsymbol{h}_{1R}^{(t)\,H} \boldsymbol{\Theta}_1^{(t)} \boldsymbol{G}_1^{(t)} \hat{\boldsymbol{w}}^{(t)}) \\ =&\arg(\boldsymbol{h}_{2R}^{(t)\,H} \boldsymbol{\Theta}_2^{(t)} \boldsymbol{G}_2^{(t)} \hat{\boldsymbol{w}}^{(t)}) + , \cdots , + \\ &\arg(\boldsymbol{h}_{KR}^{(t)\,H} \boldsymbol{\Theta}_K^{(t)} \boldsymbol{G}_K^{(t)} \hat{\boldsymbol{w}}^{(t)}) + \arg(\boldsymbol{h}_{AR}^{(t)\,H} \hat{\boldsymbol{w}}^{(t)}) \\ \triangleq &\Phi_1^{(t)}, \end{aligned} \tag{IV.22}$$

where $\arg(\boldsymbol{x})$ gives the phases of the elements of $\boldsymbol{x}$.

For given $\Theta_2^{(t)}, \cdots, \Theta_K^{(t)}$ (and thus given $\Phi_1^{(t)}$), letting $\boldsymbol{h}_{1R}^{(t)\,H} \boldsymbol{\Theta}_1^{(t)} \boldsymbol{G}_1^{(t)} \hat{\boldsymbol{w}}^{(t)} = \boldsymbol{\Theta}_1^{(t)\,H} \boldsymbol{R}_1^{(t)}$, where $\boldsymbol{R}_1^{(t)} = diag(\boldsymbol{h}_{1R}^{(t)\,H}) \boldsymbol{G}_1^{(t)} \hat{\boldsymbol{w}}^{(t)}$, and substituting (IV.21) under the condition of

(IV.22) into ($P5$), we have

$$(P6): \max_{\boldsymbol{\Theta}_1^{(t)}} \left\| {\boldsymbol{\Theta}_1^{(t)}}^H \boldsymbol{R}_1^{(t)} \right\|^2, \ \forall t \in \{0, \cdots, T\} \tag{IV.23}$$

$$s.t. \qquad C1$$

$$C6: \arg({\boldsymbol{\Theta}_1^{(t)}}^H \boldsymbol{R}_1^{(t)}) = \Phi_1^{(t)}. \tag{IV.23a}$$

According to (IV.22), we can show that the optimal solution to ($P6$) is given by

$$\boldsymbol{\Theta}_{1\text{opt}}^{(t)} = e^{j(\Phi_1^{(t)} - \arg(\boldsymbol{R}_1^{(t)}))}, \tag{IV.24}$$

which suggests that the phase shifts of RIS_1 should be tuned according to the beamforming of the AP and the phase shifts of RIS_k, $k = 2, \cdots, K$.

Following the similar procedures as above, the optimal phase shifts of $\text{RIS}_k (k = 2, \cdots, K)$ can be obtained as

$$\boldsymbol{\Theta}_{k\text{opt}}^{(t)} = e^{j(\Phi_k^{(t)} - \arg(\boldsymbol{R}_k^{(t)}))}, \tag{IV.25}$$

where $\boldsymbol{R}_k^{(t)} = diag({\boldsymbol{h}_{kR}^{(t)}}^H)\boldsymbol{G}_k^{(t)}\hat{\boldsymbol{w}}^{(t)}$ and $\Phi_k^{(t)}$ is given by

$$\begin{aligned} &\Phi_k^{(t)} \\ \triangleq &\arg({\boldsymbol{h}_{1R}^{(t)}}^H \boldsymbol{\Theta}_1^{(t)} \boldsymbol{G}_1^{(t)} \hat{\boldsymbol{w}}^{(t)}) + , \cdots, + \\ &\arg({\boldsymbol{h}_{(k-1)R}^{(t)}}^H \boldsymbol{\Theta}_{k-1}^{(t)} \boldsymbol{G}_{k-1}^{(t)} \hat{\boldsymbol{w}}^{(t)}) \\ &+ \arg({\boldsymbol{h}_{(k+1)R}^{(t)}}^H \boldsymbol{\Theta}_{k+1}^{(t)} \boldsymbol{G}_{k+1}^{(t)} \hat{\boldsymbol{w}}^{(t)}) + , \cdots, + \\ &\arg({\boldsymbol{h}_{KR}^{(t)}}^H \boldsymbol{\Theta}_K^{(t)} \boldsymbol{G}_K^{(t)} \hat{\boldsymbol{w}}^{(t)}) + \arg({\boldsymbol{h}_{AR}^{(t)}}^H \hat{\boldsymbol{w}}^{(t)}) \end{aligned} \tag{IV.26}$$

For given $\mathbf{\Theta}_k^{(t)}, k = 1, \cdots, K, t \in \{0, \cdots, T\}$, $(P4)$ converts to

$$(P7): \max_{\hat{\boldsymbol{w}}^{(t)}} \left\| (\sum_{k=1}^{K} \boldsymbol{h}_{kR}^{(t)\,H} \mathbf{\Theta}_k^{(t)} \boldsymbol{G}_k^{(t)} + \boldsymbol{h}_{AR}^{(t)\,H}) \hat{\boldsymbol{w}}^{(t)} \right\|^2 \quad , \ \forall t \in \{0, \cdots, T\} \tag{IV.27}$$

$$s.t. \quad C2$$

Based on (IV.14) and (IV.15b), we solve $(P7)$ and obtain the optimal transmit beamforming direction vector $\hat{\boldsymbol{w}}_{\text{opt}}^{(t)}$ of the AP as [22]

$$\hat{\boldsymbol{w}}_{\text{opt}}^{(t)} = \frac{\left(\sum\limits_{k=1}^{K} \boldsymbol{h}_{kR}^{(t)\,H} \mathbf{\Theta}_k^{(t)} \boldsymbol{G}_k^{(t)} + \boldsymbol{h}_{AR}^{(t)\,H} \right)^H}{\left\| \sum\limits_{k=1}^{K} \boldsymbol{h}_{kR}^{(t)\,H} \mathbf{\Theta}_k^{(t)} \boldsymbol{G}_k^{(t)} + \boldsymbol{h}_{AR}^{(t)\,H} \right\|}. \tag{IV.28}$$

We can obtain the optimal transmit power $P_{\text{opt}}^{(t)}$ of the AP by substituting (IV.24), (IV.25), and (IV.28) into (IV.18).

Based on the above solutions to the two subproblems $(P5)$ and $(P7)$, we propose an iterative algorithm that solves $(P5)$ and $(P7)$ alternately in each iteration to minimize the total energy consumption at the AP, i.e., the TECO algorithm as presented in Algorithm 2. In each iteration, according to (21) and (22), calculating (24) or (25) guarantees that the objective function of (P5) is non-decreasing, and calculating (28) guarantees that the objective function of (P7) is non-decreasing [22]. As a result, after each iteration, the objective function value of (P4) is non-increasing. Since there is a lower bound of the objective function of $(P4)$ given by $C2$, the objective function of $(P4)$ will decrease after each iteration until its convergence. In Algorithm 2, solving $(P5)$ has a complexity of $\mathcal{O}(\frac{N}{K} \times K) = \mathcal{O}(N)$, where N is the total number of passive

Algorithm 2 TECO Algorithm

Input: $\boldsymbol{h}_{kR}^{(t)}, \boldsymbol{G}_{k}^{(t)}, \boldsymbol{h}_{AR}^{(t)}, \boldsymbol{q}_{R}$
Output: $\hat{\boldsymbol{w}}_{\text{opt}}^{(t)}, \boldsymbol{\Theta}_{k\text{opt}}^{(t)}, P_{\text{opt}}^{(t)}$

```
Set the iteration index s = 1 and initialize the AP's transmit beamforming direction ŵ^(t)_opt(s).
Initialize the RIS phase shifts Θ^(t)_k(s), k = 1, ..., K.
Obtain P^(t)_opt(s) according to (IV.18).
repeat
    Update s = s + 1.
    Obtain Θ^(t)_k(s), k = 1, ..., K, using (IV.24) or (IV.25).
    Obtain ŵ^(t)_opt(s) according to (IV.28).
    Obtain P^(t)_opt(s) according to (IV.18).
    P^(t)_opt(s) = min{ P^(t)_opt(s), P_max }
until P^(t)_opt(s-1) − P^(t)_opt(s) < ε.
ŵ^(t)_opt = ŵ^(t)_opt(s), Θ^(t)_kopt = Θ^(t)_k(s), P^(t)_opt = P^(t)_opt(s), k = 1, ..., K.
```

reflecting elements of all the RISs, while solving $(P7)$ has a complexity of $\mathcal{O}(M)$, where M is the number of antennas at the AP. Thus, Algorithm 2 has a complexity of $\mathcal{O}(N_I(M+N))$, where N_I is the number of iterations required for convergence.

IV.3.2 RISLN Algorithm

In order to optimize the number and locations of RISs, we divide the wall area where the RISs are deployed into a grid of $\lceil \frac{l_f \times (l_h - z_r)}{d_u^2} \rceil$ equal rectangular units, where l_f is the length of the wall, l_h is the height of the wall, z_r is the height of the robot antenna, and d_u^2 is approximately the size of each RIS. We assume that each RIS is deployed in one of the units and no more than one RIS can be deployed in any unit. Hence, the location of the k-th RIS, $q_{Rk}, \forall k \in \{1, \cdots, K\}$, can be uniquely represented by a sequence of $b = \lceil \log_2(\frac{l_f \times (l_h - z_r)}{d_u^2}) \rceil$ binary bits.

Given I obstacles in the considered indoor environment, we can show that there is no need to deploy more than $I+1$ RISs to ensure the robot seeing a LoS link from at

least one RIS or the AP at all times along its trajectroy. For each $K \in \{1, \cdots, I+1\}$, we employ Algorithm 2 and the Genetic Algorithm [23] to optimize the locations of the K RISs as follows. First, set the iteration index $s' = 1$, and randomly initialize a population of N_{ind} individuals, where N_{ind} is an even number and each individual contains a binary bit sequence $\boldsymbol{q}_R = [q_{R_1}, q_{R_2}, \cdots, q_{R_K}]$ that represents the locations of K RISs. Then, Algorithm 2 is used to obtain $\hat{\boldsymbol{w}}_{\text{opt}}^{(t)}, \boldsymbol{\Theta}_{k\text{opt}}^{(t)}, P_{\text{opt}}^{(t)}$, $t \in \{0, \cdots, T\}$, $k \in \{1, \cdots, K\}$ for each individual and $\sum_{t=0}^{T} P_{\text{opt}}^{(t)}$ is taken as the fitness value of the corresponding individual.

Update $s' = s' + 1$, and a new population of N_{ind} individuals are generated from the current population by the Roulette Wheel Selection scheme [23], where each individual has a probability of selection proportional to its fitness value. Next, the population generated by Selection is randomly divided into $\frac{N_{\text{ind}}}{2}$ pairs of individuals. For each pair, generate a random number r following a uniform distribution in $(0, 1)$ and swap the $\lfloor (Kb/2) \rfloor$-th to the Kb-th bits between the two individuals if $r \leqslant \mathcal{P}_c$, where $0 < \mathcal{P}_c < 1$ is the Crossover probability. Afterwards, for each individual in the new population generated by Crossover, generate a random number r' following a uniform distribution in $(0, 1)$ and flip every binary bit of the corresponding individual if $r' \leqslant \mathcal{P}_m$, where $0 < \mathcal{P}_m < 1$ is the Mutation probability. Then, for each individual in the new population generated by Mutation, Algorithm 2 is used to obtain $\hat{\boldsymbol{w}}_{\text{opt}}^{(t)}, \boldsymbol{\Theta}_{k\text{opt}}^{(t)}$ and $P_{\text{opt}}^{(t)}$, $t \in \{0, \cdots, T\}, k \in \{1, \cdots, K\}$. The individual that has the smallest fitness value among the population is identified, and its $\hat{\boldsymbol{w}}_{\text{opt}}^{(t)}, \boldsymbol{\Theta}_{k\text{opt}}^{(t)}$ and $P_{\text{opt}}^{(t)}$ are labeled as $\hat{\boldsymbol{w}}_{\text{opt}K(s')}^{(t)}, \boldsymbol{\Theta}_{k\text{opt}K(s')}^{(t)}$ and $P_{\text{opt}K(s')}^{(t)}$, $t \in \{0, \cdots, T\}, k \in \{1, \cdots, K\}$, respectively.

The above Selection, Crossover and Mutation procedures repeat until $\sum_{t=0}^{T} P_{\text{opt}K(s'-1)}^{(t)} - \sum_{t=0}^{T} P_{\text{opt}K(s')}^{(t)} < \varepsilon$, where ε is a positive constant. Once converged, the individual that has the smallest fitness value among the latest population is identified as the optimal locations of K RISs, labeled as $\boldsymbol{q}_{R\text{opt}K}$, and its $\hat{\boldsymbol{w}}_{\text{opt}K(s')}^{(t)}, \boldsymbol{\Theta}_{k\text{opt}K(s')}^{(t)}$ and $P_{\text{opt}K(s')}^{(t)}$ are

labeled as $\hat{\boldsymbol{w}}_{\text{opt}K}^{(t)}, \boldsymbol{\Theta}_{k\text{opt}K}^{(t)}$ and $P_{\text{opt}K}^{(t)}$, $t \in \{0, \cdots, T\}, k \in \{1, \cdots, K\}$, respectively. The above iterative algorithm for each K is ensured to converge when the iteration number is large enough [23].

After the optimized locations of K RISs have been obtained for all $K \in \{1, \cdots, I+1\}$, the value of K that is associated with the lowest value of $\sum_{t=0}^{T} P_{\text{opt}K}^{(t)}$ is identified as the optimal value of K and its corresponding $q_{R\text{opt}K}$, $\sqrt{P_{\text{opt}K}^{(t)}}\hat{\boldsymbol{w}}_{\text{opt}K}^{(t)}$ and $\boldsymbol{\Theta}_{k\text{opt}K}^{(t)}$, $t \in \{0, \cdots, T\}$, $k \in \{1, \cdots, K\}$ return the optimal RIS locations, AP beamforming vectors and RIS phase shifts, respectively.

The above described RIS Locations and Number (RISLN) Algorithm is presented in Algorithm 3. It has a complexity of $\mathcal{O}((T+1)N_I(M+N)N_{\text{ind}}\sum_{K=1}^{I+1} N_{GK})$, where N_{GK} is the number of iterations required for $K \in \{1, \cdots, I+1\}$.

IV.4 Simulation Results

In this section, we present numerical results to verify the proposed algorithms. The parameter values used in the simulation are listed in Table I unless otherwise specified.

Fig. IV.2 shows the transmission energy consumption of the AP versus the iteration number in Algorithm 3. The fluctuation of the curve is due to the use of the Genetic Algorithm that randomly generates a new population of candidate solutions in each iteration. By generating new populations, the genetic algorithm introduces genetic diversity so as to escape local optima by exploring different regions of the solution space, but the AP's transmission energy consumption of a randomly generated new population is not necessarily lower than that of the population obtained in the previous iteration. We can see that Algorithm 3 converges after the 19th iteration.

In the simulation, we compare the performance of Algorithm 3 with the following four benchmark schemes: the evenly distributed RIS deployment scheme proposed

Algorithm 3 RISLN Algorithm

Input: $\mathcal{P}_c, \mathcal{P}_m, N_{\text{ind}}, I$ $(0 < I \leqslant l_f/(l_a + W))$.

Output: K_{opt}, $q_{R\text{opt}K}$, $\sqrt{P_{\text{opt}K}^{(t)}}\hat{\boldsymbol{w}}_{\text{opt}K}^{(t)}$, $\boldsymbol{\Theta}_{k\text{opt}K}^{(t)}$, $t \in \{0, \cdots, T\}$, $k \in \{1, \cdots, K\}$.

1: Initialize the number of RISs $K = 1$.
2: **repeat**
3: Set the iteration index $s' = 1$, and randomly initialize a population of N_{ind} individuals, where each individual is a binary bit sequence $\boldsymbol{q}_R = [q_{R_1}, q_{R_2}, \cdots, q_{R_K}]$. Run Algorithm 2 for $t = 0, \cdots, T$ for each individual and take $\sum_{t=0}^{T} P_{\text{opt}}^{(t)}$ as its fitness value.
4: **repeat**
5: Update $s' = s' + 1$
6: Selection: Obtain a new population of N_{ind} individuals from the current population by the Roulette Wheel Selection scheme [23].
7: Crossover: The new population is randomly divided into $\frac{N_{\text{ind}}}{2}$ pairs. For each pair, randomly generate $r \in (0, 1)$ and swap the $\lfloor (Kb/2) \rfloor$-th to the Kb-th bits between the two individuals if $r \leqslant \mathcal{P}_c$.
8: Mutation: For each individual in the population generated by Crossover, randomly generate $r' \in (0, 1)$ and flip every bit of it if $r' \leqslant \mathcal{P}_m$.
9: Run Algorithm 2 for each individual in the population generated by Mutation. The individual that has the smallest fitness value returns $\hat{\boldsymbol{w}}_{\text{opt}K(s')}^{(t)}$, $\boldsymbol{\Theta}_{k\text{opt}K(s')}^{(t)}$ and $P_{\text{opt}K(s')}^{(t)}$, $t \in \{0, \cdots, T\}$, $k \in \{1, \cdots, K\}$.
10: **until** $\sum_{t=0}^{T} P_{\text{opt}K(s'-1)}^{(t)} - \sum_{t=0}^{T} P_{\text{opt}K(s')}^{(t)} < \varepsilon$.
11: $P_{\text{opt}K}^{(t)} = P_{\text{opt}K(s')}^{(t)}$, $\hat{\boldsymbol{w}}_{\text{opt}K}^{(t)} = \hat{\boldsymbol{w}}_{\text{opt}K(s')}^{(t)}$, $\boldsymbol{\Theta}_{k\text{opt}K}^{(t)} = \boldsymbol{\Theta}_{k\text{opt}K(s')}^{(t)}$, $t \in \{0, \cdots, T\}$, $k \in \{1, \cdots, K\}$.
12: Update $K = K + 1$.
13: **until** $K = I + 2$.
14: $K_{opt} = \underset{K\{1,\cdots,I+1\}}{arg\,min} \left\{ \sum_{t=0}^{T} P_{\text{opt}K}^{(t)} \right\}$ and return its $q_{R\text{opt}K}$, $\sqrt{P_{\text{opt}K}^{(t)}}\hat{\boldsymbol{w}}_{\text{opt}K}^{(t)}$, $\boldsymbol{\Theta}_{k\text{opt}K}^{(t)}$, $t \in \{0, \cdots, T\}$, $k \in \{1, \cdots, K\}$ as output.

Table IV.1: Parameter Values Used in the Simulation

Parameter		Value
l_f	length of the wall where RISs are deployed	$18m$
l_p	length of the wall parallel to obstacle's rows	$20m$
l_h	height of the wall where RISs are deployed	$12m$
I	number of obstacles	3
q_{O_1}	location of Obstacle 1	$[19, 1, 0]m$
q_{O_2}	location of Obstacle 2	$[19, 8, 0]m$
q_{O_3}	location of Obstacle 3	$[19, 15, 0]m$
L	length of each obstacle	$15m$
W	width of each obstacle	$2m$
H	height of each obstacle	$10m$
l_a	distance between two adjacent obstacles	$5m$
l	distance between robot and obstacle	$1m$
q_s	robot's start point	$[19, 0, 0]m$
q_d	robot's destination point	$[19, 18, 0]m$
z_r	height of the robot antenna	$1m$
v_t	speed of the robot	$1m/s$
q_A	location of the AP	$[1, 6, 12]m$
d	AP's spacing between adjacent antennas	$\lambda/2$
M	number of antennas on the AP	5
N	total number of elements on all RISs	90
d_u^2	approximate RIS size used in Algorithm 3	$1cm^2$
$\beta_{AR} = \beta_{kR}$	path loss exponent [25]	4
ρ	LoS path gain [21]	$-30dB$
σ^2	noise power [21]	$-109dBm$
γ	minimum SNR requirement	$10dB$
f_c	carrier frequency	$60GHz$
$\mathcal{P}_c$	crossover probability	0.6
$\mathcal{P}_m$	mutation probability	0.01
N_{ind}	number of individuals in a population	20
ε	convergence threshold	0.001

in [24], where the RISs are evenly spaced on the wall at the same height, and the number and the height of RISs are the optimal results obtained by Algorithm 3; the centralized deployment (i.e., a single RIS) with the optimal location of the RIS obtained by Algorithm 3 for $K = 1$; the centralized deployment of one RIS at the centre of the wall; and the case without deploying any RIS. For all the RIS deployment schemes

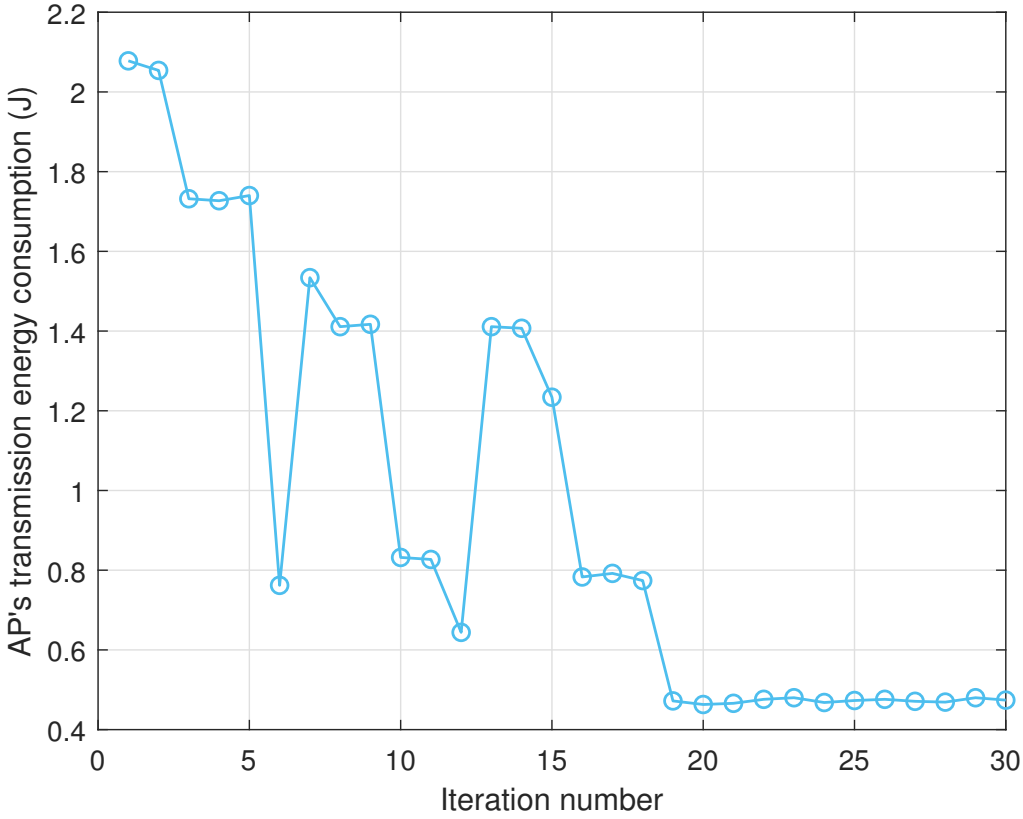

Figure IV.2: Transmission energy consumption of the AP versus the iteration number.

under comparison, the RISs are deployed on the same wall as shown in Fig. 1. The specific locations of RISs for the four RIS deployment schemes are indicated in Fig. IV.3.

Fig. IV.4 plots the AP's transmission energy consumption versus the minimum required SNR at the robot. The optimal number of RISs obtained by the proposed algorithm is $K_{opt} = 3$. As shown in Fig. IV.4, the transmission energy consumption at the AP increases when the minimum required SNR at the robot increases, since a higher target SNR at the robot requires higher transmit power at the AP at each timeslot. The optimal RIS deployment obtained by Algorithm 3 achieves the lowest energy consumption at the AP among all the considered schemes. Compared with

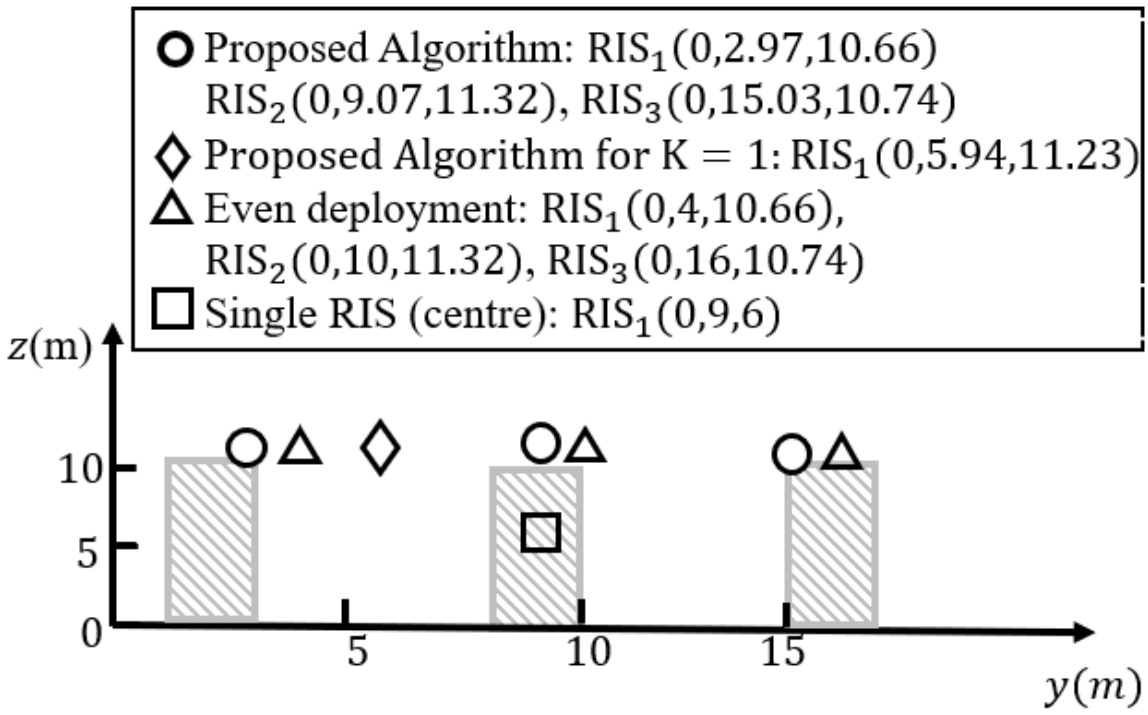

Figure IV.3: Locations of RISs.

the evenly distributed RIS deployment scheme, deploying a single RIS at the optimal location obtained by Algorithm 3 for $K = 1$ leads to a lower energy consumption at the AP. This is because Algorithm 3 optimizes the RIS location while considering the exact locations of obstacles and the robot. Between the two schemes both without optimizing the RIS location, the evenly distributed deployment outperforms deploying a single RIS at the center of the wall because the multiple distributed RISs make it more likely for the robot to see a LoS link from one of the RISs along the whole trajectory than a single RIS. The case with no RIS always has the highest transmission energy consumption at the AP among all the considered schemes. This indicates that the deployment of RIS can decrease the transmission energy consumption at the AP.

In Fig. IV.5, we plot the transmission energy consumption at the AP versus the total number of elements on RISs. The optimal number of RISs obtained by the proposed algorithm is $K_{opt} = 3$. In addition to the four benchmark shcemes considered

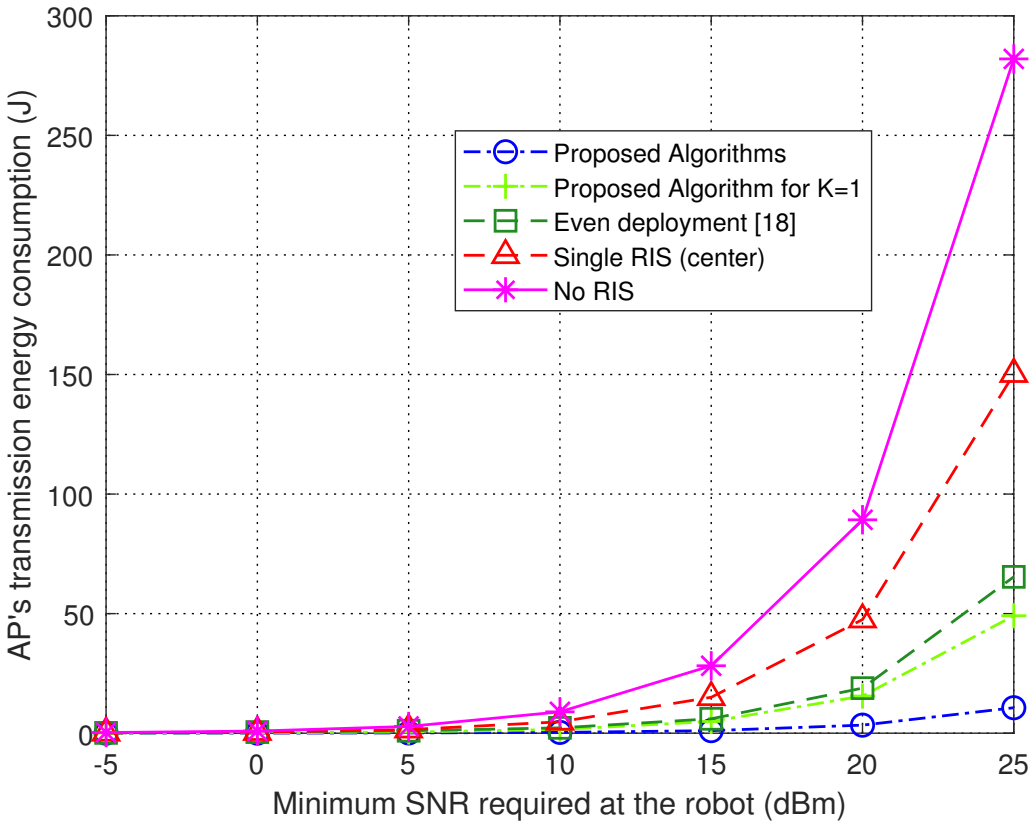

Figure IV.4: AP's transmission energy consumption versus the minimum required SNR at the robot.

in Fig. IV.4, we also plot a curve for the even deployment scheme [24] with $K = 2K_{opt}$. The AP's transmission energy consumption decreases with the total number of elements on RISs under all the considered schemes, because a larger number of elements leads to a larger beamforming gain of the RISs. The proposed algorithm performs the best because the optimized deployment locations of RISs ensure that the robot sees a LoS link from an RIS or the AP throughout its trajectory and the AP can transmit at the lowest possible power at each timeslot. The even deployment scheme for $K = K_{opt}$ achieves a lower transmission energy consumption of the AP than the even deployment scheme for $K = 2K_{opt}$. This indicates that further distributing the fixed total number of elements to more RISs cannot further lower the AP's transmission energy consumption if the whole trajectory has already been covered with LoS links, while less elements per RIS will reduce the beamforming gain of each RIS.

In Fig. IV.6, we plot the transmission energy consumption at the AP versus the carrier frequency of the mmWave signal. The optimal number of RISs obtained by the proposed algorithm is $K_{opt} = 3$. For all the considered schemes, the transmission energy consumption at the AP increases with the carrier frequency of the signal because the signal strength decays faster over distance at a higher carrier frequency. The performance gain of the proposed algorithm over the other schemes becomes larger with the increase of the carrier frequency. This shows the importance of optimizing RIS deployment for indoor downlink transmissions in high mmWave bands.

In Fig. IV.7, we plot the transmission energy consumption at the AP versus the number of obstacles. The transmission energy consumption at the AP increases with the number of obstacles for all the considered schemes because of the robot's longer trajectory. The proposed algorithm, the proposed algorithm for $K = 1$ and the even deployment scheme have the same AP's transmission energy consumption when the number of obstacle is one, because deploying one RIS is enough for the robot to main-

tain a LoS link from the RIS or the AP along the whole trajectory. The even deployment scheme outperforms the proposed algorithm for $K = 1$ when the number of obstacles is four or five, because the centralized deployment scheme keeps the robot seeing a LoS link from the RIS or the AP for fewer timeslots.

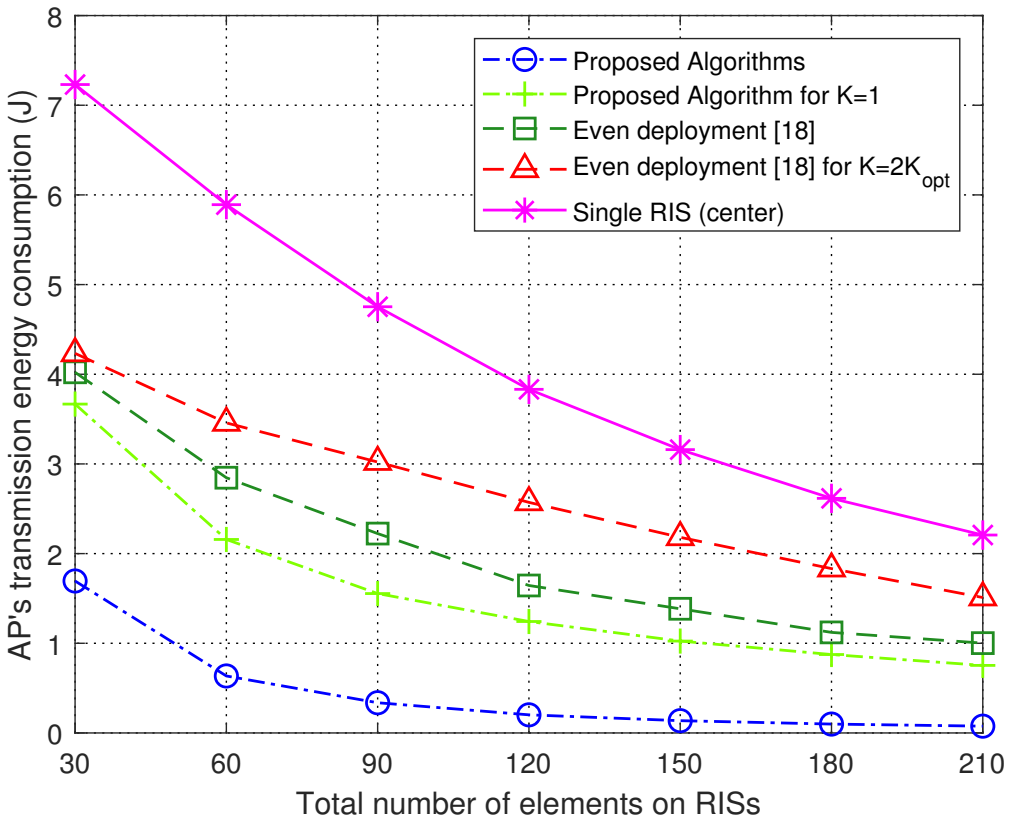

Figure IV.5: AP's transmission energy consumption versus the total number of elements on RISs.

IV.5 Conclusion and Future Work

In this paper, we have studied multiple-RIS-assisted mmWave communications for a robot moving around obstacles along a predefined trajectory inside an industrial building. To minimize the transmission energy consumption at the AP while ensuring the

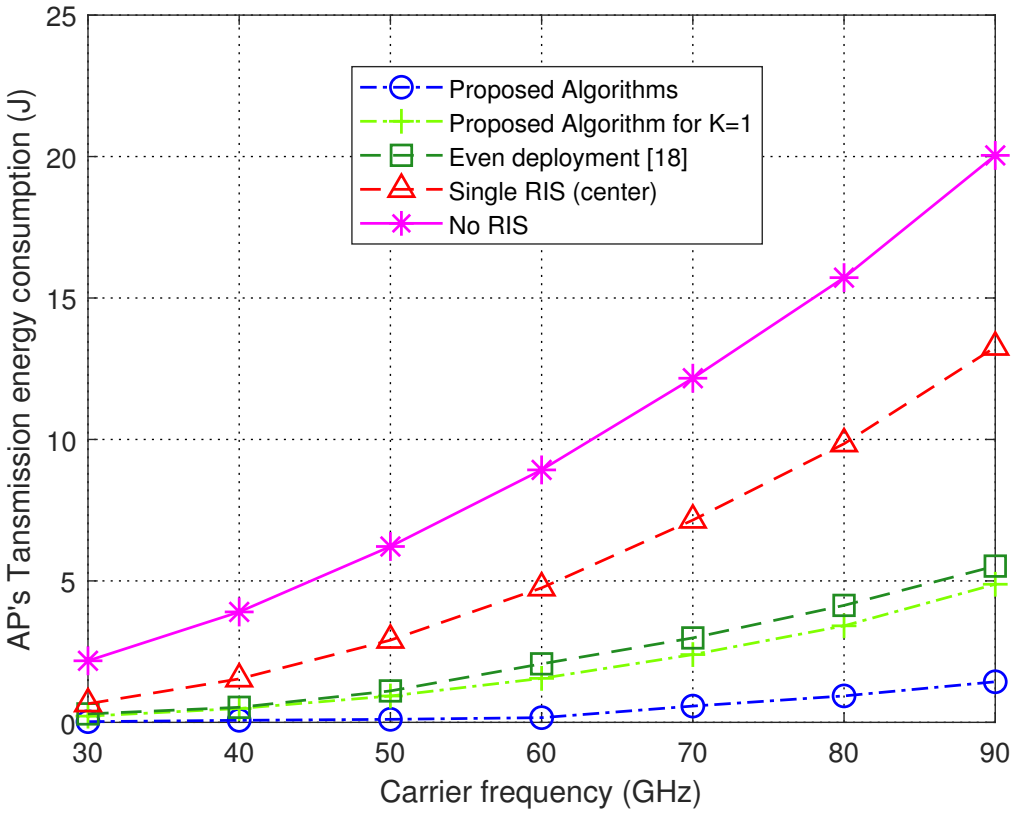

Figure IV.6: AP's transmission energy consumption versus the carrier frequency of the signal.

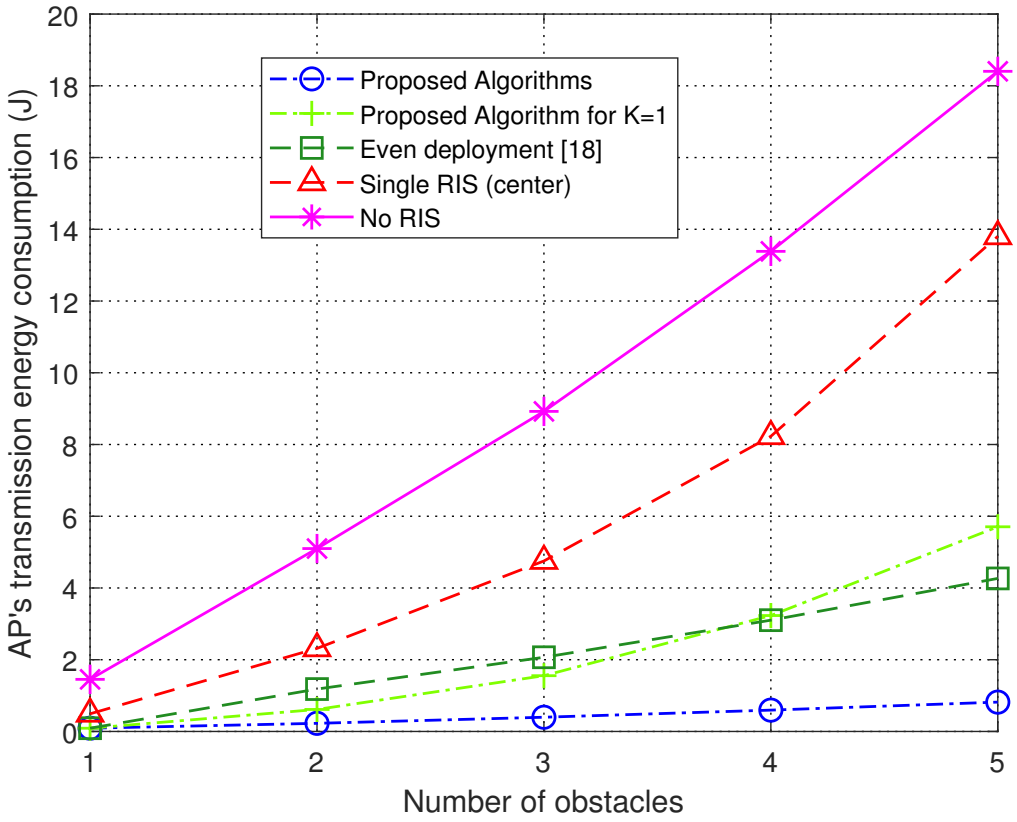

Figure IV.7: AP's transmission energy consumption versus the number of obstacles.

received SNR at the robot above a threshold throughout its journey, we have proposed the TECO Algorithm and RISLN Algorithm that jointly optimize the number, locations and phase shifts of RISs and the beamforming vector of the AP. Simulation results demonstrate that the proposed algorithms converge fast and can significantly reduce the transmission energy consumption at the AP as compared to the benchmark schemes that either do not deploy any RIS or do not optimize the number or locations of RISs. Distributing the fixed total number of reflecting elements to more RISs leads to a lower transmission energy consumption of the AP, since more distributed RISs provide more LoS links to the robot while it moves along its trajectory. The reduction in AP transmission energy consumption stops when the number of RISs becomes too large. This is because when all sections of the robot trajectory have been covered by LoS links from either the AP or an RIS, further dividing the fixed total number of reflecting elements into more RISs will reduce the beamforming gain of each RIS. For the considered scenario of I obstacles, properly deploying I RISs is sufficient to ensure that the robot sees a LoS link from at least one RIS or the AP at all times along its trajectory. The AP's transmission energy consumption increases with the minimum SNR required at the robot and the carrier frequency of the mmWave signal, but decreases with a larger total number of elements on the RISs.

In our future work, we will study the AP transmission energy consumption minimization problem where the robot's trajectory can be jointly optimized with the deployment of the AP and RISs. We will also extend out work to more complex scenarios, e.g., multiple robots moving along different trajectories. This will require allocating the available RISs and AP beamforming vectors to different robots while considering potential co-channel interference among the links serving neighboring robots. It will also be interesting to consider the energy consumption of RISs when the reflecting elements are not fully passive.

Bibliography

[1] S. Haddadin, A. De Luca and A. Albu-Schäffer, "Robot collisions: A survey on detection, isolation, and identification," in IEEE Transactions on Robotics, vol. 33, no. 6, pp. 1292-1312, Dec. 2017.

[2] T. S. Rappaport, G. R. MacCartney, M. K. Samimi and S. Sun, "Wideband millimeter-wave propagation measurements and channel models for future wireless communication system design," in IEEE Transactions on Communications, vol. 63, no. 9, pp. 3029-3056, Sept. 2015.

[3] A. N. Uwaechia and N. M. Mahyuddin, "A comprehensive survey on millimeter wave communications for fifth-generation wireless networks: Feasibility and challenges," in IEEE Access, vol. 8, pp. 62367-62414, 2020.

[4] M. Di Renzo, M. Debbah, D.-T. Phan-Huy, A. Zappone, M.-S. Alouini, C. Yuen, et al., "Smart radio environments empowered by reconfigurable AI meta-surfaces: An idea whose time has come", EURASIP J. Wireless Commun. Netw., vol. 2019, pp. 129, May 2019.

[5] Q. Wu and R. Zhang, "Towards smart and reconfigurable environment: Intelligent reflecting surface aided wireless network," in IEEE Communications Magazine, vol. 58, no. 1, pp. 106-112, January 2020.

[6] Q. Wu and R. Zhang, "Intelligent reflecting surface enhanced wireless network via joint active and passive beamforming," in IEEE Transactions on Wireless Communications, vol. 18, no. 11, pp. 5394-5409, Nov. 2019.

[7] H. Du, J. Zhang, J. Cheng, and B. Ai, "Millimeter wave communications with reconfigurable intelligent surfaces: Performance analysis and optimization," IEEE Trans. Commun., vol. 69, no. 4, pp. 2752–2768, Apr. 2021.

[8] S. Lin, B. Zheng, G. C. Alexandropoulos, M. Wen, M. D. Renzo and F. Chen, "Reconfigurable intelligent surfaces with reflection pattern modulation: Beamforming design and performance analysis," in IEEE Transactions on Wireless Communications, vol. 20, no. 2, pp. 741-754, Feb. 2021.

[9] J. Lyu and R. Zhang, "Spatial throughput characterization for intelligent reflecting surface aided multiuser system," in IEEE Wireless Communications Letters, vol. 9, no. 6, pp. 834-838, June 2020.

[10] S. Zhang and R. Zhang, "Intelligent reflecting surface aided multiple access: Capacity region and deployment strategy," 2020 IEEE 21st International Workshop on Signal Processing Advances in Wireless Communications (SPAWC), Atlanta, GA, USA, 2020, pp. 1-5.

[11] Y. Han, S. Zhang, L. Duan and R. Zhang, "Cooperative double-IRS aided communication: Beamforming design and power scaling," in IEEE Wireless Communications Letters, vol. 9, no. 8, pp. 1206-1210, Aug. 2020.

[12] Y. Zhang, J. Zhang, M. Di Renzo, H. Xiao and B. Ai, "Reconfigurable intelligent surfaces with outdated channel state information: Centralized vs. distributed deployments," in IEEE Transactions on Communications, vol. 70, no. 4, pp. 2742-2756, Apr. 2022.

[13] S. Pala, K. Singh, M. Katwe and C. -P. Li, "Joint optimization of URLLC parameters and beamforming design for multi-RIS-aided MU-MISO URLLC system," in IEEE Wireless Communications Letters, vol. 12, no. 1, pp. 148-152, Jan. 2023.

[14] K. Zhao, H. Mei, S. Lyu and L. Peng, "Joint optimization of multiple UAV-mounted RISs deployment and RIS elements allocation," 2022 13th International Conference on Information and Communication Technology Convergence (ICTC), Jeju Island, Korea, Republic of, 2022, pp. 1193-1197.

[15] C. Tatino, N. Pappas and D. Yuan, "Robot trajectory planning with QoS constrained IRS-assisted millimeter-wave communications," IEEE International Conference on Communications, 2021, pp. 1-6.

[16] M. Eskandari, H. Huang, A. V. Savkin and W. Ni, "Model predictive control-based 3D navigation of a RIS-equipped UAV for LoS wireless communication with a ground intelligent vehicle," in IEEE Transactions on Intelligent Vehicles, 2022.

[17] N. Agrawal, A. Bansal, K. Singh and C. -P. Li, "Performance evaluation of RIS-assisted UAV-enabled vehicular communication system with multiple non-identical interferers," in IEEE Transactions on Intelligent Transportation Systems, vol. 23, no. 7, pp. 9883-9894, July 2022.

[18] Y. Yu, X. Liu and V. C. M. Leung, "Fair downlink communications for RIS-UAV enabled mobile vehicles," in IEEE Wireless Communications Letters, vol. 11, no. 5, pp. 1042-1046, May 2022.

[19] A. Bansal, N. Agrawal, and K. Singh, "Rate-splitting multiple access for UAV-based RIS-enabled interference-limited vehicular communication system," IEEE Trans. Intel. Veh., 2022.

[20] E. Martin, M. Marcus, G. Thorsten and M. Stefan,"Fast ray/axis-aligned bounding box overlap tests using ray slopes," Journal of Graphics Tools, vol. 12, no. 4, pp. 35-46, 2007.

[21] J. He, H. Wymeersch, T. Sanguanpuak, O. Silven and M. Juntti,"Adaptive beamforming design for mmWave RIS-aided joint localization and communication," 2020 IEEE Wireless Communications and Networking Conference Workshops (WCNCW), 2020, pp. 1-6.

[22] T. K. Y. Lo, "Maximum ratio transmission," in IEEE Transactions on Communications, vol. 47, no. 10, pp. 1458-1461, Oct. 1999.

[23] R. L. Haupt and D. H. Werner,"Appendix: MATLAB code," in Genetic Algorithms in Electromagnetics, IEEE, 2007, pp.269-275.

[24] Z. Li, H. Hu, J. Zhang and J. Zhang, "Coverage analysis of multiple transmissive RIS-aided outdoor-to-indoor mmWave networks," in IEEE Transactions on Broadcasting, vol. 68, no. 4, pp. 935-942, Dec. 2022.

[25] V. Dharmadhikari, N. Pusalkar and P. Ghare, "Path loss exponent estimation for wireless sensor node positioning: Practical approach," 2018 IEEE International Conference on Advanced Networks and Telecommunications Systems (ANTS), 2018, pp. 1-4.

Chapter V

Paper II: Deployment Strategy of Intelligent Omni-surface-assisted Outdoor-to-Indoor Millimeter-wave Communications

Introduction & Comments

In this paper, I studied IOS-assisted outdoor-to-indoor mmWave communications where an outdoor BS transmit signals through multiple IOSs to indoor users. To address the BS's energy efficiency maximization problem, I propose EEM and IOSLN algorithms to jointly optimize the number, locations, phase shifts of the IOS and the beamforming vector of the BS. Simulation results find out that distributing IOSs across a wall rather than centralizing them significantly enhances BS energy efficiency, and the optimal IOS locations concentrate in the vertical central area of the wall.

Here are some further explanations to avoid confusion. This paper does not consider other multi-access techniques. Therefore, interference arises exclusively from the refracted signals of the IOS. Specifically, user k receives the desired signal corresponding to the beamforming vector w_k, while also experiencing interference from unintended signals directed at other users, which are associated with the beamforming vectors $w_1, w2, \cdots, w_j, \cdots, w_K$, where $j \neq k$.

Note that the parameters in Table I with the highest sensitivity to the overall results are the number of IOS elements IN, transmit power $P_{\mathrm{T}_{\max}}$, circuit power consumption P_{TR}, P_{BS}, and minimum data rate requirement $r_{\min}$. The number of IOS elements directly affects the beamforming gain and overall channel quality, making it critical for achieving high energy efficiency. Transmit power significantly influences the system's ability to overcome path loss and meet user rate requirements, particularly in scenarios with high blockage or long distances. Circuit power consumption contributes directly to the denominator of the energy efficiency metric, making it a dominant factor when transmit power is low. The minimum data rate requirement directly influences the optimization of beamforming and phase shift designs. It places constraints on how power is allocated and how the IOS is configured to maximize overall system efficiency

while ensuring no user experiences a data outage.

For mmWave frequencies like 60 GHz, IOS element sizes are typically small due to the shorter wavelengths $\lambda = \frac{c}{f} = \frac{3\times10^8}{60\times10^9} = 5mm$, where c and f are speed of light and carrier frequency. Based on this, each IOS element could be in the range of 0.5λ to λ, making the size of an individual IOS element around $2.5mm$ to $5mm$.

Deployment Strategy of Intelligent Omni-surface-assisted Outdoor-to-Indoor Millimeter-wave Communications

Zhiyu Liu*, David Lopez-Perez†, Na Tang, Xiaoli Chu

Abstract

Intelligent omni-surfaces (IOSs) have been considered for assisting outdoor-to-indoor millimeter-wave (mmWave) communications. Nevertheless, the existing works have not adequately investigated how the number or the deployment locations of IOSs should be optimized for serving multiple indoor users. In this paper, we study IOS-assisted outdoor-to-indoor mmWave communications where IOSs are installed in an exterior wall of a building to refract mmWave signals from an outdoor base station (BS) to indoor users that locate among indoor blockages. Given a fixed total number of refracting elements, we formulate an optimization problem to maximize the downlink energy efficiency of the outdoor BS while satisfying the dowlink data rate requirements of the indoor users by jointly optimizing the number, locations and phase shifts of IOSs and the beamforming vectors of the BS. To address the varying dimensionality and

*Zhiyu Liu, Na Tang, and Xiaoli Chu are with the Department of Electronic and Electrical Engineering, The University of Sheffield, Sheffield S1 4ET, UK

†David Lopez-Perez is with the Institute of Telecommunications and Media Applications, Universitat Politècnica de València, 46022 Valencia, Spain

the non-convexity of the optimization problem, we decompose it into two sub-problems that optimize the IOSs' phase shifts together with the BS beamforming vectors and the number and locations of IOSs, respectively, and devise successive convex approximation and Continuous Population-Based Incremental Learning-based algorithms to solve them alternately. Simulation results demonstrate that the proposed algorithms can obtain the optimal number and locations of IOSs, resulting in significantly enhanced energy efficiency of the outdoor BS compared to benchmark schemes.

V.1 Introduction

Nowadays, with over 80% of mobile data traffic generated or terminated indoors [15], the deployment of indoor small-cell base stations (BSs) for wireless coverage faces challenges. Managing large numbers of indoor BSs and their associated wired or optical backhaul involves high costs and complexity [2]. Moreover, their performance is hindered by inter-cell interference, especially in dense deployment scenarios [3].

To address these issues, outdoor-to-indoor communication utilizing existing outdoor BSs to serve indoor users is gaining prominence as a promising alternative solution to meet indoor mobile service demand [4, 5]. Simultaneously, the rise of millimeter-wave (mmWave) communications is anticipated to play a crucial role in 5G and future 6G mobile networks [6].

Recent studies on outdoor-to-indoor mmWave communications mainly aimed to mitigate severe penetration losses and attenuations experienced by mmWave signals propagating through walls, windows, or other building materials [2, 7–9]. It was shown in [10] that a relay-aided outdoor-to-indoor mmWave downlink system achieved a higher indoor coverage probability than systems without relays.

In [2], outdoor-to-indoor penetration losses were addressed by deploying customer

premise equipment (CPE), comprising a pair of connected outdoor and indoor units. The outdoor unit, installed on an exterior window or wall, receives mmWave signals from an outdoor BS, while the indoor unit down-converts and transmits them to indoor users. However, the deployment and maintenance of CPE, involving signal frequency conversion and active components, can be costly and power-consuming [2].

In [11], the authors focused on maximizing the downlink received signal-to-noise ratio (SNR) by jointly optimizing the active and passive beamforming of both an outdoor and an indoor hybrid reconfigurable intelligent surface (RIS). These RISs sequentially reflect an outdoor mmWave signal to an indoor receiver. We note that the study in [11] did not consider penetration losses through building materials and the reflections by two RISs will result in severe attenuation of the signal strength.

Different from RISs, intelligent omni-surfaces (IOSs) that can refract and/or reflect incident signals by changing their phase and amplitude have recently emerged [12–14]. An IOS is typically a planar array of nearly passive reconfigurable elements. Recent works explored the idea of installing IOSs on the exterior walls of buildings to refract signals from an outdoor BS to indoor users [12], [14]. The authors in [15] designed new IOS elements and arranged them in a hexagonal lattice structure. Simulation results showed that substituting a part of a wall with an IOS can improve the coverage probability for the outdoor-to-indoor mmWave communication system. In [16], simulation results demonstrated that replacing a part of a concrete wall with a refracting RIS that refracts the mmWave signals from an outdoor BS to indoor users can significantly increase the coverage probability as compared with a relay-aided counterpart. The authors in [17] maximized the downlink data rate in an IOS-assisted outdoor-to-indoor mmWave cellular network by jointly optimizing the precoding matrices of both the BS and the IOS. In [18], analytical results showed that, for a fixed total number of reconfigurable elements, distributing them to multiple small IOSs evenly spaced at the

same height on a selected wall resulted in a higher indoor coverage probability than deploying one large IOS on the same wall. This performance gap became more evident for a higher indoor blockage density and/or a lower SNR threshold. We note that, [16] and [17] limited their focus to a single IOS, and neither [16] nor [18] considered multi-user interference. Additionally, the optimization of both the quantity and placements of IOSs was overlooked in these studies.

In this paper, we study an outdoor-to-indoor mmWave communication system, where an outdoor BS transmits mmWave signals to indoor users through multiple IOSs deployed on the exterior wall between the BS and the users[1], taking into account the impact of indoor blockages. Our goal is to maximize the transmission energy efficiency of the outdoor BS by investigating whether a fixed number of passive elements should be distributed across a large number of small IOSs or centralized in a small number of large IOSs, while maintaining reliable downlink communications for all indoor users.

The contributions of this paper can be summarized as follows:

- We formulate an optimization problem to maximize the transmission energy efficiency of the outdoor BS while ensuring that the downlink data rate of each user remains above a threshold. This optimization problem involves a joint optimization of the number, positions, and phase shifts of the IOSs, as well as the beamforming vectors of the BS. The challenges in solving this problem primarily arise from the intricate coupling of variables, the non-convexity, and the varying dimensionality of the problem. This is distinct from the existing works that considered only a single IOS [12, 13, 15–17], or where the number or locations of IOSs were not optimized [12, 13, 15–18].

- We address the varying dimensionality of the joint optimization problem by de-

[1]Since the IOSs in our system model are mainly used to refract the outdoor BS's signals to indoor users, they can also be referred to as reconfigurable refractive surfaces [**?**].

composing it into two subproblems. The first subproblem involves optimizing the phase shifts of the IOSs and the beamforming vectors of the BS for a given number and locations of IOSs. For this non-convex subproblem, we devise an Energy Efficiency Maximization (EEM) algorithm to solve it by iteratively optimizing the phase shifts of each IOS and the beamforming vector of the BS. The second subproblem involves optimizing the number and locations of IOSs for a given set of phase shifts and beamforming vectors, and is solved by leveraging the Continuous Population-Based Incremental Learning (PBILc) algorithm. By solving the above two subproblems alternately, we propose the IOS Locations and Number (IOSLN) Algorithm to iteratively determine the optimal quantity, placement, and phase shifts of the IOSs, alongside the beamforming vectors for the BS. It achieves this through a repeated process that alternates between the PBILc algorithm and the proposed EEM algorithm. This iterative approach ensures that the adjustments to the number and locations of IOSs directly influence their phase shifts and the BS's beamforming strategy, enabling a harmonized optimization of all the variables toward a maximized transmission energy efficiency of the outdoor BS.

- Our simulation results demonstrate that the proposed algorithms can identify suitable numbers and deployment locations of IOSs that maximize the energy efficiency of the outdoor BS, while maintaining reliable downlink communications for all indoor users. The results also indicate that, for a fixed total number of reconfigurable elements, the optimized number and locations of IOSs lead to higher energy efficiency of the BS compared to either centralized or evenly distributed IOS deployment. The optimal number of IOSs increases with the number of indoor users, and the optimized IOS locations cluster in a vertical central area of the wall.

The rest of the paper is organized as follow. In Section II, we introduce the system model and the channel model. In Section III, we formulate the BS's downlink transmission energy efficiency maximization problem and propose algorithms to solve it. Section IV presents simulation results. Finally, we conclude the paper in Section V.

V.2 System Model

As shown in Fig. 1, we consider an outdoor-to-indoor mmWave communication system, where an outdoor BS transmits signals to K indoor users through I IOSs deployed on the wall between the BS and the users. The BS is equipped with a uniform linear array (ULA) of $M(>1)$ antennas.

The K users are distributed on the floor of a room, which has a length of L_{r}, width of W_{r}, and height of H_{r} along the x-axis, y-axis and z-axis in Fig. 1, respectively. Each user is equipped with a single directional antenna. The locations of the users are denoted by $\boldsymbol{q}_{\mathrm{UE}} = [q_1, \cdots, q_K]$, where $q_k = (x_k, y_k, z_k)$ is the location of the k-th user, x_k and y_k follow a distribution $\boldsymbol{\Xi}$ on the 2D horizontal plane, e.g., a uniform distribution, and z_k is the k-th user's height that follows an independent uniform distribution from 1m to 2m. In the room, there are R static blockages that are distributed on the floor following a 2D homogeneous Poisson point process (PPP) with a density of κ blockage/m^2 [20]. We assume that the blockages are cubes with lengths $\boldsymbol{L}_o = [L_{o_1}, \cdots, L_{o_R}]$, widths $\boldsymbol{W}_o = [W_{o_1}, \cdots, W_{o_R}]$, and heights $\boldsymbol{H}_o = [H_{o_1}, \cdots, H_{o_R}]$, where the elements of $\boldsymbol{L}_o$ and $\boldsymbol{W}_o$ follow independent uniform distributions from 1m to 2m, and those of $\boldsymbol{H}_o$ in the range $[1.5\mathrm{m}, H_{\mathrm{r}}]$. Each IOS contains N elements that form an uniform rectangular array (URA). The locations of the IOSs are denoted by $\boldsymbol{q}_{\mathrm{IOS}} = [\boldsymbol{q}_1, \cdots, \boldsymbol{q}_I]$, where $q_i = [q_{i1}, \cdots, q_{iN}]$ contains the locations of the N elements on

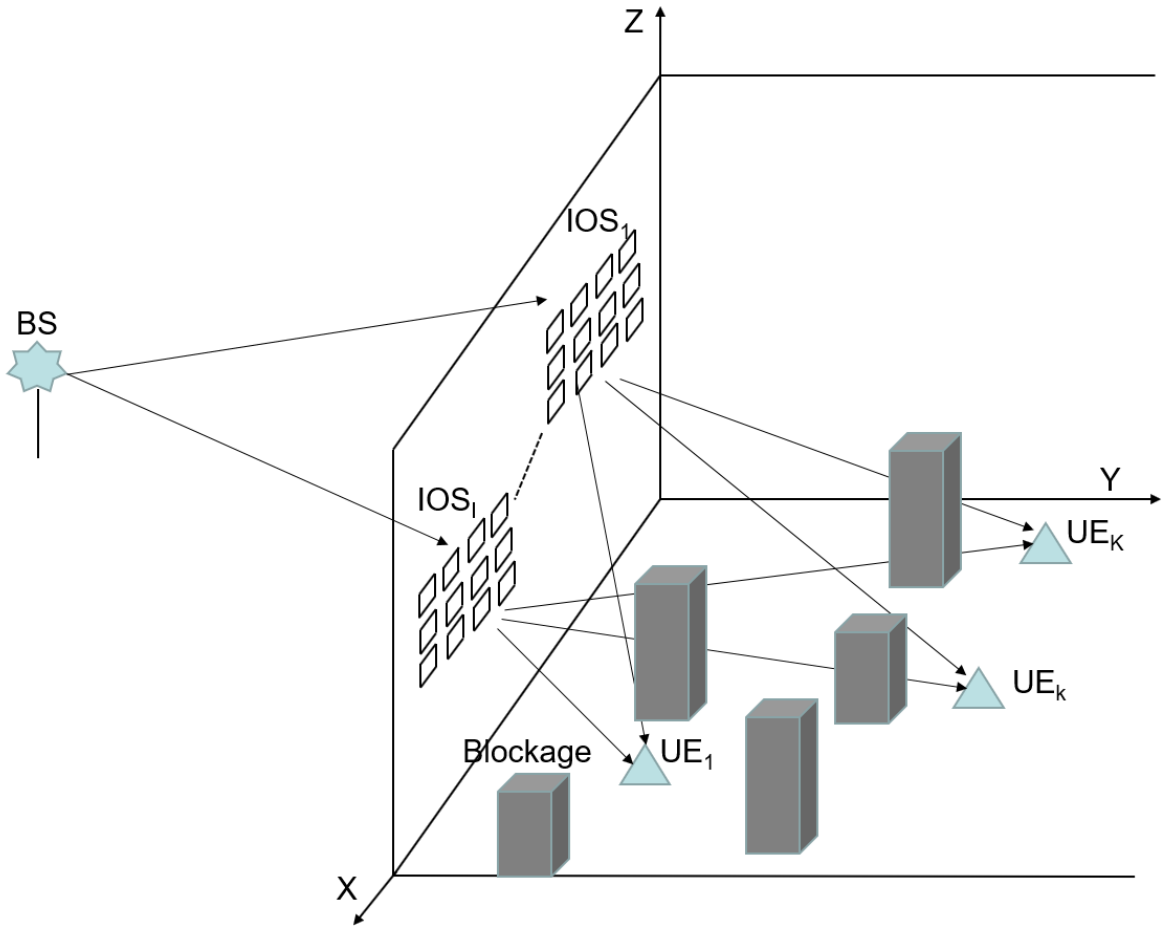

Figure V.1: An IOS-assisted outdoor-to-indoor mmWave communication system.

the i-th IOS, $q_{in} = (x_{in}, y_{in}, z_{in})$. For simplicity in optimizing the locations of the IOSs, the location of the central element of an IOS's array is used to present the location of the IOS, which is denoted by $q_{\mathrm{c}_i} = (x_{\mathrm{c}_i}, y_{\mathrm{c}_i}, z_{\mathrm{c}_i})$ for the i-th IOS, $i \in \{1, \cdots, I\}$, with $\boldsymbol{q}_{\mathrm{IOS_c}} = [q_{\mathrm{c}_1}, \cdots, q_{\mathrm{c}_I}]$. Each IOS is connected to a smart controller that adjusts its phase shifts and refraction amplitudes via a separate wired link.

V.2.1 Channel Model

The channel from the BS to the i-th IOS is modeled as a Rician channel, and is denoted by $\boldsymbol{G}_i \in \mathbb{C}^{N \times M}$. The (n, m)-th element in $\boldsymbol{G}_i$ denotes the channel between the m-th antenna at the BS and the n-th element on the i-th IOS, and is given by [19]

$$G_{i,mn} = \sqrt{\frac{\epsilon}{1+\epsilon}} G_{i,mn}^{LoS} + \sqrt{\frac{1}{1+\epsilon}} G_{i,mn}^{NLoS} \tag{V.1}$$

where ϵ is the Rician factor, $G_{i,mn}^{LoS}$ and $G_{i,mn}^{NLoS}$ are the LoS and NLoS component, respectively, and $G_{i,mn}^{LoS}$ is given by [19]

$$G_{i,mn}^{LoS} = \frac{\sqrt{J_m^{BS} J_{i,n}^{IOS} K_{i,mn}^{A} K_{i,mn}^{D}} e^{\left(\frac{-j2\pi d_{i,mn}}{\lambda}\right)}}{(4\pi)^{\frac{3}{4}} (d_{i,mn})^{\alpha}} \tag{V.2}$$

where J_m^{BS} and $J_{i,n}^{IOS}$ are the maximum antenna gain of the m-th antenna element at the BS and the maximum antenna gain of the n-th element on the i-th IOS, respectively, $d_{i,mn} = \sqrt{(x_m - x_{in})^2 + (y_m - y_{in})^2 + (z_m - z_{in})^2}$ is the distance between the m-th antenna at the BS and the n-th element on the i-th IOS, λ is the signal wavelength, α is the path loss exponent, $K_{i,mn}^{D}$ and $K_{i,mn}^{A}$ are the normalized radiation pattern of the m-th antenna element at the BS in the direction of the n-th element on the i-th IOS and the normalized radiation pattern of the n-th element on the i-th IOS in the

direction of the m-th antenna at the BS, and are given by

$$K_{i,mn}^{D} = \left|\cos^3 \phi_{i,mn}^{D}\right|, \tag{V.3}$$

$$K_{i,mn}^{A} = \left|\cos^3 \phi_{i,mn}^{A}\right| \tag{V.4}$$

where $\phi_{i,mn}^{D}$ and $\phi_{i,mn}^{A}$ are the angle of departure (AoD) from the m-th antenna at the BS to the n-th element on the i-th IOS and the angle of arrival (AoA) at the n-th element on the i-th IOS from the m-th antenna at the BS, respectively.

The NLoS component in (V.1) is given by

$$G_{i,mn}^{NLoS} = \tilde{h}_{i,mn}, \tag{V.5}$$

where $\tilde{h}_{i,mn} \sim \mathcal{CN}(0,1)$ follows independent complex Gaussian distribution with zero mean and unit variance.

The channel from the i-th IOS to the k-th user is given by

$$\hat{\boldsymbol{h}}_{ik} = \boldsymbol{b}_{ik} \odot \boldsymbol{h}_{ik}, \tag{V.6}$$

where $\odot$ denotes the element-wise multiplication, $\boldsymbol{b}_{ik} = [b_{ik,1}, \cdots, b_{ik,N}]$ contains N binary indicators, where $b_{ik,n} = 1$ indicates that the link between the n-th element of the i-th IOS and the k-th user is LoS [16], otherwise $b_{ik,n} = 0$, and $\boldsymbol{h}_{ik} = [h_{ik,1}, \cdots, h_{ik,N}]$, where $h_{ik,n}$ is the channel coefficient between the n-th element on the i-th IOS and the k-th user, and is given by [19]

$$h_{ik,n} = \sqrt{\frac{\epsilon}{1+\epsilon}} h_{ik,n}^{LoS} + \sqrt{\frac{1}{1+\epsilon}} h_{ik,n}^{NLoS}, \tag{V.7}$$

where $h_{ik,n}^{LoS}$ is the LoS component and is given by

$$h_{ik,n}^{LoS} = \frac{\lambda\sqrt{J_{i,n}^{IOS} J_k K_{ik,n}^D K_{ik,n}^A \delta_x \delta_z \gamma_{n,i}} e^{\left(\frac{-j2\pi d_{ik,n}}{\lambda}\right)}}{(4\pi)^{\frac{3}{4}} (d_{ik,n})^{\alpha}}, \tag{V.8}$$

where J_k is the maximum antenna gain of the k-th user, δ_x and δ_z are the sizes of each element on the respective IOSs, $\gamma_{n,i}$ is the power ratio between the signal re-emitted by the n-th element of the i-th IOS and the incident signal, $d_{ik,n}$ the distance between the n-th element on the i-th IOS and the k-th user and is given by

$$d_{ik,n} = \sqrt{(x_{in} - x_k)^2 + (y_{in} - y_k)^2 + (z_{in} - z_k)^2}. \tag{V.9}$$

$K_{ik,n}^D$ and $K_{ik,n}^A$ are the normalized radiation pattern of the n-th element on the i-th IOS in the direction of the k-th user and the normalized radiation pattern of the k-th user's antenna, and are given by

$$K_{ik,n}^D = \left|\cos^3 \phi_{ik,n}^D\right| \tag{V.10}$$

$$K_{ik,n}^A = \left|\cos^3 \phi_{ik,n}^A\right|, \tag{V.11}$$

where $\phi_{ik,n}^D$ and $\phi_{ik,n}^A$ are the AoD from the n-th element on the i-th IOS to the k-th user and the AoA at the k-th user from the n-th element on the i-th IOS, respectively.

The NLoS component in (V.7) is given by

$$h_{ik,n}^{NLoS} = \tilde{h}_{ik,n}, \tag{V.12}$$

where $\tilde{h}_{ik,n} \sim \mathcal{CN}(0,1)$.

The LoS probability of the link between the n-th element on the i-th IOS and the

k-th user is given by [16]

$$P_{ik,n} = \Pr\left[b_{ik,n} = 1\right] = \Gamma(z_{in}) e^{-\left(\beta \hat{d}_{ik,n} + p\right)}, \tag{V.13}$$

where $\Gamma(z_{i,n})$ is given by

$$\Gamma(z_{i,n}) = \frac{1}{2} \times \left(1 + \frac{z_{i,n} - \mathrm{E}\left[\boldsymbol{H}_o\right]}{H_{\mathrm{r}}}\right), \tag{V.14}$$

where $\mathrm{E}\left[\boldsymbol{H}_o\right]$ is the average height of the blockages, $\hat{d}_{ik,n} = \sqrt{(x_{in} - x_k)^2 + (y_{in} - y_k)^2}$ is the horizontal distance between the n-th element on the i-th IOS and the k-th user, and β is given by

$$\beta = \frac{2\kappa \left(\mathrm{E}\left[\boldsymbol{L}_o\right] + \mathrm{E}\left[\boldsymbol{W}_o\right]\right)}{\pi}, \tag{V.15}$$

where κblokages/m^2 is the density of blockages, $\mathrm{E}\left[\boldsymbol{L}_o\right]$ and $\mathrm{E}\left[\boldsymbol{W}_o\right]$ are the average length and width of the blockages, respectively, p in (V.13) is the fraction of the room's floor area covered by blockages and is given by

$$p = \kappa \mathrm{E}\left[\boldsymbol{L}_o\right] \mathrm{E}\left[\boldsymbol{W}_o\right]. \tag{V.16}$$

V.2.2 Downlink data rate

The signal received at the k-th user is given by

$$y_k = \left(\sum_{i=1}^{I} \hat{\boldsymbol{h}}_{ik} \boldsymbol{\Theta}_i \boldsymbol{G}_i\right) \boldsymbol{w}_k s_k + \iota_k \tag{V.17}$$

where $k = 1, \cdots, K$, $\boldsymbol{\Theta}_i = \mathrm{diag}\left(e^{j\theta_{i1}}, \cdots, e^{j\theta_{iN}}\right)$ is a N-by-N diagonal matrix, θ_{in} is the refraction phase shift applied by the n-th element on the i-th IOS, s_k is the information symbol with a zero mean and unit variance (i.e., normalized power) transmitted by the

BS to the k-th user, $\boldsymbol{w}_k \in \mathbb{C}^{M\times 1}$ is the BS beamforming vector towards the k-th user, and $\sum_{k=1}^{K} {\boldsymbol{w}_k}^H \boldsymbol{w}_k = P_T$, where P_T is the transmit power at the BS, and ι_k is the additive white Gaussian noise (AWGN) at the k-th user with zero mean and the variance of σ^2. For analytical tractability, we assume that the IOSs' phase shifts are continuous. The results of this work can be applied to a system where the IOS phase shifts are of discrete values by adding a quantization process, which approximates the optimal continuous phase shifts of the IOS by the closest possible discrete phase shift values.

The downlink data rate at the k-th user is given by

$$r_k = B\log_2\left(1 + \frac{\left|\left(\sum_{i=1}^{I} \hat{\boldsymbol{h}}_{ik}\boldsymbol{\Theta}_i\boldsymbol{G}_i\right)\boldsymbol{w}_k\right|^2}{\sum_{j=1,j\neq k}^{K}\left|\left(\sum_{i=1}^{I} \hat{\boldsymbol{h}}_{ik}\boldsymbol{\Theta}_i\boldsymbol{G}_i\right)\boldsymbol{w}_j\right|^2 + \sigma^2}\right), \tag{V.18}$$

where B is the bandwidth of the BS transmission to a single user.

Letting $\hat{\boldsymbol{h}}_k = \left[\hat{\boldsymbol{h}}_{1k}, \cdots, \hat{\boldsymbol{h}}_{Ik}\right]$, $\boldsymbol{G} = [\boldsymbol{G}_1, \cdots, \boldsymbol{G}_I]^H$, and $\boldsymbol{\Lambda} = [\boldsymbol{\Lambda}_1, \cdots, \boldsymbol{\Lambda}_I]^H \in \mathbb{C}^{IN\times 1}$, where $\boldsymbol{\Lambda}_i = \left[e^{j\theta_{i1}}, \cdots, e^{j\theta_{iN}}\right]^H \in \mathbb{C}^{N\times 1}, \Lambda_{in} = e^{j\theta_{in}}$,$\hat{\boldsymbol{\Theta}} = \text{diag}(\Lambda) \in \mathbb{C}^{IN\times IN}$, the expression of r_k is rewritten as

$$r_k = B\log_2\left(1 + \frac{\left|\left(\hat{\boldsymbol{h}}_k\hat{\boldsymbol{\Theta}}\boldsymbol{G}\right)\boldsymbol{w}_k\right|^2}{\sum_{j=1,j\neq k}^{K}\left|\left(\hat{\boldsymbol{h}}_k\hat{\boldsymbol{\Theta}}\boldsymbol{G}\right)\boldsymbol{w}_j\right|^2 + \sigma^2}\right). \tag{V.19}$$

V.3 Problem Formulation and Solution Algorithms

V.3.1 Problem Formulation

We formulate an optimization problem to maximize the downlink transmission energy efficiency of the BS by jointly optimizing the number and locations of IOSs, the re-

fraction phase shifts of all the IOS elements, and the beamforming vectors of the BS, subject to the constraints on the downlink data rate of each user and the maximum transmission power of the BS, i.e.,

$$(P1): \max_{I,\boldsymbol{q}_{\mathrm{IOS_c}},\hat{\boldsymbol{\Theta}},\boldsymbol{w}_1,\cdots,\boldsymbol{w}_K} \frac{\sum_{k=1}^{K} r_k}{\sum_{k=1}^{K} \boldsymbol{w}_k{}^H \boldsymbol{w}_k + P_C} \tag{V.20}$$

$$s.t.\ C1: \sum\nolimits_{k=1}^{K} \boldsymbol{w}_k{}^H \boldsymbol{w}_k \leqslant P_{T\max}, \tag{V.20a}$$

$$C2: 0 \leqslant \theta_{in} < 2\pi, \forall i, \forall n, \tag{V.20b}$$

$$C3: r_k \geqslant r_{\min,k}, \forall k, \tag{V.20c}$$

$$C4: I \geqslant 1, \tag{V.20d}$$

$$C5: \frac{d_I}{2} \leqslant x_{\mathrm{c}_i} \leqslant L_{\mathrm{r}} - \frac{d_I}{2}, \forall i, \tag{V.20e}$$

$$C6: E[\boldsymbol{H}_o] + \frac{d_I}{2} \leqslant z_{\mathrm{c}_i} \leqslant H_{\mathrm{r}} - \frac{d_I}{2}, \forall i, \tag{V.20f}$$

$$C7: \left|z_{\mathrm{c}_i} - z_{\mathrm{c}_j}\right| \geqslant d_I, \text{or } \left|x_{\mathrm{c}_i} - x_{\mathrm{c}_j}\right| \geqslant d_I, i \neq j, \forall i, \forall j, \tag{V.20g}$$

where I is the number of IOSs and $\boldsymbol{q}_{\mathrm{IOS}_c}$ contains the locations of the IOSs, $P_{T\max}$ is the maximum transmit power of the BS, $r_{\min,k}$ is the minimum downlink data rate required of the k-th user, d_I is the size of an IOS, and the minimum distance we set between two IOSs to avoid overlapping, P_C denotes the total power consumed by the active transceivers at the BS and by the circuits of the BS and the users, and it is given by [22]

$$P_C = P_{BS} + N_{TR}P_{TR} + \sum\nolimits_{k=1}^{K} P_k, \tag{V.21}$$

where P_{BS} is the circuit power consumed by the BS, N_{TR} is the number of active transceivers at the BS, P_{TR} is the power consumed by each active transceiver at the BS, and P_k is the circuit power consumed by the k-th user. In $(P1)$, constraint C1

specifies the maximum transmit power at the outdoor BS, C2 imposes the value range of the phase shift for each element on the IOSs, C3 ensures that the downlink data rate at each user is above the minimum downlink data rate required, C4 guarantees that at least one IOS is deployed, C5 and C6 delineate the permissible spatial boundaries for the placement of IOSs, and C7 precludes the overlap of these IOSs, ensuring their distinct and non-intersecting distribution.

V.3.2 EEM Algorithm

We note that it is hard to solve $(P1)$ directly due to the varying number of variables involved and its non-convexity. Hence, we first study the case with the number I and the locations of IOSs fixed, for which $(P1)$ reduces to

$$(P2): \max_{\hat{\boldsymbol{\Theta}}, \boldsymbol{w}_1, \cdots, \boldsymbol{w}_K} \frac{\sum_{k=1}^{K} r_k}{\sum_{k=1}^{K} {\boldsymbol{w}_k}^H \boldsymbol{w}_k + P_C} \quad s.t.\ C1, C2, C3. \tag{V.22}$$

Since $(P2)$ is still a non-convex problem and is difficult to solve directly, we decompose $(P2)$ into two subproblems that optimize the IOSs' refraction phase shifts for given beamforming vectors of the BS and the BS's beamforming vectors for given refraction phase shifts of the IOSs, respectively.

Refraction phase shifts

For given beamforming vector $\boldsymbol{w}_k, k = 1, \cdots, K$, (P2) reduces to

$$(P3): \max_{\hat{\boldsymbol{\Theta}}, \boldsymbol{\eta}} \sum_{k=1}^{K} \log_2 (1 + \eta_k) \tag{V.23}$$

$$
\begin{aligned}
s.t. \qquad & C2 \\
& C8: \eta_k \leqslant \frac{\left|\left(\hat{\boldsymbol{h}}_k \hat{\boldsymbol{\Theta}} \boldsymbol{G}\right) \boldsymbol{w}_k\right|^2}{\sum_{j=1, j \neq k}^{K}\left|\left(\hat{\boldsymbol{h}}_k \hat{\boldsymbol{\Theta}} \boldsymbol{G}\right) \boldsymbol{w}_j\right|^2+\sigma^2}, \qquad \text{(V.23a)} \\
& \qquad\qquad \forall k \in\{1, \cdots, K\}, \\
& C9: \eta_k \geqslant 2^{\frac{r_{\min, k}}{B}}-1, \ \forall k \in\{1, \cdots, K\}. \qquad \text{(V.23b)}
\end{aligned}
$$

where $\boldsymbol{\eta}=[\eta_1, \cdots, \eta_K] \in \mathbb{C}^{1 \times K}$ is a slack vector that returns the optimal solution when the equality in constraint $C8$ holds, and $C9$ ensures the minimum rate required of each user. Letting $\left(\hat{\boldsymbol{h}}_k \hat{\boldsymbol{\Theta}} \boldsymbol{G}\right) \boldsymbol{w}_j=\boldsymbol{\varsigma}_{kj}^H \boldsymbol{\Lambda}$, where $\boldsymbol{\varsigma}_{kj}=\operatorname{diag}\left(\hat{\boldsymbol{h}}_k\right) \boldsymbol{G} \boldsymbol{w}_j$, $C8$ can be rewritten as

$$
C8': \eta_k \leqslant \frac{\left|\boldsymbol{\varsigma}_{kk}^H \boldsymbol{\Lambda}\right|^2}{\sum_{j=1, j \neq k}^{K}\left|\boldsymbol{\varsigma}_{kj}^H \boldsymbol{\Lambda}\right|^2+\sigma^2}, \ \forall k \in\{1, \cdots, K\}. \qquad \text{(V.24)}
$$

To deal with the non-convexity of $C8'$, we introduce the auxiliary variables $\zeta_k, \ k=1, \cdots, K$, $\boldsymbol{\zeta}=[\zeta_1, \cdots, \zeta_K]$, and convert $C8'$ to $C8.1'$ and $C8.2'$ as follows

$$
C8.1': \ \left|\boldsymbol{\varsigma}_{kk}^H \boldsymbol{\Lambda}\right|^2 \geqslant \zeta_k \eta_k=\frac{1}{4}\left(\left(\zeta_k+\eta_k\right)^2-\left(\zeta_k-\eta_k\right)^2\right), \qquad \text{(V.25)}
$$

$$
C8.2': \ \sum\nolimits_{j=1, j \neq k}^{K}\left|\boldsymbol{\varsigma}_{kj}^H \boldsymbol{\Lambda}\right|^2+\sigma^2 \leqslant \zeta_k, \qquad \text{(V.26)}
$$

By substituting $C8.1'$ and $C8.2'$ into $(P3)$, we have

$$
(P4): \ \max_{\boldsymbol{\Lambda}, \boldsymbol{\eta}, \boldsymbol{\zeta}} \sum\nolimits_{k=1}^{K} \log_2\left(1+\eta_k\right) \qquad \text{(V.27)}
$$

$$s.t. \qquad C8.1', C8.2', C9$$

$$C2': \ |\Lambda_{in}| = 1, \ \forall i \in \{1, \cdots, I\}, \forall n \in \{1, \cdots, N\}. \tag{V.27a}$$

$$C10: \ \zeta_k \geqslant 0, \ \forall k \in \{1, \cdots, K\}. \tag{V.27b}$$

By applying the penalty method, $(P4)$ can be rewritten as

$$(P5): \ \max_{\mathbf{\Lambda}, \boldsymbol{\eta}, \boldsymbol{\zeta}} \sum\nolimits_{k=1}^{K} \log_2 (1 + \eta_k) + A \sum\nolimits_{i=1}^{I} \sum\nolimits_{n=1}^{N} \Big(|\Lambda_{in}|^2 - 1 \Big) \tag{V.28}$$

$$s.t. \qquad C8.1', C8.2', C9, C10,$$

$$C2'': \ |\Lambda_{in}| \leqslant 1, \ \forall i \in \{1, \cdots, I\}, \forall n \in \{1, \cdots, N\}. \tag{V.28a}$$

where A is a positive constant, and the optimal solution will be achieved when $|\Lambda_{in}| = 1$, $\forall i \in \{1, \cdots, I\}$, $\forall n \in \{1, \cdots, N\}$.

Then, we use successive convex approximation (SCA) to solve $(P5)$ iteratively as follows. In the s-th iteration, where $s \geqslant 1$, the objective function of $(P5)$ is approximated by

$$\begin{aligned} \max_{\mathbf{\Lambda}, \boldsymbol{\eta}, \boldsymbol{\zeta}} & \sum\nolimits_{k=1}^{K} \log_2 \left(1 + \eta_k^{(s)} \right) \\ & + 2A \sum\nolimits_{i=1}^{I} \sum\nolimits_{n=1}^{N} \Lambda_{in}^{(s-1)} \left(\Lambda_{in}^{(s)} - \Lambda_{in}^{(s-1)} \right) \end{aligned} \tag{V.29}$$

where $2A \sum_{i=1}^{I} \sum_{n=1}^{N} \Lambda_{in}^{(s-1)} \left(\Lambda_{in}^{(s)} - \Lambda_{in}^{(s-1)} \right)$ is the first order Taylor polynomial of $A \sum_{i=1}^{I} \sum_{n=1}^{N} \left(\left| \Lambda_{in}^{(s)} \right|^2 - 1 \right)$ at $\Lambda_{in}^{(s-1)}$, and $\Lambda_{in}^{(0)}$ is the initial value of Λ_{in}.

Although $C8.2'$ is convex, $C8.1'$ is still non-convex. Since $\left| \boldsymbol{\varsigma}_{kk}^H \mathbf{\Lambda} \right|^2$ and $(\zeta_k - \eta_k)^2$ are convex and any convex function is globally lower-bounded by its first order Taylor polynomial at any point [23], we approximate both sides of $C8.1'$ by their first order

Taylor polynomial at $\mathbf{\Lambda}^{(s-1)}$, $\zeta_k^{(s-1)}$, and $\eta_k^{(s-1)}$ and have

$$\begin{aligned} C8.1'':\ & 2\Re\left(\left(\boldsymbol{\varsigma}_{kk}^H\mathbf{\Lambda}^{(s-1)}\right)^H\boldsymbol{\varsigma}_{kk}^H\mathbf{\Lambda}^{(s)}\right)-\left|\boldsymbol{\varsigma}_{kk}^H\mathbf{\Lambda}^{(s-1)}\right|^2 \\ \geqslant & \frac{1}{4}\Bigg[\left(\zeta_k^{(s)}+\eta_k^{(s)}\right)^2-\left(\zeta_k^{(s-1)}-\eta_k^{(s-1)}\right) \\ & \left(\zeta_k^{(s)}-\eta_k^{(s)}\right)+\left(\zeta_k^{(s-1)}-\eta_k^{(s-1)}\right)^2\Bigg] \end{aligned} \tag{V.30}$$

Based on (V.29) and (V.30), $(P5)$ can be approximated to the following convex problem:

$$(P6):\ \max_{\mathbf{\Lambda}^{(s)},\boldsymbol{\eta}^{(s)},\boldsymbol{\zeta}^{(s)}}\sum\nolimits_{k=1}^{K}\log_2\left(1+\eta_k^{(s)}\right)+2A\sum\nolimits_{i=1}^{I}\sum\nolimits_{n=1}^{N}\Lambda_{in}^{(s-1)}\left(\Lambda_{in}^{(s)}-\Lambda_{in}^{(s-1)}\right) \tag{V.31}$$

$$s.t.\qquad C8.2', C8.1'', C9, C2'', C10.$$

Since $(P6)$ is a convex problem, it can be solved by CVX toolbox [26]. With the optimal $\mathbf{\Lambda}$ obtained by solving $(P6)$, we have the optimal $\hat{\mathbf{\Theta}}$.

Beamforming vector

Continuing from the previous subsection, with the $\hat{\mathbf{\Theta}}$ obtained by solving $(P6)$, $(P2)$ reduces to

$$(P7):\ \max_{\tilde{\boldsymbol{\eta}},\boldsymbol{w}_1,\cdots,\boldsymbol{w}_K}\frac{\sum_{k=1}^{K}B\log_2\left(1+\tilde{\eta}_k\right)}{\sum_{k=1}^{K}\boldsymbol{w}_k{}^H\boldsymbol{w}_k+P_C} \tag{V.32}$$

$$\begin{aligned} s.t.\qquad & C1, \\ & C11:\ \tilde{\eta}_k\leqslant\frac{\left|\tilde{\boldsymbol{\varsigma}}_k^H\boldsymbol{w}_k\right|^2}{\sum_{j=1,j\neq k}^{K}\left|\tilde{\boldsymbol{\varsigma}}_k^H\boldsymbol{w}_j\right|^2+\sigma^2},\ \forall k\in\{1,\cdots,K\}, && \text{(V.32a)} \\ & C12:\ \tilde{\eta}_k\geqslant 2^{\frac{r_{\min,k}}{B}}-1,\ \forall k\in\{1,\cdots,K\}, && \text{(V.32b)} \end{aligned}$$

where $\tilde{\boldsymbol{\eta}} = [\tilde{\eta}_1, \cdots, \tilde{\eta}_K]$ contains K slack variables, and $\tilde{\boldsymbol{\varsigma}}_k = \hat{\boldsymbol{h}}_k \hat{\boldsymbol{\Theta}} \boldsymbol{G}$.

To deal with the non-convexity of $C11$, we introduce the slack variable $\tilde{\zeta}_k > 0$, $k = 1, \cdots, K$, $\tilde{\boldsymbol{\zeta}} = \left[\tilde{\zeta}_1, \cdots, \tilde{\zeta_K}\right]$. Since we can express $\tilde{\boldsymbol{\varsigma}}_k^H \boldsymbol{w}_k$ as a real number by arbitrarily rotating the phase of $\boldsymbol{w}_k$ [21], we convert $C11$ to

$$C11.1: \ \sqrt{\tilde{\eta}_k \tilde{\zeta}_k} \leqslant \Re\left(\tilde{\boldsymbol{\varsigma}}_k^H \boldsymbol{w}_k\right), \tag{V.33}$$

$$C11.2: \ \sum\nolimits_{j=1, j\neq k}^{K} \left|\tilde{\boldsymbol{\varsigma}}_k^H \boldsymbol{w}_j\right|^2 + \sigma^2 \leqslant \tilde{\zeta}_k. \tag{V.34}$$

Since $C11.1$ is still non-convex, we apply SCA to it, i.e., by substituting $\sqrt{\tilde{\eta}_k \tilde{\zeta}_k}$ with its first order Taylor polynomial, and in the s-th iteration we have

$$\begin{aligned} C11.1': \ & \Re\left(\tilde{\boldsymbol{\varsigma}}_k^{(s)} {\boldsymbol{w}_k^{(s)}}^H\right) \geqslant \sqrt{\tilde{\eta}_k^{(s-1)} \tilde{\zeta}_k^{(s-1)}} \\ & + \frac{1}{2}\sqrt{\frac{\tilde{\zeta}_k^{(s-1)}}{\tilde{\eta}_k^{(s-1)}}}\left(\tilde{\eta}_k^{(s)} - \tilde{\eta}_k^{(s-1)}\right) + \frac{1}{2}\sqrt{\frac{\tilde{\eta}_k^{(s-1)}}{\tilde{\zeta}_k^{(s-1)}}}\left(\tilde{\zeta}_k^{(s)} - \tilde{\zeta}_k^{(s-1)}\right) \end{aligned} \tag{V.35}$$

Replacing $C11$ by $C11.1'$ and $C11.2$, $(P7)$ converts to

$$\begin{aligned} (P8): \ & \max_{\tilde{\boldsymbol{\eta}}^{(s)}, \boldsymbol{w}_1^{(s)}, \cdots, \boldsymbol{w}_K^{(s)}, \tilde{\boldsymbol{\zeta}}^{(s)}} \frac{\sum_{k=1}^{K} B\log_2\left(1 + \tilde{\eta}_k^{(s)}\right)}{\sum_{k=1}^{K} {\boldsymbol{w}_k^{(s)}}^H \boldsymbol{w}_k{}^{(s)} + P_C} \\ & s.t. \ C1, C11.1', C11.2, C12. \end{aligned} \tag{V.36}$$

We note that $(P8)$ is a convex problem and can be solved by the Dinkelbach method [24].

Based on the above solutions to $(P6)$ and $(P8)$, we propose an iterative algorithm to solve $(P2)$ by solving $(P6)$ and $(P8)$ alternately in each iteration as shown in Algorithm 1, where ε is a very small positive value used to terminate the iteration. It is not difficult to verify that the introduction of the slack variables does not lose the optimality of the

Algorithm 4 EEM Algorithm

Input: $\hat{\boldsymbol{h}}_k,\ \forall k \in \{1,\cdots,K\}, \boldsymbol{G}, I, \boldsymbol{q}_I, \varepsilon$
Output: $\hat{\boldsymbol{\Theta}}_{\text{opt}}, \boldsymbol{w}_{1\text{opt}}, \cdots, \boldsymbol{w}_{K\text{opt}}, EE_{\text{opt}}$
1: Set the iteration index $s = 0$ and initialize $\hat{\boldsymbol{\Theta}}^{(0)}, \boldsymbol{w}_k^{(0)}$ and $EE^{(0)}$ $\forall k \in \{1,\cdots,K\}$.
2: **repeat**
3: Update $s = s + 1$.
4: Obtain $\hat{\boldsymbol{\Theta}}^{(s)}$ by solving $(P6)$.
5: Obtain $\boldsymbol{w}_k^{(s)},\ \forall k \in \{1,\cdots,K\}$ by solving $(P8)$.
6: Obtain $EE^{(s)}$ by calculating (V.22)
7: **until** $EE^{(s)} - EE^{(s-1)} < \varepsilon$.
8: $EE_{\text{opt}} = EE^{(s)}, \hat{\boldsymbol{\Theta}}_{\text{opt}} = \hat{\boldsymbol{\Theta}}^{(s)}, \boldsymbol{w}_{k\text{opt}} = \boldsymbol{w}_k^{(s)},\ \forall k \in \{1,\cdots,K\}$

optimization problem, since all the constraints that include slack variables can be met with equality.

For subproblems $(P6)$ and $(P8)$, the optimal solutions are obtained in each iteration of Algorithm 1, and as a result, the objective function in $(P2)$ is non-decreasing over iterations. Moreover, the objective function of $(P2)$ is upper bounded due to the maximum transmit power at the BS. Thus, the proposed EEM algorithm is guaranteed to converge.

The complexity of Algorithm 1 is analyzed as follows. In each iteration of Algorithm 1, the complexity of solving $(P6)$ is $\mathcal{O}((2K+IN)^2(4K+IN))$ [25], where $2K+IN$ and $4K+IN$ are the number of variables and the total number of constraints in $(P6)$, respectively; and the complexity of solving $(P8)$ is $\mathcal{O}(DQ)$ [24], where D is the number of iterations required by the Dinkelbach method and Q is the complexity per iteration of the Dinkelbach method. The number of iterations required by the SCA to converge in solving $(P5)$ is $\mathcal{O}(\sqrt{4K+IN}\log_2(1/\varepsilon))$ [26], where $4K+IN$ is the total number of constraints in $(P5)$; while the number of iterations required by the SCA to converge in solving $(P7)$ is $\mathcal{O}(\sqrt{2K+1}\log_2(1/\varepsilon))$, where $2K+1$ is the total number of constraints in $(P7)$. So, the complexity of Algorithm 1 is $\mathcal{O}\left(\log_2(1/\varepsilon)\left[\sqrt{4K+IN}(2K+IN)^2(4K+IN)+\sqrt{2K+1}DQ\right]\right)$ [21].

V.3.3 IOSLN Algorithm

For given phase shifts of IOSs and beamforming vectors of the BS obtained by Algorithm 1, $(P1)$ reduces to

$$(P9): \max_{I,\boldsymbol{q}_{\mathrm{IOS_c}}} \frac{\sum_{k=1}^{K} r_k}{\sum_{k=1}^{K} \boldsymbol{w}_k{}^H \boldsymbol{w}_k + P_C} \quad \text{(V.37)}$$
$$s.t.\ C3, C4, C5, C6, C7.$$

To solve $(P9)$ is to obtain the optimal number and locations of IOSs that maximize the downlink transmission energy efficiency of the BS. To this end, we divide the wall area where the IOSs will be deployed (as defined by C5 and C6) into $\frac{L_\mathrm{r}}{d_I}$ columns each of the same length $H_\mathrm{r} - E[\boldsymbol{H}_o]$ and width d_I, where $\frac{L_\mathrm{r}}{d_I}$ is assumed to be an integer for simplicity. This is because d_I is much smaller than L_r and we allow the outermost column at either edge of the wall to be slightly wider than d_I. Each IOS is deployed within a column (not across any two columns). More than one IOS is allowed to be deployed in a column. Without loss of generality, if one of the top corners of the wall is assigned the value of 0 and its diagonally opposite corner of the considered wall area is assigned the value of $\frac{L_\mathrm{r}(H_\mathrm{r}-E[\boldsymbol{H}_o])}{d_I}$, then all possible IOS-deployment locations on the wall form a continuous range from 0 to $\frac{L_\mathrm{r}(H_\mathrm{r}-E[\boldsymbol{H}_o])}{d_I}$. To obtain the optimal locations of I IOSs for given I, we employ the Population Based Incremental Learning for continuous space (PBILc) [27], where a probabilistic model that characterizes a population evolves over generations instead of the individuals in the population. Hence, PBILc is more efficient than traditional evolutionary algorithms such as the genetic algorithm (GA) and particle swarm optimization (PSO).

In the following, we present the PBILc-based IOSLN algorithm to solve (P9). First, we set the number of IOS(s) $I = 1$ and the iteration index $s' = 1$, and randomly initial-

ize a population of N_{ind} individuals, where N_{ind} is an even number and each individual contains the location(s) of I IOS(s), $\boldsymbol{q}_{\mathrm{IOS_c}} = [q_{\mathrm{c}_1}, \cdots, q_{\mathrm{c}_I}]$. The initialized location of each IOS follows an independent, identical Gaussian distribution $\mathcal{N}(X^{(s')}, \sigma_X^{(s')})$, where the initialized mean value $X^{(s')} = \frac{L_{\mathrm{r}}(H_{\mathrm{r}} - E[\boldsymbol{H}_o])}{2d_I}$ (i.e., the centre of the considered wall area), and the initialized standard deviation $\sigma_X^{(s')} = \frac{L_{\mathrm{r}}(H_{\mathrm{r}} - E[\boldsymbol{H}_o])}{4d_I}$. An individual will be discarded and generated again if any two of its IOS locations are in the same column and the distance between them is smaller than d_I. Then, Algorithm 1 is used to obtain $\boldsymbol{w}_{k\mathrm{opt}}$, $\hat{\boldsymbol{\Theta}}_{\mathrm{opt}}$, $k \in \{1, \cdots, K\}$ for each individual and EE_{opt} is taken as the fitness value of the corresponding individual. The individual with the largest fitness value in the population is identified, and its $\boldsymbol{w}_{k\mathrm{opt}}$, $\hat{\boldsymbol{\Theta}}_{\mathrm{opt}}$ and EE_{opt} are denoted by $\boldsymbol{w}_{k\mathrm{opt}I}^{(s')}$, $\hat{\boldsymbol{\Theta}}_{\mathrm{opt}I}^{(s')}$ and $EE_{\mathrm{opt}I}^{(s')}$, $k \in \{1, \cdots, K\}$, respectively.

Update $s' = s' + 1$, and a new half-population of $\frac{N_{\mathrm{ind}}}{2}$ individuals are generated by selecting the $\frac{N_{\mathrm{ind}}}{2}$ individuals of the highest fitness values from the previous population. Next, the mean value of the Gaussian distribution is updated as

$$X^{(s')} = (1 - \chi)X^{(s'-1)} + \chi(X^{best_1} + X^{best_2} - X^{worst}), \tag{V.38}$$

where $\chi \in (0, 1)$ is a constant relaxation factor, X^{best_1} and X^{best_2} are the mean values of the two individuals with the largest two fitness values in the new half-population, and X^{worst} is the mean value of the individual with the smallest fitness value in the new half-population. The standard deviation of the Gaussian distribution is updated as

$$\sigma_X^{(s')} = (1 - \chi)\sigma_X^{(s'-1)} + \chi\sqrt{\frac{\sum_{j=1}^{\frac{N_{\mathrm{ind}}}{2}}(X_j - \bar{X}_j)^2}{\frac{N_{\mathrm{ind}}}{2}}}, \tag{V.39}$$

where X_j is the mean value of the j-th individual of the new half-population, and $\bar{X}_j$ is the average value of all X_j, for $j = 1, \cdots, \frac{N_{\mathrm{ind}}}{2}$. Afterwards, another new half-population

of $\frac{N_{\text{ind}}}{2}$ individuals are generated independently following the updated Gaussian distribution. An individual will be discarded and generated again if any two of its IOS locations are in the same column and their distance is less than d_I. The two half-populations form a new population. Then, for each individual in the new population, Algorithm 1 is used to obtain $\boldsymbol{w}_{k\text{opt}}$, $\hat{\boldsymbol{\Theta}}_{\text{opt}}$ and EE_{opt}, $k \in \{1, \cdots, K\}$. The individual that has the largest fitness value among the population is identified, and its $\boldsymbol{w}_{k\text{opt}}$, $\hat{\boldsymbol{\Theta}}_{\text{opt}}$ and EE_{opt} are labeled as $\boldsymbol{w}_{k\text{opt}I}^{(s')}$, $\hat{\boldsymbol{\Theta}}_{\text{opt}I}^{(s')}$ and $EE_{\text{opt}I}^{(s')}$, $k \in \{1, \cdots, K\}$, respectively.

The above procedures repeat until $EE_{\text{opt}I}^{(s')} - EE_{\text{opt}I}^{(s'-1)} < \varepsilon$. Once the iteration terminates, the individual of the largest fitness value among the latest population is identified as the optimal locations of the I IOSs, labeled as $\boldsymbol{q}_{\text{opt}I}$, and its $\boldsymbol{w}_{k\text{opt}I}^{(s')}$, $\hat{\boldsymbol{\Theta}}_{\text{opt}I}^{(s')}$, and $EE_{\text{opt}I}^{(s')}$ are labeled as $\boldsymbol{w}_{k\text{opt}I}$, $\hat{\boldsymbol{\Theta}}_{\text{opt}I}$, and $EE_{\text{opt}I}$, $k \in \{1, \cdots, K\}$, respectively. The above iterative algorithm for any given value of I is ensured to converge when the iteration number is large enough [27].

Update $I = I + 1$ and repeat the above procedures until $EE_{\text{opt}I} - EE_{\text{opt}(I-1)} < \varepsilon$. Finally, the value of I that is associated with the highest value of $EE_{\text{opt}I}$ is identified as I_{opt} and its corresponding $\boldsymbol{q}_{\text{opt}I}$, $EE_{\text{opt}I}$, $\boldsymbol{w}_{k\text{opt}I}$, $\hat{\boldsymbol{\Theta}}_{\text{opt}I}$, $k \in \{1, \cdots, K\}$ return the optimal IOS locations, energy efficiency of the BS, BS beamforming vectors and IOS phase shifts, respectively.

The above IOSLN Algorithm is summarized in Algorithm 2. It has a complexity of $\mathcal{O}\left(\sum_{I=1}^{I_{\text{opt}}}\left(\log_2(1/\varepsilon)\left[\sqrt{2K+IN}(2K+IN)^2(4K+IN)+\sqrt{2K+1}DQ\right]N_{ind}\frac{N_{\text{P}I}+1}{2}\right)\right)$, where $N_{\text{P}I}$ is the number of iterations required for the PBILc to converge for $I \in \{1, \cdots, I_{\text{opt}}\}$.

Algorithm 5 IOSLN Algorithm

Input: N_{ind}, ε, K, $\boldsymbol{\Xi}$.

Output: I_{opt}, $\boldsymbol{q}_{\text{opt}I}$, $EE_{\text{opt}I}$, $\boldsymbol{w}_{k\text{opt}I}$, $\hat{\boldsymbol{\Theta}}_{\text{opt}I}$, $k \in \{1, \cdots, K\}$.

Initialize $I = 0$ and $EE_{\text{opt}0} = 0$.
repeat
  Update $I = I + 1$
  Set the iteration index $s' = 1$, and randomly initialize a population of N_{ind} individuals, where each individual contains I independent IOS locations, $q_i \sim \mathcal{N}(X^{(s')}, \sigma_X^{(s')})$, $i \in \{1, \cdots, I\}$, where $X^{(s')} = \frac{L_{\text{r}}(H_{\text{r}} - E[\boldsymbol{H}_o])}{2d_I}$ and $\sigma_X^{(s')} = \frac{L_{\text{r}}(H_{\text{r}} - E[\boldsymbol{H}_o])}{4d_I}$. Run Algorithm 1 for each individual and take EE_{opt} as its fitness value.
  repeat
    Update $s' = s' + 1$.
    A new half-population is formed by the $\frac{N_{\text{ind}}}{2}$ individuals with the largest fitness values of the previous population.
    Update $X^{(s')}$ and $\sigma_X^{(s')}$ based on (V.38) and (V.39), respectively.
    Generate $\frac{N_{\text{ind}}}{2}$ individuals independently following $\mathcal{N}(X^{(s')}, \sigma_X^{(s')})$. The two half-populations to form a new population.
    Run Algorithm 1 for each individual in the new population. The individual that has the largest fitness value returns $\boldsymbol{w}_{k\text{opt}I}^{(s')}$, $\hat{\boldsymbol{\Theta}}_{\text{opt}I}^{(s')}$ and $EE_{\text{opt}I}^{(s')}$, $k \in \{1, \cdots, K\}$.
  until $EE_{\text{opt}I}^{(s')} - EE_{\text{opt}I}^{(s'-1)} < \varepsilon$.
  $\boldsymbol{w}_{k\text{opt}I} = \boldsymbol{w}_{k\text{opt}I}^{(s')}$, $\hat{\boldsymbol{\Theta}}_{\text{opt}I} = \hat{\boldsymbol{\Theta}}_{\text{opt}I}^{(s')}$, $EE_{\text{opt}I} = EE_{\text{opt}I}^{(s')}$, $k \in \{1, \cdots, K\}$.
until $EE_{\text{opt}I} - EE_{\text{opt}(I-1)} < \varepsilon$.
$I_{\text{opt}} = \underset{I}{arg\max}\{EE_{\text{opt}I}\}$ and return its $\boldsymbol{q}_{I\text{opt}}$, $EE_{\text{opt}I}$, $\boldsymbol{w}_{k\text{opt}I}$, $\hat{\boldsymbol{\Theta}}_{\text{opt}I}$, $k \in \{1, \cdots, K\}$ as output.

Table V.1: Parameter Values Used in the Simulation

Parameter		Value
M	number of antennas at the BS	16
N_{TR}	number of active transceivers at the BS	4
P_{TR}	circuit power of each active transceiver	30dBm
P_{BS}	circuit power of the BS	35dBm
$P_{\mathrm{T}_{\max}}$	maximum transmit power at the BS	35dBm
IN	total number of elements on IOSs	120
q_{B}	location of the BS	$(-50, 5, 5)$m
K	number of users	40
P_k	circuit power of each user	10dBm
σ^2	noise power	-85dBm
B	bandwidth	1GHz
$r_{\min}$	minimum data rate required	5Mbps
κ	blockage density	0.15blockages/m^2
L_r	room length	10m
W_r	room width	10m
H_r	room height	10m
$\mathbf{\Xi}$	users' spacial distribution	uniform distribution

V.4 Simulation Results

In this section, we present simulation results to evaluate the performance of the proposed algorithms. The simulated system model aligns with the description in Section II, and the parameter values used in the simulation are listed in Table I unless otherwise specified. In the simulations, we compare the performance of Algorithm 2 with three benchmark schemes: (i) an evenly distributed IOS deployment scheme [18], where the IOSs are evenly spaced on the wall at the same height, and the number and height of IOSs are optimized using Algorithm 2; (ii) centralized deployment (i.e., a single IOS) with an optimal location on the wall obtained by Algorithm 2 using $I = 1$; and (iii) the case without deploying any RIS. In all compared schemes, the IOSs are deployed on the same wall, as shown in Fig. 1, and the total number (IN) of elements on IOS(s) is kept constant.

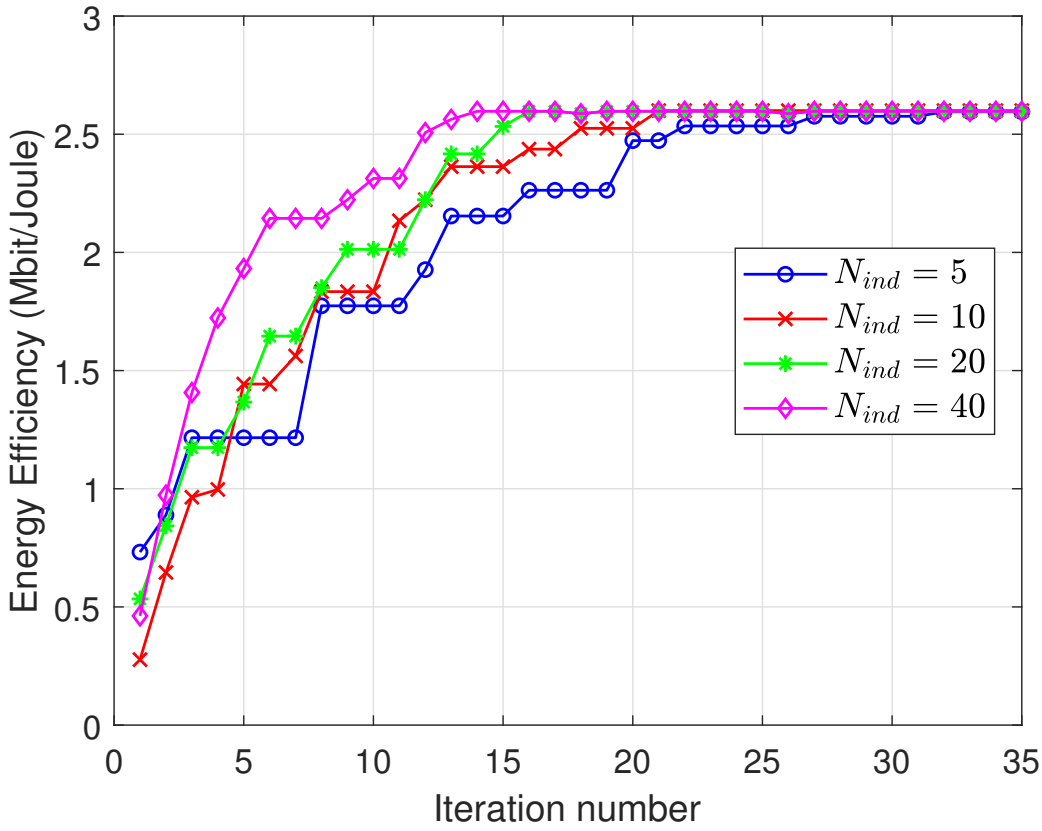

Figure V.2: Energy efficiency versus the iteration number.

In Fig.V.2, we plot the energy efficiency of the outdoor BS versus the number of iterations in Algorithm 2 for different population sizes (N_{ind}) used in the PBILc. The energy efficiency of the outdoor BS first increases with the iteration number and finally converges to a stable value. Algorithm 2 converges faster for a larger value of N_{ind}, because it is likely to obtain a larger fitness value in each iteration with a larger population size.

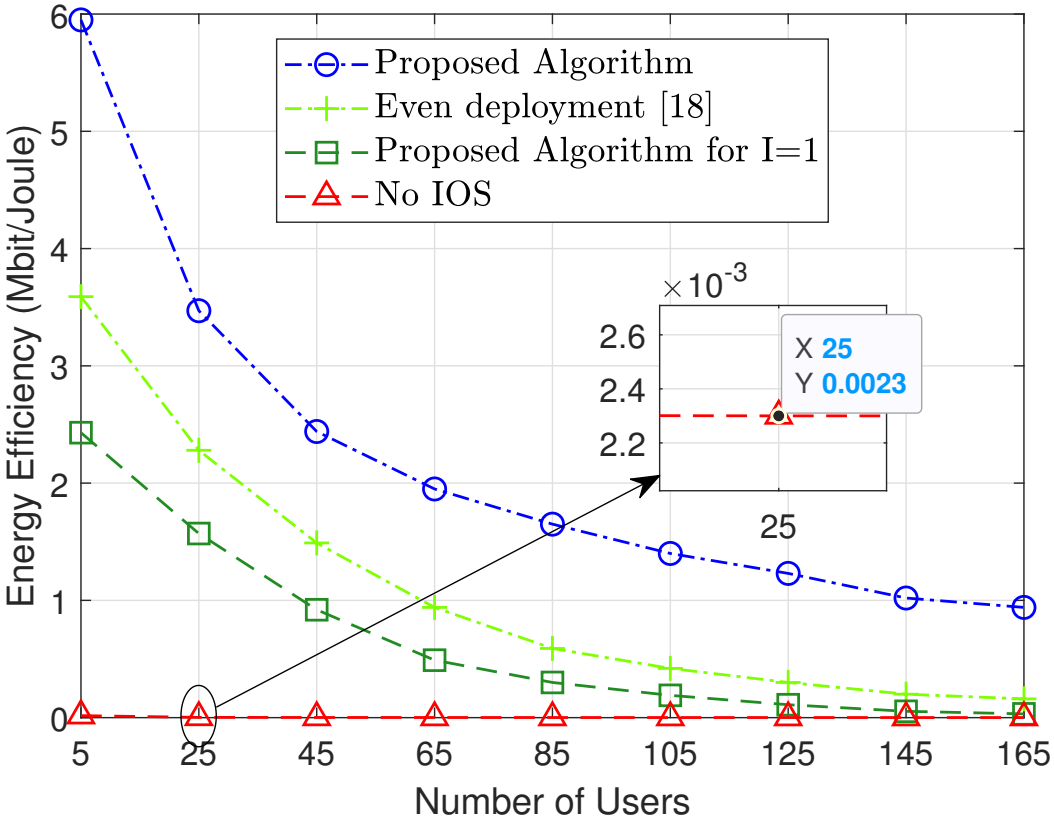

Figure V.3: Energy efficiency versus the number of users.

In Fig. V.3, we present a plot of the downlink transmission energy efficiency of the outdoor BS against the number of users in the indoor environment under consideration. The energy efficiency for all four schemes is observed to decrease as the number of users increases, given that a larger number of users necessitates higher transmit power at the

BS. For a specific number of users, the proposed algorithm consistently achieves significantly higher energy efficiency compared to the benchmark schemes. It is noteworthy that the energy efficiency of the BS without deploying any IOS is notably low due to severe penetration losses and attenuations of signal strength at mmWave frequencies.

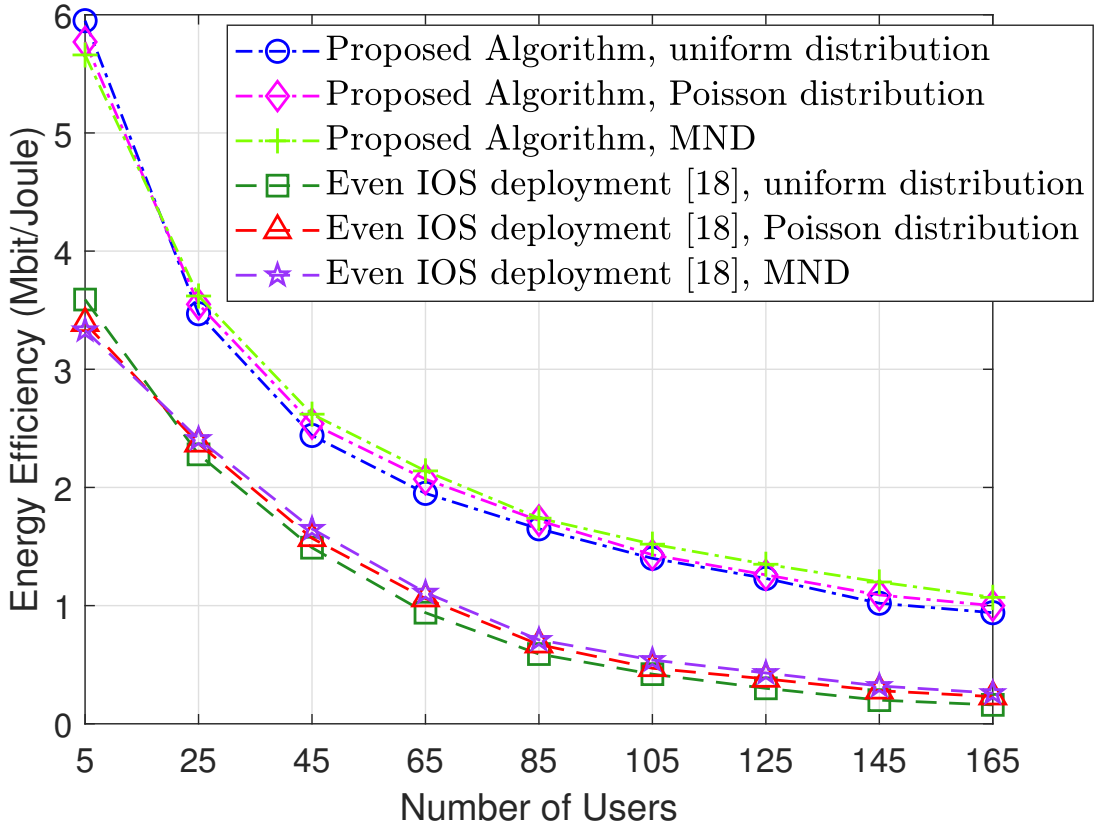

Figure V.4: Energy efficiency versus the number of users for different user distributions.

In Fig. V.4, we plot the energy efficiency of the outdoor BS versus the number of users for three different indoor user spatial distributions: (i) the uniform distribution that is considered in the system model; (ii) a Poisson distribution where x_k and y_k of user k ($k = 1, 2, \cdots, K$) each follow an independent Poisson distribution with the expected occurrence rate of $\lambda = 3$, i.e., the users are gathered toward the point $(3, 3)$ in the 10m $\times$ 10m room; and (iii) a multivariate normal distribution (MND) where

$x_k \sim \mathcal{N}(5,5)$ and $y_k \sim \mathcal{N}(5,5)$ for user k $(k = 1, 2, \cdots, K)$ independently, i.e., the users are gathered around the center point $(5, 5)$ of the room, where the unit of x_k and y_k is meter. For all the three considered user distributions, z_k of user k $(k = 1, 2, \cdots, K)$ follows an independent uniform distribution from 1m to 2m. The figure demonstrates that the proposed algorithm is applicable to different user distributions and is able to achieve a higher BS transmission energy efficiency than the even IOS deployment [18] in all the considered spatial distributions of indoor users.

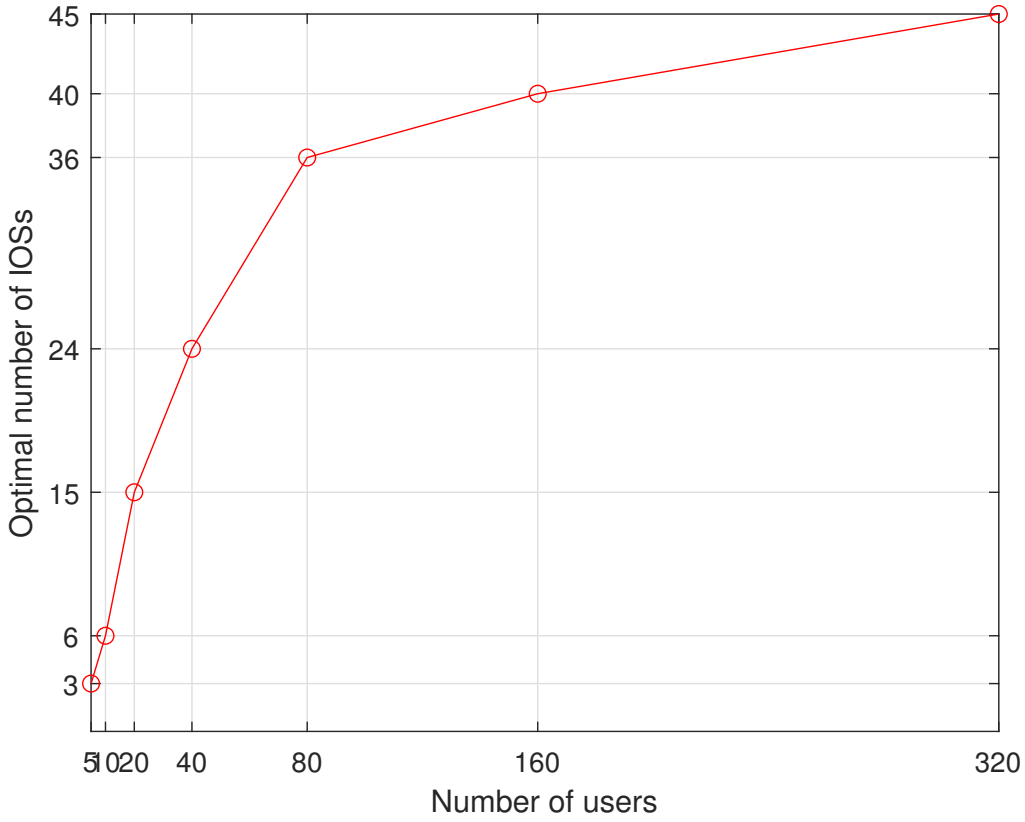

Figure V.5: Optimal number of IOSs versus the number of users.

In Fig. V.5, the optimal number of IOSs obtained by Algorithm 2 is plotted against the number of users. The total number of elements of the IOSs is fixed at 360. As the number of users increases, the optimal number of IOSs also increases, albeit at a

diminishing rate as the user population grows larger. This trend is attributed to the need for more distributed IOSs to establish LoS links with a larger number of users. However, increasing the number of IOSs while maintaining a fixed total number of elements results in a reduction in the refraction beamforming gain per IOS.

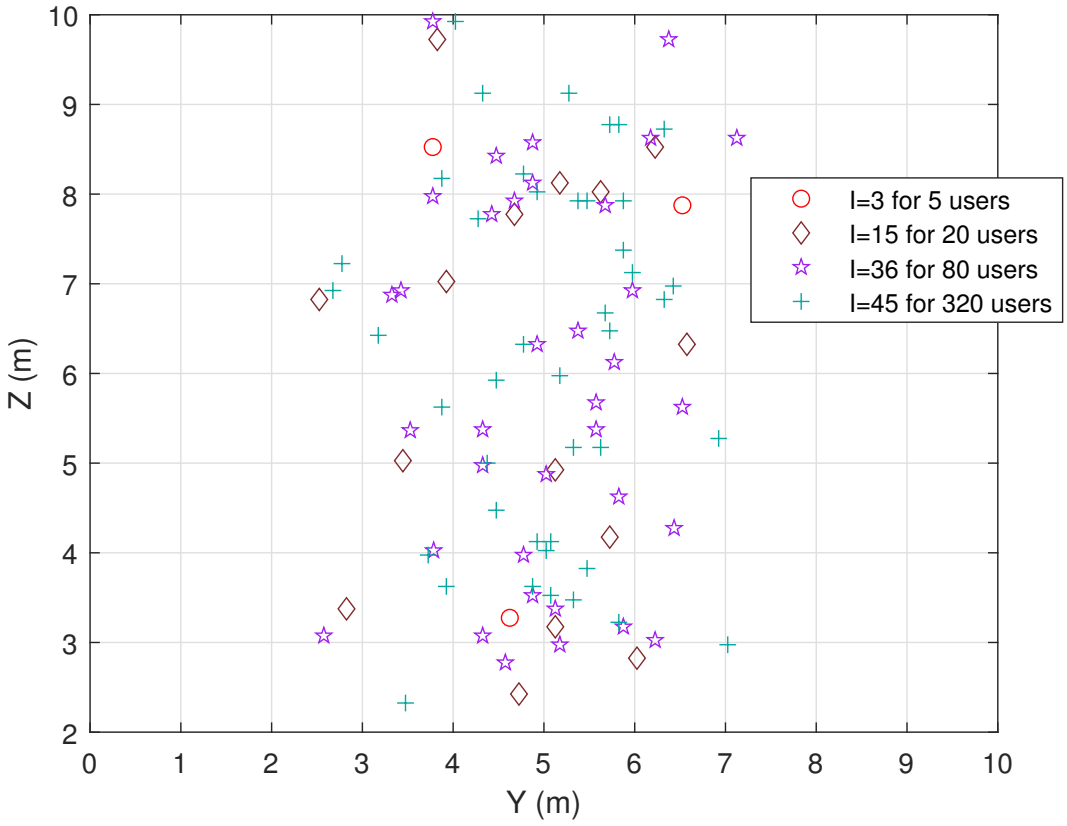

Figure V.6: Optimal number and locations of IOSs and locations.

In Fig. V.6, we illustrate the optimal locations of the ideal number of IOSs on the wall for different numbers of users, with a total of 360 elements in the IOSs. Observing the figure, it is evident that, for each considered number of users, the optimized IOS locations converge in the vertical central area of the specified wall. This concentration is attributed to the likelihood that IOSs deployed in the vertical central area are more likely to establish LoS links for a greater number of users compared to those deployed

on the left or right side of the wall. Furthermore, the outdoor BS's antenna array is positioned at $(-50, 5, 5)$, facing the center of the wall. Deploying an IOS closer to the center results in a shorter distance from the BS antenna array to the IOS, thereby reducing the path loss of the link. It is noteworthy that some IOSs are deployed above the height of the BS antenna array due to the presence of blockages and the locations of users. In other words, certain IOSs need to be positioned higher than the blockages to establish LoS links for users obstructed by tall obstacles.

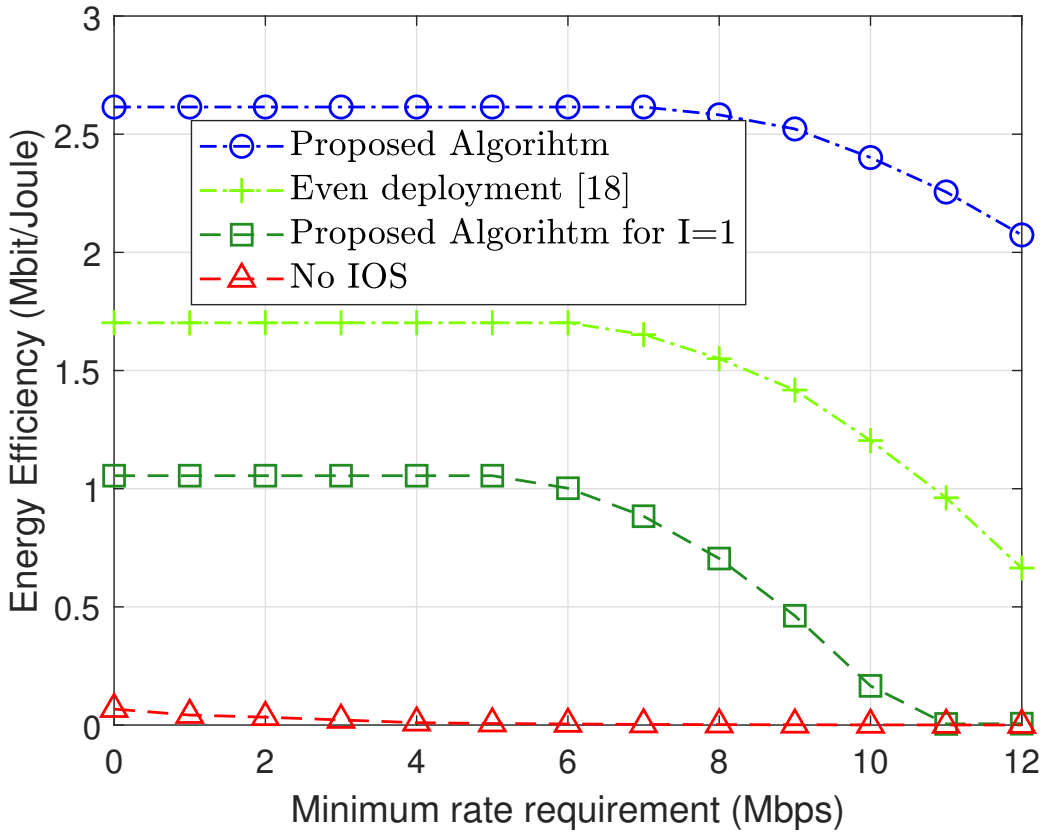

Figure V.7: Energy efficiency versus minimum rate requirement per user.

In Fig. V.7, we depict the transmission energy efficiency of the outdoor BS against the minimum rate requirement of each user. Across all schemes compared, the energy efficiency of the BS decreases as the user rate requirement increases. This trend is

attributed to the heightened transmit power needed at the BS to meet the higher minimum rate requirement, resulting in a reduction in energy efficiency. Notably, the proposed algorithm consistently outperforms the other schemes for each considered value of the user rate requirement due to the optimized number and locations of IOSs.

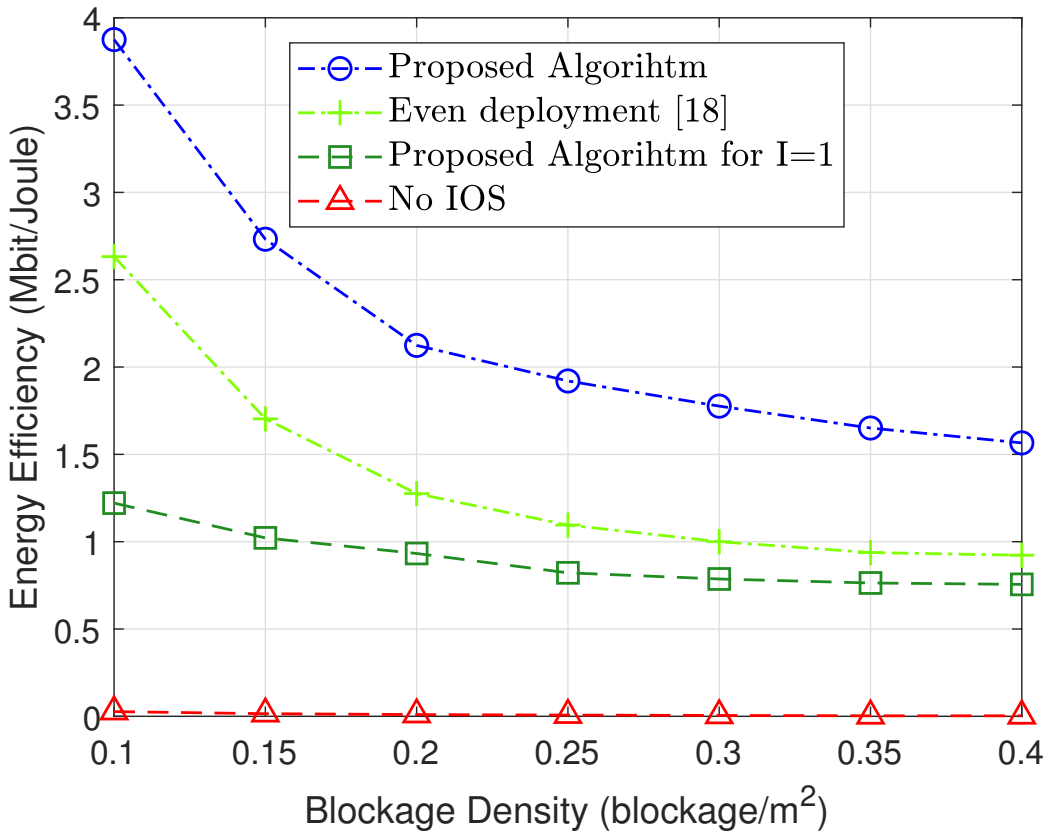

Figure V.8: Energy efficiency versus the blockage density.

In Fig. V.8, we illustrate the transmission energy efficiency of the outdoor BS against the blockage density. Across all considered schemes, the energy efficiency of the BS experiences a decline with increasing blockage density. This decline is attributed to the reduction in LoS links between the IOSs and the users as the blockage density rises. The proposed algorithm outperforms the other schemes significantly due to the optimized number and locations of IOSs, ensuring a larger number of LoS

links between the IOSs and the users. The performance gap between the centralized IOS deployment scheme and the proposed algorithm/even deployment scheme becomes smaller for higher blockage densities. This is because, under scenarios of the proposed algorithm/even deployment scheme, the number of LoS links significantly decreases with the increase in blockage density. In contrast, for the centralized IOS deployment scheme, the decrease is slight since many LoS links have already been blocked even for a small blockage density.

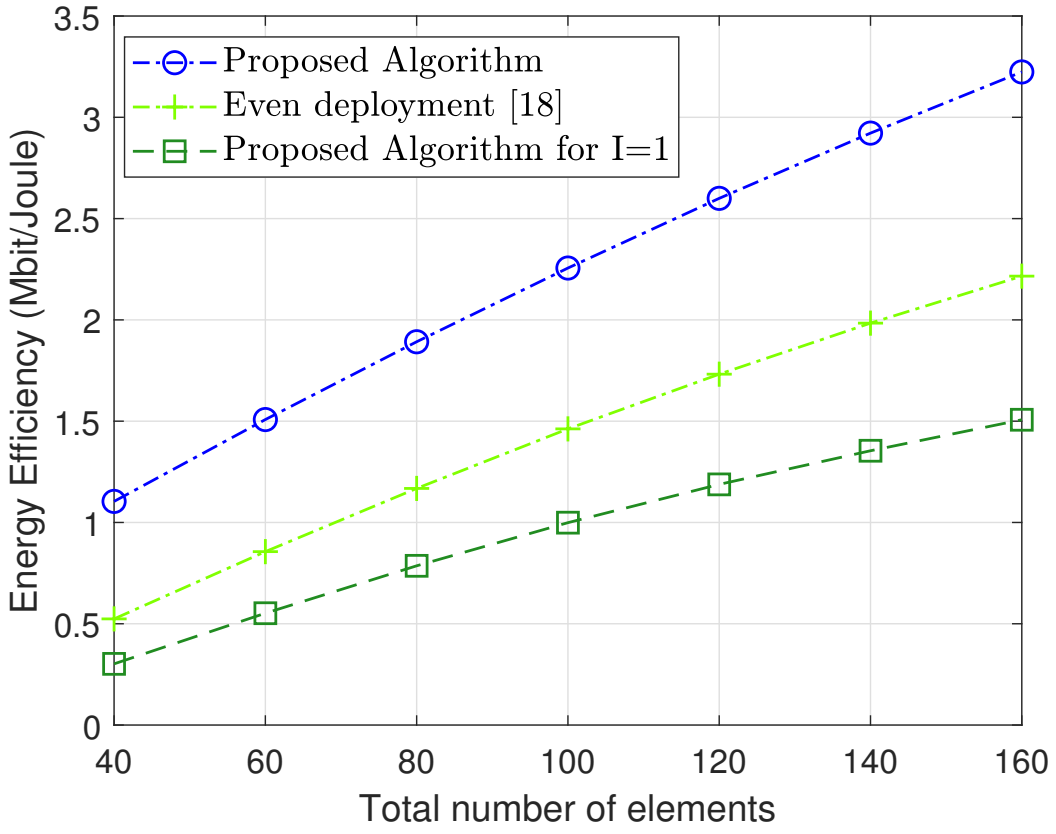

Figure V.9: Energy efficiency versus IOSs' total number of elements.

In Fig. V.9, we present the transmission energy efficiency of the outdoor BS against the total number of elements on the IOSs for the three IOS deployment schemes. Notably, for each scheme, the BS's energy efficiency increases with the total number of

elements on the IOSs, as the channel gain of the IOSs grows with the total number of elements. For a given total number of elements, the proposed algorithm consistently achieves the highest energy efficiency for the BS, followed by the evenly distributed IOS deployment [18]. The centralized IOS deployment (i.e., the proposed algorithm with $I = 1$) achieves the lowest energy efficiency for the BS. This order is attributed to the proposed algorithm having the most LoS links between the IOSs and the users, enhancing the utilization of the increased elements in the IOSs, while the centralized IOS deployment scheme has the fewest LoS links.

V.5 Conclusion and Future Work

In this study, we explored the dynamics of multiple IOSs in outdoor-to-indoor mmWave communications for multiple indoor users in the presence of indoor blockages. To maximize the transmission energy efficiency of the outdoor BS while ensuring each user's downlink data rate surpasses a specified threshold, we introduced the EEM algorithm and the IOSLN algorithm. These algorithms jointly optimize the number, locations, and phase shifts of IOSs, along with the beamforming vectors of the BS. Simulation results demonstrate that the proposed algorithms significantly enhance the downlink energy efficiency of the BS compared to benchmark schemes that either neglect IOS deployment or do not optimize the number or locations of IOSs. The optimized number and locations of IOSs play a crucial role in maximizing LoS links to users. The optimal number of IOSs increases with the number of users, but the rate of increase diminishes as the user population expands. This is attributed to the trade-off, as distributing a fixed total number of refracting elements to an increasing number of IOSs results in a reduced refraction beamforming gain per IOS. Optimal IOS locations concentrate in the vertical central area of the wall. This strategic placement allows central IOSs

to create LoS links for more users compared to those on the left or right sides. Additionally, central IOSs are closer to the outdoor BS, which faces the center of the wall. Furthermore, the transmission energy efficiency of the BS exhibits a positive correlation with the total number of IOS elements but experiences decreases with the number of users, user rate requirements, and blockage density. These findings provide valuable insights into optimizing multiple IOSs for efficient outdoor-to-indoor mmWave communications.

In our future studies, we plan to extend this work to more complex scenarios, where an outdoor BS provides services to both outdoor and indoor mobile users. Such scenarios will necessitate the use of IOSs' capabilities of both reflecting and refracting incident signals, while considering the dynamic channel conditions and potentially different mobility patterns of outdoor and indoor users. This approach promises to unveil interesting possibilities for enhancing communication efficiency and user experience.

Bibliography

[1] ABI Research, "ABI research anticipates in-building mobile data traffic to grow by more than 600% by 2020," Jan. 2016.

[2] A. Schumacher, R. Merz and A. Burg, "A mmWave bridge concept to solve the cellular outdoor-to-indoor challenge," 2020 IEEE 91st Vehicular Technology Conference (VTC2020-Spring), Antwerp, Belgium, 2020, pp. 1-6.

[3] G. Larson, "Deployment options for providing indoor coverage in high frequency bands," Master Thesis, KTH Royal Institute of Technology, Stockholm, 2015.

[4] D. W. K. Ng, M. Breiling, C. Rohde, F. Burkhardt and R. Schober, "Energy-efficient 5G outdoor-to-indoor communication: SUDAS over licensed and unlicensed spectrum," in IEEE Transactions on Wireless Communications, vol. 15, no. 5, pp. 3170-3186, May 2016.

[5] C. Umit Bas et al., "Outdoor to indoor propagation channel measurements at 28 GHz," in IEEE Transactions on Wireless Communications, vol. 18, no. 3, pp. 1477-1489, March 2019.

[6] M. Xiao et al., "Millimeter wave communications for future mobile networks," in IEEE Journal on Selected Areas in Communications, vol. 35, no. 9, pp. 1909-1935, Sept. 2017.

[7] J. Lee, K. Kim, M. Kim and J. Park, "32-GHz outdoor-to-indoor channel measurement of propagation losses and delay spread," 2019 IEEE International Symposium on Antennas and Propagation and USNC-URSI Radio Science Meeting, Atlanta, GA, USA, 2019, pp. 2071-2072.

[8] A. B. Zekri, R. Ajgou, A. Chemsa and S. Ghendir, "Analysis of outdoor to indoor penetration loss for mmWave channels," 2020 1st International Conference on Communications, Control Systems and Signal Processing (CCSSP), El Oued, Algeria, 2020, pp. 74-79.

[9] M. I. Rochman, V. Sathya and M. Ghosh, "Outdoor-to-indoor performance analysis of a commercial deployment of 5G mmWave," 2022 IEEE Future Networks World Forum (FNWF), Montreal, QC, Canada, 2022, pp. 519-525.

[10] K. Ntontin and C. Verikoukis, "Relay-aided outdoor-to-indoor communication in millimeter-wave cellular networks," in IEEE Systems Journal, vol. 14, no. 2, pp. 2473-2484, June 2020.

[11] R. Liang, J. Fan, H. Liu, Y. Ge and J. Zhang, "Dual-hop hybrid IRS-aided outdoor-to-indoor mmWave communications," in IEEE Communications Letters, vol. 26, no. 12, pp. 2979-2983, Dec. 2022.

[12] H. Zhang et al., "Intelligent omni-surfaces for full-dimensional wireless communications: Principles, technology, and implementation," in IEEE Communications Magazine, vol. 60, no. 2, pp. 39-45, February 2022.

[13] Y. Zhang, B. Di, H. Zhang, Z. Han, H. V. Poor and L. Song, "Meta-wall: Intelligent omni-surfaces aided multi-cell MIMO communications," in IEEE Transactions on Wireless Communications, vol. 21, no. 9, pp. 7026-7039, Sept. 2022.

[14] S. Zeng, H. Zhang, B. Di and L. Song, "Reconfigurable refractive surface-enabled multi-user holographic MIMO communications," in IEEE Transactions on Wireless Communications, Oct. 2023.

[15] V. Singh, M. Khalily, S. B. Amlashi, J. D. Carey and R. Tafazolli, "Fully-transparent transmission surface for outdoor-indoor mmWave coverage enhancement," 2020 International Conference on UK-China Emerging Technologies (UCET), Glasgow, UK, 2020, pp. 1-4.

[16] M. Nemati, B. Maham, S. R. Pokhrel and J. Choi, "Modeling RIS empowered outdoor-to-indoor communication in mmWave cellular networks," in IEEE Transactions on Communications, vol. 69, no. 11, pp. 7837-7850, Nov. 2021.

[17] X. Xie, C. He, X. Ma, F. Gao, Z. Han and Z. J. Wang, "Joint precoding for active intelligent transmitting surface empowered outdoor-to-indoor communication in mmWave cellular networks," in IEEE Transactions on Wireless Communications, vol. 22, no. 10, pp. 7072-7086, Oct. 2023.

[18] Z. Li, H. Hu, J. Zhang and J. Zhang, "Coverage analysis of multiple transmissive RIS-aided outdoor-to-indoor mmWave networks," in IEEE Transactions on Broadcasting, vol. 68, no. 4, pp. 935-942, Dec. 2022.

[19] S. Zhang et al., "Intelligent omni-surfaces: Ubiquitous wireless transmission by reflective-refractive metasurfaces," in IEEE Transactions on Wireless Communications, vol. 21, no. 1, pp. 219-233, Jan. 2022.

[20] T. Bai, R. Vaze, and R. W. Heath, "Analysis of blockage effects on urban cellular networks," IEEE Trans. Wireless Commun., vol. 13, no. 9, pp. 5070–5083, Sep. 2014.

[21] Z. Yang, J. Shi, Z. Li, M. Chen, W. Xu and M. Shikh-Bahaei, "Energy efficient rate splitting multiple access (RSMA) with reconfigurable intelligent surface," 2020 IEEE International Conference on Communications Workshops (ICC Workshops), 2020, pp. 1-6.

[22] L. You, J. Xiong, D. W. K. Ng, C. Yuen, W. Wang and X. Gao, "Energy efficiency and spectral efficiency tradeoff in RIS-aided multiuser MIMO uplink transmission," in IEEE Transactions on Signal Processing, vol. 69, pp. 1407-1421, 2021.

[23] S. Boyd and L. Vandenberghe, Convex optimization. Cambridge University Press, 2004.

[24] W. Dinkelbach, "On nonlinear fractional programming," Management Science, vol. 13, no. 7, pp. 492–498, 1967.

[25] M. S. Lobo, L. Vandenberghe, S. Boyd, and H. Lebret, "Applications of second-order cone programming," Linear algebra and its applications, vol. 284, no. 1-3, pp. 193–228, 1998.

[26] M. Grant, S. Boyd, and Y. Ye, "CVX: Matlab software for disciplined convex programming," 2008.

[27] M. Sebag and A. Ducoulombier, "Extending population-based incremental learning to continuous search spaces", International Conference on Parallel Problem Solving from Nature, pp. 418-427, 1998.

Chapter VI

Conclusions and Future Work

VI.1 Conclusions

In this thesis, I have studied the transmission energy minimization, energy efficiency maximization for RIS-assisted indoor, and outdoor-to-indoor environment wireless communications. I also proposed different RIS/IOS deployment strategies to improve the performance of the RIS/IOS.

Specifically, I investigated the scenario of multi-RIS-assisted mmWave communications for a robot navigating obstacles along a predefined trajectory within an industrial building. The objective was to minimize the transmission energy consumption at the AP while maintaining the SNR at the robot above a specified threshold throughout its trajectory. To achieve this, I proposed the TECO and RISLN algorithms, which jointly optimize the number, locations, and phase shifts of the RISs along with the beamforming vector of the AP. Simulation results indicated that the proposed algorithms exhibit rapid convergence and significantly reduce the transmission energy consumption of the AP. Simulation results also demonstrated that allocating a fixed total number of reflecting elements across multiple RISs reduces the AP's transmission energy, as a

greater distribution of RISs provides more LoS links to the robot as it navigates its trajectory. However, this reduction in energy consumption plateaus when the number of RISs becomes excessive. At this point, further dividing the fixed number of reflecting elements among additional RISs diminishes the beamforming gain of each RIS, as all segments of the robot's trajectory are already covered by LoS links from either the AP or an RIS.

I studied multiple IOSs in outdoor-to-indoor mmWave communications for multiple indoor users in the presence of indoor blockages. I aimed to maximize the energy efficiency of the BS and proposed EEM and IOSLN algorithms to jointly optimize the number, locations and phase shifts of the IOS, and the beamforming vectors of the BS. Simulation results showed that the proposed algorithm converge fast and effectively solve the optimization problem. Simulation results also proved that the optimal number of IOSs tends to increase with the user population though the rate of increase diminishes as the number of users grows. This trend arises from the inherent trade-off in distributing a fixed total number of refracting elements among a growing number of IOSs, which leads to a reduction in the refraction beamforming gain per IOS. Optimal placement of IOSs is typically concentrated in the vertical central area of the wall, a location that enables central IOSs to establish LoS links for a greater number of users than those positioned on the left or right sides. Additionally, central IOSs benefit from proximity to the outdoor BS, which faces the center of the wall. Moreover, the transmission energy efficiency of the BS shows a positive correlation with the total number of IOS elements but declines with increasing numbers of users, higher user rate requirements, and greater blockage density.

VI.2 Future Work

The following future research directions are proposed for each paper included in this thesis. For Paper I, I plan to investigate the problem of minimizing AP transmission energy consumption by jointly optimizing the robot's trajectory alongside the deployment of the AP and RISs. Our work will also be extended to more complex scenarios, such as multiple robots traversing distinct trajectories. This extension will involve allocating available RISs and AP beamforming vectors to different robots, while accounting for potential co-channel interference among links serving adjacent robots.

For Paper II, I intend to extend this work to more intricate scenarios in which an outdoor BS provides services to both outdoor and indoor mobile users. These scenarios will require leveraging the dual capabilities of IOSs to both reflect and refract incident signals, while taking into account dynamic channel conditions and the potentially differing mobility patterns of outdoor and indoor users. This approach is expected to reveal significant opportunities for improving communication efficiency and enhancing the user experience.

I intend to develop a RIS-based LLM that simultaneously optimizes variables such as the beamforming vectors of the BS, the phase shifts of the RIS, the number and placement of RISs, and the trajectory of moving objects. This approach avoids partitioning the problem into subproblems, thereby reducing both the complexity and computational time of the algorithm.

The RIS deployment can be further extended to encompass a 3D space, allowing for more intricate and sophisticated deployment strategies. This extension includes the modeling of complex electromagnetic wave propagation phenomena, such as multi-path fading and Doppler shifts, which are critical in mobile and high-speed scenarios. Furthermore, it involves the integration of adaptive algorithms for real-time optimization,

the handling of diverse user densities and traffic patterns, and the incorporation of heterogeneous network elements, such as multiple base stations or access points. Additionally, it enables the exploration of advanced configurations, such as RIS deployment in urban landscapes with dense infrastructure, integration with aerial platforms like unmanned aerial vehicles, and the coordination of multiple RISs in different directions to manage complex electromagnetic environments.